Diode laser spectroscopy in extended wavelength ranges

Gustafsson, Ulf

2000

DIODE LASER SPECTROSCOPY

IN EXTENDED WAVELENGTH RANGES

Ulf Gustafsson

Lund Reports on Atomic Physics
LRAP-253

Doctoral Thesis
Department of Physics
Lund Institute of Technology
April 2000

ISBN 91-7874-047-9

Contents

Abstract

Diode laser spectroscopy performed in the ultraviolet, visible and infrared spectral regions is presented.

The accessible wavelength range for visible and near-infrared diode lasers is extended by the use of sum- and difference-frequency generation. Sum-frequency generation to the ultraviolet spectral region was employed using a blue and a red diode laser. Mercury spectroscopy was demonstrated with the generated ultraviolet beam. Difference-frequency generation with two near-infrared diode lasers has been utilised to extend the wavelength range to the mid-infrared spectral region. With each of the three wavelengths resonant with a molecular species, detection of molecular oxygen, water vapour, and methane was achieved simultaneously.

By employing frequency modulation techniques, detection limits are improved by orders of magnitude compared to direct absorption measurements. Frequency modulated absorption spectroscopy in the red spectral region was performed for sensitive long-path absorption monitoring of nitrogen dioxide. The possibility of employing frequency modulation techniques for sensitive absorption measurements in the blue and ultraviolet spectral region has also been investigated. Atomic spectroscopy in the blue and red spectral region has been demonstrated, providing a pedagogical demonstration of the theory for Doppler broadening.

A new instrument, using a coupled cavity diode laser, has been constructed and employed for aerosol particle sizing and identification. The size of a single aerosol particle is determined by an extinction loss signal and identification is performed using a diffraction image.

A compact fluorosensor utilising a violet diode laser as an exciting source combined with an integrated spectrometer and fibre-optic sampling for the monitoring of fluorescence signatures was developed. The potential of this new instrument was demonstrated in measurements on vegetation and human malignant skin lesions.

List of papers

This thesis is based on the following papers:

Paper I. J. Sandsten, U. Gustafsson and G. Somesfalean, *Single aerosol particle sizing and identification using a coupled-cavity diode laser*, Optics Communications **168**, 17-24 (1999).

Paper II. U. Gustafsson, J. Alnis and S. Svanberg, *Atomic spectroscopy with violet laser diodes*, American Journal of Physics, tentatively Vol. 68, April 2000.

Paper III. U. Gustafsson, G. Somesfalean, J. Alnis and S. Svanberg, *Frequency modulation spectroscopy with blue diode lasers*, Submitted to Applied Optics, October 1999.

Paper IV. G. Somesfalean, J. Alnis, U. Gustafsson, H. Edner, and S. Svanberg, *Long-path monitoring of NO_2 with a 635 nm diode laser using frequency modulation spectroscopy*, Manuscript.

Paper V. J. Alnis, U. Gustafsson, G. Somesfalean and S. Svanberg, *Sum-frequency generation with a blue diode laser for mercury spectroscopy at 254 nm*, Applied Physics Letters **76**, 1234-1236 (2000).

Paper VI. U. Gustafsson, J. Sandsten, and S. Svanberg, *Simultaneous detection of methane, oxygen and water vapour utilizing near-infrared diode lasers in conjunction with difference frequency generation*, Submitted to Applied Physics B, March 2000.

Paper VII. U. Gustafsson, S. Pålsson, and S. Svanberg, *Compact fiber-optic fluorosensor using a continuous-wave violet diode laser*, Submitted to Review of Scientific Instruments, December 1999.

Appendix

Paper VIII. X. Wang, M. Afzelius, N. Ohlsson, U. Gustafsson, and S. Kröll, *Coherent transient optical data rate conversion and data transformation*, Submitted to Optics Letters, December 1999.

1. Introduction

Ever since their introduction, lasers have found their way into a large variety of spectroscopic applications, ranging from scientific utilisation in molecular spectroscopy, plasma physics, and generation of high-order harmonics, to monitoring of atmospheric pollutants, and the detection and demarcation of cancer. The continued growth of laser applications into different research areas is due to the high spatial, spectral and temporal resolution achievable by lasers.

Due to their low prize, compact size, low power consumption, and convenient operation, diode lasers can provide cheap and realistic implementations of techniques developed using much more advanced and expensive laser sources. Except from being used in compact disc players, optical memories, laser printers, bar-code readers, telecommunications, alignment and pointing applications, metrology and distance measurements, etc., the diode laser is also being used for atmospheric trace gas detection and monitoring, industrial process control, medical diagnostics, and for the study of combustion processes. The work presented in this thesis aims at studying the use of diode laser spectroscopy in environmental, medical and combustion applications. Most of the work is on absorption spectroscopy for monitoring of atmospheric pollutants, but feasibility studies using diode lasers for inducing fluorescence in vegetation monitoring and medical diagnostics, and in scattering to determine size and shape of aerosol particles have also been performed. Special emphasis is placed on the applied nature of diode laser spectroscopy, more than on fundamental aspects of the laser-matter interaction.

This thesis is divided into two parts, the first one presenting different aspects of diode laser spectroscopy, the diode laser itself, absorption spectroscopy, methods for achieving a high sensitivity in absorption measurements and extending the available diode laser wavelength region, and the second part containing the scientific papers on which this thesis is based.

Since the work presented exclusively makes use of diode lasers emitting coherent radiation in the visible and near-infrared region (around 400 nm, 635 nm, 690 nm, 760 nm, 780 nm and 980 nm) corresponding diode laser types and different diode laser characteristics, such as construction, beam properties, emission spectrum, and tunability are presented in some detail in Chapter 2.

Absorption spectroscopy using diode lasers is a powerful method for quantitative measurements of gaseous species. In direct absorption measurements the diode laser wavelength is scanned across the whole absorbing feature, and the recorded absorption spectrum is subsequently evaluated to achieve information on concentration, pressure and temperature. In order to reach a high accuracy and sensitivity in the measurements, a precise theoretical model which accurately describes the absorption line under varying environmental conditions is required. In Chapter 3 important absorption relations are presented and aspects of achieving a high sensitivity in direct diode laser absorption measurements are discussed.

Tuneable diode laser absorption spectroscopy is often used in conjunction with modulation techniques. Compared to direct absorption measurements, which often have to resolve small intensity changes on a large background signal, modulation techniques can provide orders of magnitude higher sensitivity. The basic concept of all modulation techniques is the movement of the detection band to a high frequency region, where the laser excess noise is avoided or significantly reduced. Different modulation techniques and a brief overview of noise sources and the achievable sensitivity using modulation are presented in Chapter 4.

Commercially available room-temperature operated diode lasers essentially cover the range from 400 nm to 2 µm. Since it is interesting to employ these diode lasers also at wavelengths below 400 nm and above 2 µm, the use of nonlinear optical frequency conversion is a way of extending the available wavelength range. In Chapter 5, aspects of the nonlinear optical conversion frequency process, including birefringent and quasi phase-matching as well as conversion efficiency are summarised.

In the final Chapter 6, applications relevant to energy, environmental and medical research are presented and discussed.

2. Diode lasers

The diode laser is in many aspects a unique light source. The compact size, low power consumption, long life time, high reliability, easy operation, and relatively low cost make the diode lasers extremely well suited for several important opto-electronic devices. During the 1980's, driven by the demand in the communication and consumer electronic markets, the diode laser was transformed from a laboratory device operated only at cryogenic temperatures into a practical, compact opto-electronic component emitting coherent radiation at room temperature useful for many applications. Today, diode lasers can be found in applications ranging from bar-code readers and laser pointers to high-resolution trace gas monitors and cooling and trapping of atoms, and they continuously find applications in everyday life as well as in different research areas.

For spectroscopic use, added benefits of the diode laser include, e.g., high spectral purity, high wavelength stability, uncomplicated wavelength tuning, and excellent modulation capabilities. Although the available emission wavelengths are almost exclusively dictated by the demands in the communication and consumer electronic market, the rapid development of new structures, devices and wavelengths are still beneficial for spectroscopic applications. Increased wavelength coverage, higher output power, better reliability, and lower price are results of this development.

An extremely wide variety of diode lasers has been developed, from single-stripe low-power diode lasers to multi-stripe high-power units. In the following description only single-stripe, moderately powered (5-200 mW) diode lasers are considered. This chapter starts with a short historical overview, and then continues with a discussion of important features regarding diode laser use in spectroscopy. A brief overview of available diode lasers and their wavelength coverage is also given. The basic aspects of the physics of diode lasers have been covered in many text books, and for a more detailed description the reader is referred to [2.1-2.3]. A comprehensive survey of diode laser device structure, development trends and areas of application has been given in [2.4]. Although diode lasers are extremely well suited for spectroscopy, they still have some limitations for certain applications, e.g., all free-running diode lasers have a limited continuous tuning range and some also exhibit longitudinal multimode behaviour. These issues are considered at the end of this chapter, discussing external cavity diode lasers.

2.1 Historical perspective

In 1962, only two years after the first (ruby) laser was demonstrated, four American research groups announced, almost at the same time, that they had achieved laser action in semiconductor junctions [2.5-2.8]. Three of the groups demonstrated coherent radiation in the near-infrared around 840 nm from a forwardly biased GaAs *p-n* junction [2.5,2.6,2.8], while the fourth group generated visible radiation at 710 nm by using a different semiconductor composition, $GaAs_{1-x}P_x$ [2.7]. Diode lasers at several different wavelengths were soon realised by implementing *p-n* junctions of other semiconductor materials, e.g., by using a lead salt compound (PbTe) the first diode laser emitting mid-infrared radiation at 6.5 μm was realised in 1963 [2.9]. All of these early diode lasers were homostructure devices, meaning that each laser was fabricated with only one semiconductor material. This is not an efficient laser structure, and in order to achieve laser action, a high threshold current density was needed. Therefore they had to be operated in a pulsed mode at cryogenic temperatures to avoid catastrophic failure caused by heat build-up. Although it was suggested already in 1963 [2.10,2.11] that lasing action in semiconductors could be improved by replacing the simple *p-n* junction with multiple semiconductor layers of different composition, it was not until 1970 that the semiconductor technology had matured enough to make it possible to manufacture the first double-heterostructure room-temperature operated continuous-wave diode lasers [2.12,2.13]. Composed of alternate layers of $Al_xGa_{1-x}As$ and GaAs, these lasers had a considerably lower threshold current and emitted coherent radiation at about 860 nm.

In the late 1970's a considerable interest was focused on the wavelength region between 1.0 μm and 1.6 μm because it was then realised that optical fibres have the lowest material dispersion (1.3 μm) and loss (1.55 μm) in this region. The first room-temperature operated telecommunication laser based on InGaAsP emitting at 1.3 μm was introduced in 1977 [2.14] and at 1.55 μm in 1979 [2.15-2.18]. During the same time a great effort was made to produce and manufacture better and more efficient laser types emitting light around 780 nm. The technology was based on the same structures as in 1970, but much better confinement of the laser light in the laser cavity could be obtained. This process was especially driven by the demand for cheap and reliable light sources to be used in audio disc players, and the first compact disc players were introduced by Philips and Sony in the fall of 1982. The strive for shorter wavelength lasers, to be used in, e.g., laser printers (photosensitive materials are more sensitive at shorter wavelengths), bar code readers (to replace HeNe lasers), and optical memories (data can be more densely packed), has lead to the introduction of room-temperature operated diode lasers at 670-680 nm in 1985 [2.19,2.20], at 630 nm in 1991 [2.21-2.23], and at 400 nm in 1997 [2.24]. Further developments in the diode lasers market towards even shorter wavelengths and also higher power and better reliability are most likely to occur. A very interesting historical survey on the

diode laser development until 1978 is given in [2.25], while more recent developments are described in [2.2].

2.2 Wavelength selection

The selection of a diode laser for a specific spectroscopic application can be a difficult task. While diode lasers have been operated from 400 nm to 30 μm, commercially available diode lasers are in practise limited to a number of wavelength regions within this range. Diode lasers operating in the visible and near-infrared region (0.4-2.0 μm) are based on group III (Al, Ga, In) and group V (N, P, As, Sb) semiconductor materials. Diode lasers emitting in the infrared (3-30 μm) region have as their basis group II-IV semiconductor materials, and are often referred to as lead salt diode lasers because many of them contain lead. Table 2.1 shows some of the semiconductor compounds used in diode lasers, and possible emission wavelengths. However, the commercial availability of diode lasers in the indicated regions is limited, and currently the upper limit for group III-V diode lasers is around 2 μm. A sample of molecules absorbing in the different wavelength regions are also included in Table 2.1. In particular, we note the following molecular absorptions; NO_2 at several wavelengths in the visible region, O_2 around 760 nm, H_2O around 980 nm, and hydrocarbons around 3.4 μm. These overlaps are used in Papers IV and VI.

Table 2.1: *Diode laser materials, emission wavelengths, and absorbing species.*

Compound	*Wavelength (nm)*	*Absorbing species*
GaN	390-410	NO_2
ZnSe	525	NO_2
$(Al_xGa_{1-x})_yIn_{1-y}P$	630-690	NO_2
$Al_xGa_{1-x}As$	750-895	O_2, H_2O, NH_3
GaAs	904	
$In_{0.2}Ga_{0.8}As$	980	H_2O
$In_{1-x}Ga_xAs_yP_{1-y}$	1100-1650	CO, CO_2, C_2H_2, CH_4, NH_3
$In_{0.73}Ga_{0.27}As_{0.58}P_{0.42}$	1310	
$In_{0.58}Ga_{0.42}As_{0.9}P_{0.1}$	1550	
InGaAsSb	1700-3700	Hydrocarbons, CO, CO_2, N_2O, ...
PbEuSeTe and PbSSe	3300-8000	Hydrocarbons, SO_2, NO_2, NO,...
PbSnTe and PbSnSe	6300-29000	Hydrocarbons, SO_2, NO_2, ...

The strong molecular fundamental rotational-vibrational absorption bands in the middle infrared region (2-15 μm) of several atmospheric species make the lead salt diode lasers especially attractive for spectroscopic applications and, in fact, many scientific trace gas spectrometers incorporate a diode laser of this type [2.26,2.27]. However, these lasers operate only at cryogenic temperatures which increases device

cost and makes operation and handling more complex. In addition, the reliability of these lasers for practical spectroscopic implementations has for a long time been regarded as unacceptable among spectroscopists. The infrared diode lasers are only produced in small batches and at a much lower level of manufacturing sophistication, and cannot benefit from the high manufacturing capabilities as the visible and near-infrared diode lasers. Infrared lasers have not been used in the work presented in this thesis, and the following presentation will instead focus upon the visible and near-infrared diode lasers.

The diode laser technology in the visible and near-infrared wavelength range (about 400 nm to 2 μm) offers 5-200 mW of narrow-band tuneable radiation at room temperature from small and low-cost devices, developed for the use in communication and consumer electronic markets. Additionally, fibre-optic technology, and inexpensive auxiliary equipment such as low-noise current sources and detectors, thermoelectric coolers, visible optics etc. are readily available. Since the molecular transitions in the visible and near-infrared are weak rotational-vibrational overtones and combination bands, a modulation technique is often employed to compensate for the two to three orders of magnitude loss in sensitivity. Different modulation techniques using diode lasers are outlined in Chapter 4. Utilising nonlinear optical frequency conversion the available wavelength range can be extended to allow molecular and atomic spectroscopy in the middle infrared and the ultraviolet spectral regions. Aspects of frequency conversion are considered in Chapter 5. Many atomic species have transitions in the ultraviolet, visible and near-infrared regions and many atomic spectroscopy experiments have been performed. Atomic diode laser spectroscopy is discussed and reviewed in [2.28,2.29]. In the present work, atomic diode laser spectroscopy has been extended to potassium, lead and mercury, absorbing at 404 nm, 406 nm and 254 nm, respectively (Papers II, III and V). Short wavelength diode lasers, such as the violet and the blue ones used in the present work, are also very suitable for inducing fluorescence in organic materials. Applications in environmental and medical monitoring are presented in Paper VII.

2.3 Diode laser characteristics

2.3.1 Principle of operation

The construction of a typical diode laser of today is shown in Fig. 2.1. The laser is based on the double heterostructure, mentioned in the Section 2.1, where the active (laser) medium is sandwiched between two other semiconductor materials with higher bandgap energies. Homostructures, due to their inefficiency, are no longer used. Laser light in a diode laser is generated by applying a forward bias current to the *p-n* junction. This produces electrons and holes in the active region between the *p*- and *n*-type materials. A population inversion between the conduction and valence bands can thus be achieved, and stimulated emission will result due to electron-hole

recombination. The emission wavelength of the diode laser light is determined by the bandgap of the semiconductor material (see Table 2.1).

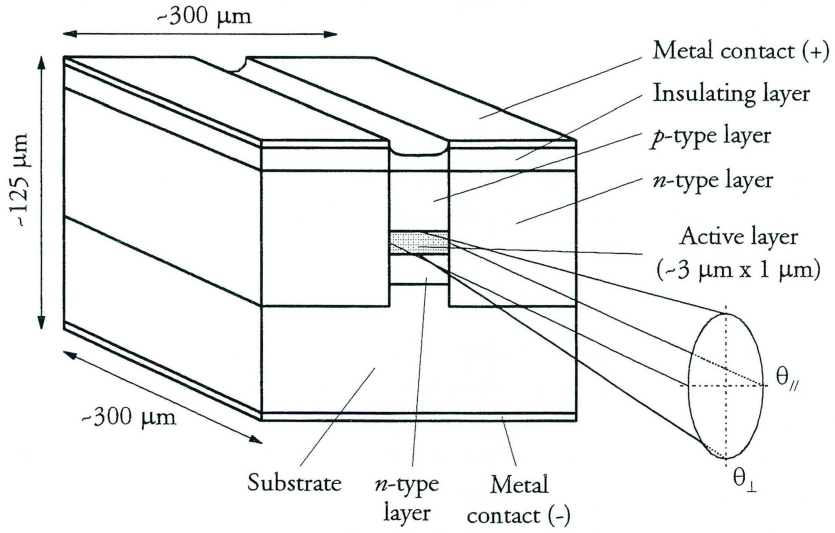

Fig. 2.1 *Illustration of the construction of a modern index-guided diode laser showing the different layers and typical dimensions. The small dimensions and the rectangular shape of the active medium result in a divergent and asymmetric output beam.*

To assure continuous laser action, an optical resonator is needed, and this is formed by the cleaved facets of the semiconductor material, having a typical reflectance of about 30% (the refractive index of AlGaAs is about 3.6, yielding a reflectivity to air of $R = [(3.6\text{-}1)/(3.6\text{+}1)]^2 = 32\%$). The sandwiched double heterostructure confines the light in a narrow channel along the *p-n* junction. In the other lateral direction, perpendicular to the *p-n* junction, the light can either be confined by spatial variations of the injection current (gain guided) or by spatial variations in the refractive index of the material structure surrounding the *p-n* junction (index guided). Historically, gain-guided diode lasers have been easier to produce, but today, index-guided diode lasers are the most common laser type, and present better optical characteristics and lower threshold current. An enormous variety of different index- and gain-guided structures has been implemented, and is comprehensively covered in [2.2,2,4].

Since stimulated emission has to compete against absorption processes in the active region, the laser will not emit coherent light until the current exceeds a certain value, the threshold current. At low currents, diode lasers act as light emitting diodes, since the losses are then too high to get population inversion. When the current equals the threshold value, population inversion is achieved and coherent light will be emitted. Above the threshold current, the laser output power varies linearly with current. A

threshold current around 20-50 mA and an operating current around 20-200 mA are typical for most 5-200 mW diode lasers. By applying a reduced reflectance coating on the output facet (typically between 2 and 20%), and a high-reflectance coating on the back surface of the diode laser, higher output powers are available than from lasers with only cleaved facets.

2.3.2 Beam characteristics

The output beam from a diode laser is divergent, asymmetric and astigmatic, which means that optical components especially adapted for diode lasers have to be used to make the beam useful for spectroscopy. Since diode lasers are usually sealed on the output end by a planar glass window, spherical aberration is introduced when the divergent output beam passes through the window.

The large divergence and asymmetric shape of the output beam is due to the small cross-sectional dimensions and rectangular shape (about 3 μm x 1 μm) of the active region of the diode laser. Typical divergence angles (full width at half the intensity) are 10-20° in the plane of the *p-n* junction and 30-40° in the perpendicular direction ($\theta_{//}$ and $\theta_{\perp}$, respectively, in Fig. 2.1) A benefit of the small lateral size of the active region is that it ensures a spatial profile of an essentially single transverse mode, resembling a Gaussian profile. The astigmatism occurs because of the longitudinal separation between the individual diode laser emission points and is due to a directional dependence on the refractive indices in the cavity.

The output beam is collimated using a lens with a high numerical aperture (typically 0.5 or better) and a short focal length. A singlet lens will introduce significant spherical aberrations, and therefore one often uses multiple-element spherical glass lenses or moulded aspheric lenses. These lenses can be manufactured to also compensate for the spherical aberrations originating from the protective window. Throughout the work presented in this thesis, moulded glass aspheric lenses have been used. It was found that the use of such lenses introduces less interference fringes in absorption measurements than otherwise encountered. The asymmetry is no problem in most spectroscopic studies as long as the whole beam passes the absorbing volume and is focused onto the detector. When two beams should overlap, as in nonlinear optical frequency conversion, it is essential for the conversion efficiency of the process that the two beams overlap as well as possible. The elliptical beam can be made circular using either a cylindrical lens or an anamorphic prism pair. Anamorphic prism pairs were used in Paper VI, and the construction and functioning of this component is illustrated in Fig. 2.2.

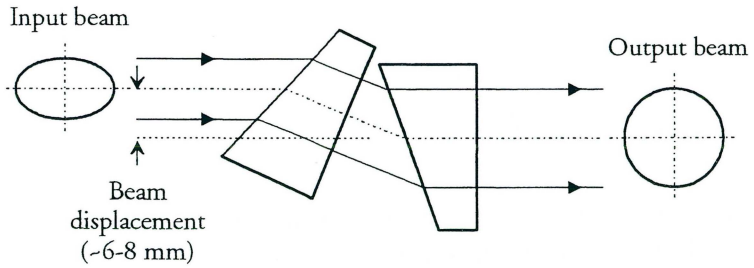

Fig. 2.2 *Schematic illustration showing the working principle of an anamorphic prism pair. The prism pair transforms an elliptical beam into a circular beam, either by expanding, or decreasing the beam in one direction only. The prism pair shown here expands the minor axis to make a circular beam. The transformation is always accompanied by a small displacement of the beam. The amount of magnification (or demagnification) can be varied by changing the incident angle. The two identical prisms are mounted with an incident angle close to Brewster's angle to minimise reflection losses and maintain the state of polarisation.*

An important factor for how well the diode laser beam can be collimated and focused is the astigmatism, which for most visible and near-infrared index-guided diode lasers of today is small. Gain-guided diode lasers exhibit larger astigmatism. The astigmatism limits the ability to focus the beam to a small spot size. However, since the diameter of a normal photodiode for the visible and near-infrared region ranges from about one mm to several mm, focusing the slightly astigmatic beam onto the detector surface does not constitute a problem.

In many applications (e.g., nonlinear optical frequency conversion as in Papers V and VI) it is essential to have control over the polarisation of the radiation. The output radiation from most diode lasers is linearly polarised along the *p-n* junction plane. The polarisation ratio is typically 100:1 or more when the diode laser is operated near its maximum power. At low operating currents the share of unpolarised light due to spontaneous emission is higher and consequently, the polarisation ratio decreases.

2.3.3 Spectral emission

Diode laser can be divided into two main categories regarding their spectral emission properties, featuring single or multiple longitudinal mode operation. The spacing of the longitudinal cavity modes in a diode laser is given, as for all Fabry-Perot type cavities, by

$$\Delta\nu = \frac{c}{2nL} \tag{2.1}$$

or

$$\Delta\lambda = \frac{\lambda^2}{2nL}\left(1-\frac{\lambda}{n}\frac{\partial n}{\partial\lambda}\right)^{-1} = \frac{\lambda}{2n_g L}, \tag{2.2}$$

where c is the speed of light, λ is the wavelength, n the refractive index of the semiconductor material, L the cavity length, and n_g is referred to as the group refractive index. The typical longitudinal mode spacing (free spectral range) of diode lasers is around 150 GHz (using n=3.6 and L=300 µm). Since the laser cavity is much longer than the lasing wavelength, several longitudinal modes are possible. It is the gain profile of the semiconductor material that determines how many modes can lase at the same time. Depending on the processing technology and wavelength, the diode laser features more or less multimode behaviour. Index-guided diode lasers typically emit light in a single longitudinal mode, while gain-guided units often exhibit multimode operation. It is also a well-known fact that the first diode lasers emitting in a new wavelength region exhibit mostly multimode operation. When finally the processing technology matures, single-mode operation becomes more dominant. Multimode behaviour can be problematic in most spectroscopic applications. In measurements on molecules, with many close-lying lines, multimode behaviour is unacceptable since several transitions are probed at the same time, making it impossible to accurately determine the specific absorptions. For atomic physics experiments, multimode behaviour is still not wanted but could be acceptable since atoms frequently have large spacings between their transition lines, and only one transition is probed by a selected diode laser mode while the others run idle. An additional problem in spectroscopic measurements on atoms and molecules is presented by the linewidth of the light source, which can largely affect the determination of absorption lineshapes and linewidths. Single-mode diode lasers typically exhibit linewidths in the range 50-100 MHz, while multimode diode lasers, due to a less sophisticated structure, can have linewidths of several hundred MHz. In fluorescence studies on solids and liquids, or biological material such as leafs or tissue, as presented in Paper VII, neither the longitudinal mode operation nor the linewidth has any practical importance at all. This is because these materials exhibit broad absorption and fluorescence bands. The effect of external optical feedback into the diode laser cavity to enhance the spectral purity is discussed in Section 2.4.

2.3.4 Wavelength tuning

One of the most important characteristics of a diode laser for atomic and/or molecular spectroscopy is its tunability. The wavelength of a diode laser can be tuned by altering the temperature or by varying the drive current. A change in the drive current changes the junction temperature (Joule heating). The wavelength changes because of the

temperature dependence of the bandgap, which shifts the gain curve. A further influence is the temperature dependence of the refractive index, which alters the optical path length in the cavity. These two temperature dependencies are quite different; e.g., in an AlGaAs diode laser, the gain curve tunes about 0.25 nm/°C and the changes in the optical length (refractive index) of the cavity tunes about 0.06 nm/°C. This results in a temperature-wavelength tuning curve that consists of several continuous tuning ranges, which are interrupted by sudden wavelengths jumps, referred to as mode jumps. A typical tuning curve for a 5 mW 760-nm AlGaAs diode laser is displayed in Fig. 2.3. The slope of the continuous tuning ranges corresponds to the tuning of that particular longitudinal cavity mode while the mode jumps correspond to a jump from one longitudinal mode to another, not necessarily the one next by, due to the shift in the gain curve. The mode jump behaviour of Fabry-Perot -type diode laser makes a large portion of the total wavelength range covered by a particular diode laser inaccessible. In practice a continuous tuning range of 20-80 GHz before the diode laser jumps to the a different longitudinal mode is typical for most lasers operating in the visible and near-infrared region. The maximum continuous tuning range corresponds to approximately half the free spectral range (the longitudinal mode spacing) of the diode laser. The mode jump behaviour is particularly frustrating when selecting diode lasers for atomic physics experiments. Most often the diode laser will exhibit a mode jump at the transition frequency of interest! Therefore, several diode lasers have to be purchased, and hopefully one or two will tune continuously at the transition frequency. With molecules no such problem exist in concentration measurements, since there will always be lines where the diode laser tunes continuously. In theory, the laser temperature can be tuned between 0-60°C (some diode lasers can be tuned up to 85°C), by using a Peltier element in close connection to the diode laser capsule. In practise though, one usually does not go below 5-10°C or above 50°C, to avoid water condensation and thermal degradation which significantly shortens the diode laser lifetime.

Typically, coarse wavelength tuning of a diode laser is accomplished by changing the temperature around the diode laser capsule, while fine tuning is realised by changing the drive current. A wavelength scan over, e.g., an absorption profile can be made by changing the temperature, but since temperature tuning is slow, it is instead often made by superimposing a current waveform (saw-tooth, rectangular, sinusoidal) at high repetition rates on the operating current of the diode laser. The wavelength is thus repetitively scanned allowing real-time monitoring of the signals during acquisition and for optimising system performance. By the use of jump-scanning, a technique in which a specially produced waveform with current jumps is applied to the diode [2.30], it is possible to measure multiple transitions from different gas species in one recording.

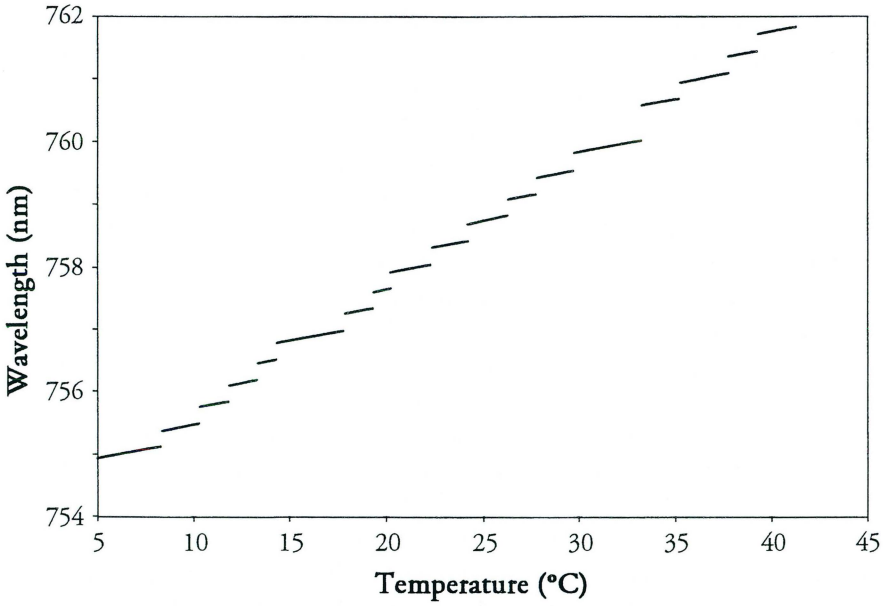

Fig. 2.3 *Wavelength as a function of temperature for an AlGaAs diode laser. The maximum continuous tuning range for this diode laser is about 0.15 nm (80 GHz).*

2.3.5 Modulation

One of the important advantages of diode lasers over other optical sources is that their amplitude and frequency can be modulated very easily and rapidly by changing the injection current. One of the modulation aspects have been discussed above, namely to scan the wavelength. Another application is in optical fibre communication, where the light can be switched on and off very quickly. A third application for modulation is to increase the sensitivity in optical measurements, e.g., absorption spectroscopy (frequency modulation). A strong reason for frequency modulation is to move the detection band into a higher frequency region, where the noise of different origins is strongly reduced. Different modulation techniques using diode lasers are further outlined in Chapter 4.

2.4 External cavity diode lasers

Although very unique in several aspects, a free-running diode laser is not suited for every application, since the mode jumps might be intolerable, the multimode behaviour unacceptable and/or the linewidth of 50-100 MHz too large. Applications requiring a very narrow linewidth, continuous tuning range, and/or single longitudinal mode operation include, e.g., high resolution spectroscopy, laser cooling and trapping, optical pumping, metrology and photon echoes. Fortunately, the spectral properties of a free running diode laser can be improved by exploiting its sensitivity to optical feedback.

Two main schemes utilising optical feedback for improving the spectral characteristics of free-running diode lasers can be distinguished; either coupling to an external high-finesse cavity [2.31] or to a diffraction grating [2.32]. These two schemes correspond to weak and strong feedback, respectively. The use of weak dispersive feedback from a high-finesse cavity, can result in a very narrow linewidth, but at the expense of a high level of technical complexity which limits the practical applicability. The other scheme, using strong dispersive feedback from a diffraction grating is much simpler to realise, and can, combined with an enlarged resonator, conveniently be used for wavelength tuning without mode jumps and linewidth narrowing. This arrangement, in which light diffracted from a grating is resonantly coupled back into the diode laser is commonly referred to as just an external cavity diode laser. Wavelength tuning to any desired wavelength within the gain profile of the semiconductor material using such techniques can be accomplished.

The two most prevalent designs using strong feedback from a grating are based on either the Littrow or the Littman configuration. In the present work, the Littrow configuration has been used in Papers II, V and VIII. The two configurations are schematically illustrated in Fig. 2.4. Descriptions of the two configurations are presented in [2.33-2.36] and [2.37-2.40], respectively. Common to both configurations is that the first diffraction order of the grating is coupled back into the laser and that the zeroth reflected order is the output. The wavelength is tuned by moving the grating in the Littrow configuration and the external mirror in the Littman design. The advantage of the Littrow configuration is its simplicity and compactness, while a disadvantage is that a change in the grating angle produces an angular displacement of the output beam. This displacement can be reduced if the output beam is reflected by a mirror attached to the grating with the surfaces parallel. The Littman configuration is somewhat more complex, but since the grating position is fixed, and wavelength tuning is accomplished by moving the mirror, the position of the output beam is not altered during tuning. Thus, the Littman configuration is often the preferred choice for large wavelength scans.

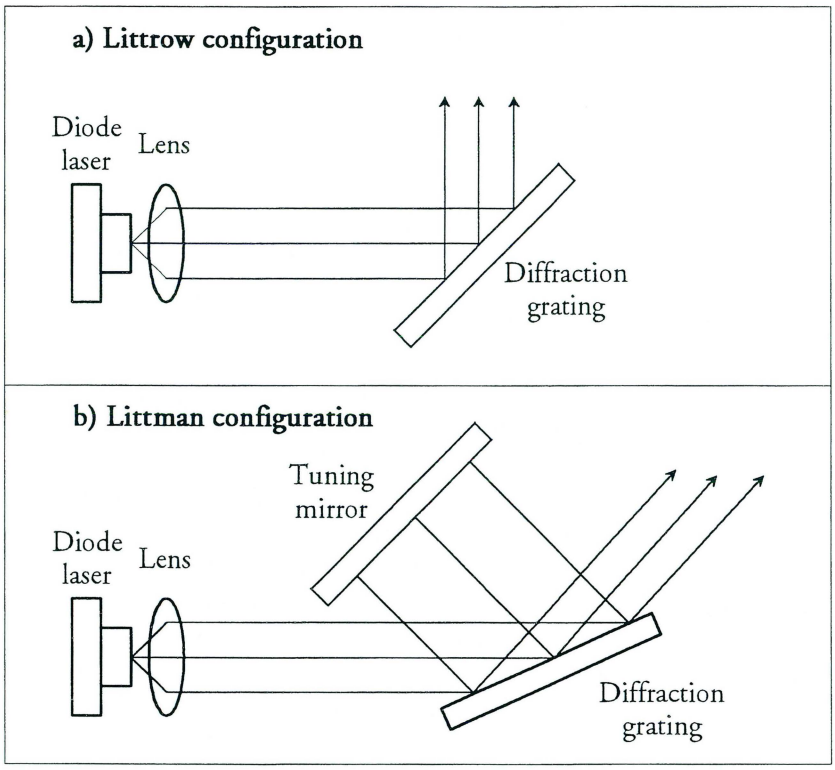

Fig. 2.4 *Schematic illustration of external cavity diode laser designs using a) the Littrow and b) the Littman configuration.*

True mode-hop free tuning over the gain curve of the semiconductor material is only possible with anti-reflection coated diode lasers. Most external cavity implementations use diode lasers where the front facet is anti-reflection coated, with a residual reflection of 10^{-3} or less. The low reflectivity of the output facet means that the diode laser cannot lase without the resonantly enhanced feedback from the grating. The longitudinal mode structure is thus determined by the length of the external cavity and not by the length of the diode laser. Since the external cavity length is much longer than the diode laser cavity, the spacing of the external cavity modes is much smaller, and large continuous wavelength ranges of several tens of nanometers can be obtained by rotating the grating in the Littrow or the mirror in the Littman configuration around a carefully selected pivot point [2.37,2.41-2.43] so that the peak of the grating gain function exactly follows the same external cavity mode during tuning [2.39,2.40,2.44]. However, if a mirror/grating rotation around an arbitrary point is chosen, the diode laser will discontinuously tune over the gain curve of the semiconductor material.

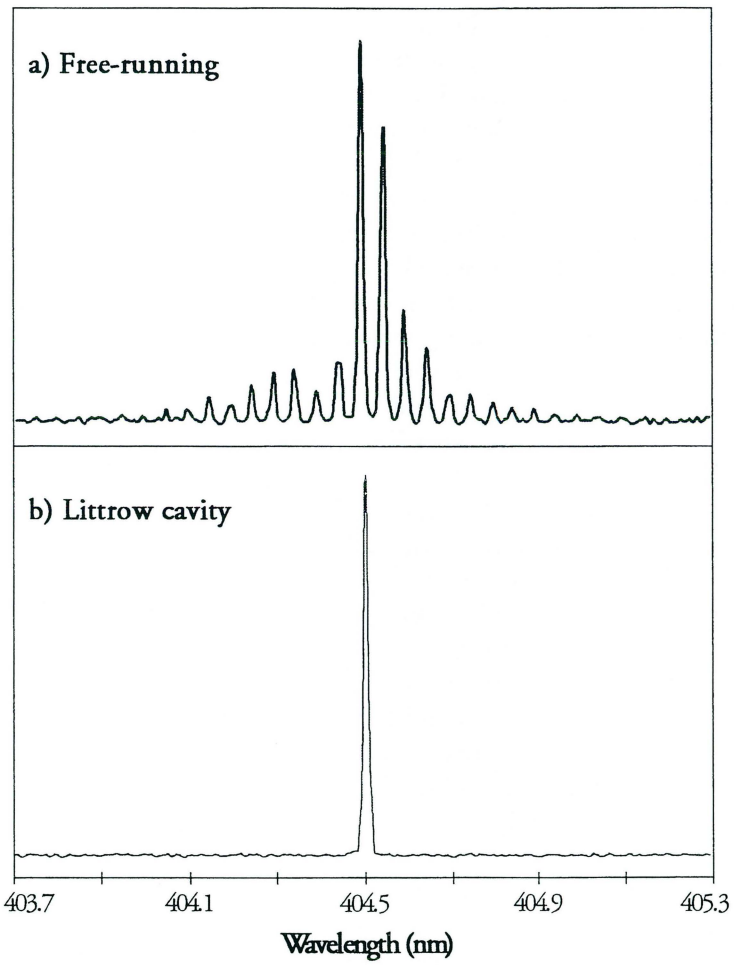

Fig. 2.5 *Diode laser output spectra when the diode laser is operating with and without an external cavity. A Nichia blue diode laser was used.*

When commercially available diode lasers are used in an external cavity, either diode lasers with uncoated facets or diode lasers with a high-reflectance coating on the back facet and a reduced reflectance coating on the output facet, the longitudinal modes of the solitary diode laser remain essentially unchanged. The cavity mode spacing of the compound diode laser - external cavity system is still determined by the length of diode laser, and the back-reflected light from the grating enhances one of these longitudinal modes and suppresses the other modes. Emission spectra from a diode laser with and without grating stabilised feedback (Littrow configuration) are shown in Fig. 2.5 (Paper II), clearly illustrating this longitudinal mode enhancement.

In addition to longitudinal mode selection and wavelength tuning, an external-cavity diode laser configuration also narrows the linewidth of the output radiation. Since the linewidth of a grating-stabilised external cavity diode laser has been found to decrease with the square of the external cavity length, it might appear advantageous to use very long external resonators to further narrow the linewidth. However, frequency and intensity drifts, due to mechanical and thermal instabilities typically set the limit on the minimum linewidth, and increasing the cavity typically induces more instabilities. Therefore, to achieve a narrow linewidth, a compromise between thermal and mechanical instability and cavity length must be found. External-cavity diode laser configurations with a cavity length of 5-10 cm can attain a short-term (μs to ms) linewidth of between 100-500 kHz and a long-term stability (minutes to hours) in the MHz range [2.35,2.38]. Within the present work a Littrow based external-cavity diode laser with a short-term linewidth of around 300 kHz and a long-term linewidth of 5-10 MHz has been constructed [2.36, Paper VIII].

Special types of diode lasers have been developed, utilising the principle of selective wavelength feedback; the distributed feedback (DFB) and the distributed Bragg reflector (DBR) diode lasers. In these devices, a frequency selective grating is incorporated into the cavity structure. The DFB laser includes a grating within the active region, while the DBR laser incorporates the grating outside of the active region. These lasers exhibit pure single-mode operation and wavelength tuning without mode jumps. However, since DFB and DBR diode laser wavelengths follow the temperature dependence of the refractive index with a much smaller wavelength shift than the gain curve of the semiconductor material (see Section 2.3.4), the maximum wavelength tuning is typically of the order of a few nanometers.

Finally, it is important to note that optical feedback induced by large bandwidth optical components, such as glass plates, lenses, mirrors in the optical path, etc. as opposed to a wavelength selective grating with a narrow bandwidth, constitutes an unwanted effect that disturbs the longitudinal mode structure of the diode laser. It can induce mode jumps, broaden the linewidth and cause unstable output power. Common practise in all experiments involving free-running diode lasers is thus to slightly angle all transmissive optics and detector surfaces, to reduce the back reflections to a minimum.

3. Absorption spectroscopy

Absorption spectroscopy can provide the means for quantitative determination of concentration, temperature and pressure of gaseous species. By tuning the laser wavelength over single or multiple absorption lines of the species under investigation, a very high accuracy and precision in the measurements can be obtained. This requires a precise theoretical model of the detected signal which accurately describes the absorption line under varying environmental conditions. Different line profiles and line broadening mechanisms and their connection to temperature and pressure will be presented in this chapter. Aspects of achieving a high species sensitivity and selectivity are also considered.

3.1 Absorption relations

The Beer-Lambert law governs all absorption measurements. It relates the recorded intensity $I(\nu)$ of an electromagnetic wave at frequency ν transmitted through an absorbing gas volume to the original intensity $I_0(\nu)$ according to

$$I(\nu) = I_0(\nu)\exp\left[-\sigma(\nu)NL\right], \qquad [3.1]$$

where $\sigma(\nu)$ is the frequency-dependent absorption cross-section per molecule (cm^2/molecule), N is the density of the absorbing molecules in molecules/cm^3, i.e. the absolute gas concentration, and L is the absorption path length in cm. Eq. 3.1 is also often written with the absorption coefficient $\alpha(\nu)$ in cm^{-1}, i.e. it is given as $\alpha(\nu)=\sigma(\nu)N$. The overall strength of an absorption line is given by the line strength S, also referred to as the line intensity, and is the integral of the absorption cross-section over the frequency range of the line,

$$S = \int \sigma(\nu)d\nu. \qquad [3.2]$$

The most commonly used unit for the line strength is cm^{-1}/(molecule cm^{-2}) but the abbreviated cm/molecule is sometimes also used. It is often convenient to decouple the strength and the shape of the absorption cross-section by introducing a lineshape function of unit area $g(\nu-\nu_0)$ according to

$$\sigma(\nu) = Sg(\nu - \nu_0), \qquad [3.3]$$

where ν_0 is the frequency at the line centre.

The lineshape function $g(\nu-\nu_0)$ is both temperature and pressure dependent due to Doppler and pressure broadening, while the line strength S, which includes the Boltzmann population factor, is a function of temperature, but not of pressure.

There is an alternative, but equivalent way of expressing the Beer-Lambert law, namely

$$I(\nu) = I_0(\nu)\exp\left[-\sigma_P(\nu)PL\right], \qquad [3.4]$$

where $\sigma_P(\nu)$ is the absorption cross-section in cm^{-1}/atmosphere and P is the partial pressure of the absorbing species in atmospheres (atm.). This expression relates the partial pressure, i.e. the relative concentration and not the absolute concentration to the transmitted intensity. The line strength S' (in units of cm^{-2}/atm.) related to this expression of the Beer-Lambert law is defined according to $\sigma_P(\nu) = S'g(\nu-\nu_0)$.

By the Beer-Lambert law according to Eq. 3.1, the absorbance a is given by

$$a = \ln\frac{I_0(\nu)}{I(\nu)} = \sigma(\nu)NL. \qquad [3.5]$$

For a given value of the absorbance a, and a given signal-to-noise ratio, we can see that sensitive concentration (N) measurements can be achieved by increasing the product $\sigma(\nu)L$. Thus, the sensitivity can be increased by choosing a wavelength, where the cross-section is large or by using long path lengths. Issues regarding the absorption cross-section will be discussed in Sections 3.2 and 3.3, while methods to increase the path length are considered in Section 3.4. Aspects of how to reduce the noise level by modulation techniques and thereby increasing the sensitivity, are considered in Chapter 4.

Throughout the following presentation, absorption molecular spectroscopic data are taken from the *HITRAN* molecular spectroscopic data base [3.1]. Molecular spectroscopic data from 37 different atmospheric gases and pollution gases in the spectral range 0-23000 cm^{-1} are collected in this data base. Another very good source of molecular spectroscopic data is the *Journal of Quantitative Spectroscopy and Radiative Transfer.*

3.2 Line profiles

The lineshape function $g(\nu-\nu_0)$ describes the spectral variations of the light interaction with an absorbing species, and depends upon the conditions under which the measurement is made (pressure, temperature, gas composition, etc.). An important parameter contained within the lineshape function is the halfwidth at half its maximum value (HWHM), often denoted by $\Delta\nu$. The line broadening mechanisms can, depending on pressure, be divided into three main regions. At high pressures collisional broadening dominates giving rise to a Lorentzian lineshape, at low pressures Doppler broadening dominates and the lineshape becomes a Gaussian, while at intermediate pressures when neither collisional nor Doppler broadening dominates, the lineshape is best described as a convolution of a Lorentzian and a Gaussian line profile known as the Voigt profile [3.2].

Collisions between the absorbing molecules lead to a Lorentzian line profile, which is described as

$$g_L(\nu-\nu_0)=\frac{\Delta\nu_L}{\pi}\frac{1}{(\nu-\nu_0)^2+\Delta\nu_L^2} \qquad [3.6]$$

with a halfwidth that depends upon pressure according to

$$\Delta\nu_L=\sum_i \gamma_i p_i\,, \qquad [3.7]$$

where γ_i and p_i are the pressure broadening coefficients in cm^{-1}/atm and the partial pressures in atm, respectively, of the species present in the absorbing volume. The linewidth of a pressure-broadened absorption line thus consists of both a self-broadening contribution from the gas species probed and a foreign-gas broadening due to the other gases present in the probed volume. The pressure-induced linewidth depends also on temperature according to

$$\Delta\nu_L(T)=\Delta\nu_L(T_0)\left(\frac{T_0}{T}\right)^n\,, \qquad [3.8]$$

where T_0 is a reference temperature (typically 296 K), and the power n is both a gas- and a transition-specific parameter, i.e. it can even have different values for different transitions of the same gas. Although a value of the order of 0.5 is typical, the three species detected in Paper VI; molecular oxygen, water vapour and methane have the values of 0.70, 0.66, and 0.75, respectively.

Doppler broadening which is due to the thermal motion of the absorbing particles, is described by a Gaussian line profile

$$g_D(\nu-\nu_0)=\frac{1}{\Delta\nu_D}\sqrt{\frac{\ln 2}{\pi}}\exp\left[-\frac{\ln 2(\nu-\nu_0)^2}{\Delta\nu_D^2}\right] \qquad [3.9]$$

with a halfwidth $\Delta\nu_D$ given by

$$\Delta\nu_D=\nu_0\sqrt{\frac{2kT}{Mc^2}\ln 2}=3.581\times10^{-7}\,\nu_0\sqrt{\frac{T}{M}}\,, \qquad [3.10]$$

where ν_0 is the frequency at the line centre, T the absolute temperature, M the molecular mass, k the Boltzmann constant, and c the speed of light. As seen, the Doppler broadened linewidth, as opposed to the pressure-induced linewidth, increases with increasing temperature.

In the intermediate region, the line profile is accurately described by a Voigt profile, given by

$$g_V(\nu-\nu_0)=\frac{\Delta\nu_L}{\Delta\nu_D}\sqrt{\frac{\ln 2}{\pi^3}}\int_{-\infty}^{\infty}\frac{\exp\left[-\tau^2\ln 2/\Delta\nu_D^2\right]}{\Delta\nu_L^2+(\nu-\nu_0-\tau)^2}\,d\tau \qquad [3.11]$$

This integral has no analytical solution, and the Voigt line profile has therefore to be calculated numerically. A fast and efficient algorithm to compute the Voigt function can be found in, e.g., [3.3]. The Voigt function tends to a Lorentzian at high pressure and to a Gaussian at low pressure, and is thus the general form of the lineshape. Since the Voigt line profile has no analytical solution, no exact formula exists for the Voigt halfwidth $\Delta\nu_L$ either. An accurate empirical expression for $\Delta\nu_V$ as a function of $\Delta\nu_L$ and $\Delta\nu_D$ (with a claimed relative error of better than 0.02 %) has been given in [3.4]:

$$\Delta\nu_L=0.5346\Delta\nu_L+\sqrt{0.2166\Delta\nu_L^2+\Delta\nu_D^2}\,. \qquad [3.12]$$

However, a quick, time-saving estimate can be made by the following approximation

$$\Delta\nu_V=\sqrt{(\Delta\nu_D^2+\Delta\nu_L^2)}\,. \qquad [3.13]$$

A comparison of the Gauss, Lorentz and Voigt line profiles is shown in Fig. 3.1. All three profiles are calculated to have the same linewidth and each has an area of unity. The Lorentz and Doppler influences on the Voigt line profile were chosen so that $\Delta\nu_L=\Delta\nu_D$.

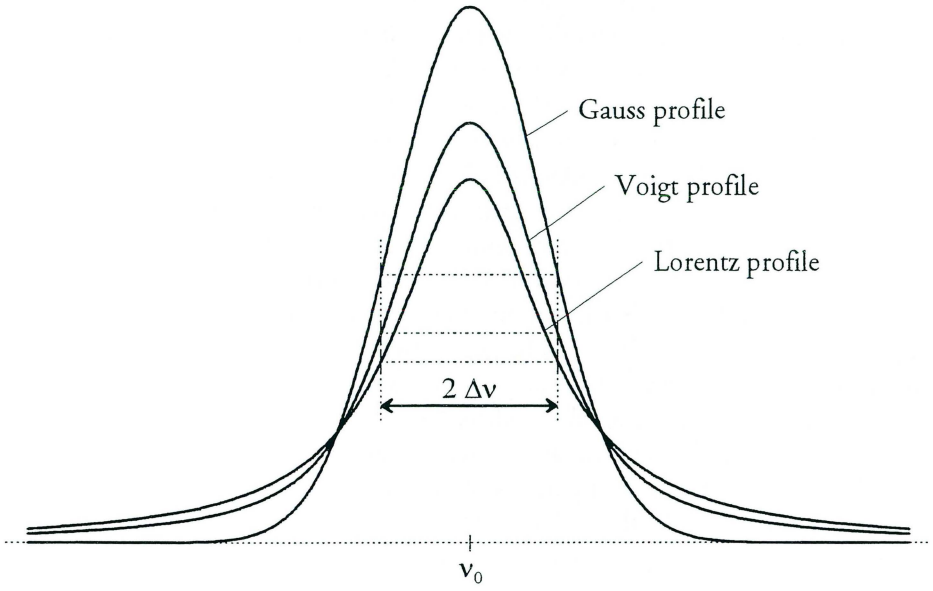

Fig. 3.1 *Doppler, Lorentz, and Voigt line profiles.*

Pressure-broadened linewidths are typically between 0.05 and 0.1 cm^{-1} (1.5-3 GHz) at atmospheric pressure. Self-broadening will only influence the pressure-broadened linewidth at high concentrations, and becomes significant at different concentrations for different gases. E.g., in Paper VI, the typical background concentration of methane in our laboratory was measured to 3 ppm, which corresponds to a partial pressure of 3×10^{-6} atm, and since the self-broadening and air-broadening of methane around 3.4 μm are typically 0.07-0.09 cm^{-1}/atm and 0.05-0.07 cm^{-1}/atm, respectively, the influence of self-broadening for methane is negligible at atmospheric pressure. For the strongly dipolar molecule H_2O, self-broadening will also have negligible influence on the pressure-broadened linewidth at normal concentrations in the atmosphere, but since H_2O has a self-broadening of 0.5 cm^{-1}/atm and an air-broadening of 0.1 cm^{-1}/atm. for the lines at 980 nm, the self-broadening will become significant at much lower relative concentrations.

Methane with M = 16 has for the lines around 2927 cm^{-1} (the lines studied in Paper VI) a pressure-broadened linewidth of 0.06 cm^{-1} and a Doppler-broadened linewidth of 0.0045 cm^{-1} at atmospheric pressure and a temperature of 296 K. This gives a Lorentz width/Doppler width ratio of about 13, and means that the Lorentz profile adequately describes the methane line profile at atmospheric pressure. Molecular oxygen, on the other hand, has a pressure-broadened linewidth of about 0.05 cm^{-1} at atmospheric pressure and a Doppler width of 0.014 cm^{-1} (M = 32) for the lines around 760 nm (ratio: 4), which means that the Voigt line profile better describes the lineshape of molecular oxygen. For the mercury (M = 200) transitions at 254 nm studied in Paper V, a pressure-broadened linewidth of 0.11 cm^{-1} at atmospheric pressure was estimated from simulations of spectra. Since the Doppler width is 0.017 cm^{-1} for mercury, the Lorentz profile again accurately describes the line profile. These examples of measurements at atmospheric pressure ranging from a transition frequency of 254 nm to 3.4 µm, and molecular masses from 20 to 200 show, that the profile to be used is largely dependent on both the molecule studied and the transition frequency. The profiles to be considered at atmospheric pressures are either of the Lorentz or the Voigt type. In the present work, measurements have also been performed in low-pressure gas cells, and the evaluation of the absorption lines in the atomic studies on potassium, lead and mercury (Papers II, III and V) used a Gaussian line profile. The evaluation of the methane lines at different pressures (Paper VI) used the Voigt line profile, with a fixed Doppler width and the pressure-broadened linewidth as an adjustable parameter.

Since the peak absorption of a molecular or atomic transition is inversely proportional to the pressure-broadened linewidth, pressure reduction is often beneficial in increasing the signal peak sensitivity, although the integrated absorbance remains constant. Also, as many closely spaced lines at atmospheric pressure tend to overlap, a reduction in linewidth also yields an increased specificity. This is clearly illustrated in the present work (Papers IV, V and VI) where both atmospheric and low-pressure gas cell spectra of NO_2, Hg and CH_4 have been recorded.

An important factor for an accurate determination of the true linewidth of a transition is the influence of the light source linewidth. As mentioned in Chapter 2, the typical linewidth of single-mode diode lasers (free running) is of the order of 50-100 MHz (0.0017 - 0.003 cm^{-1}). Thus, the linewidth of a single-mode diode laser is considerably narrower than any of the widths discussed here, both Doppler and pressure-broadened linewidths, and will not affect the linewidth determination.

To conclude this chapter on line profiles and line broadening mechanisms, we note that there exists also a natural linewidth which is always present and which is determined by the Heisenberg uncertainty principle. The energy of a state is only precisely defined if the lifetime of the energy state is infinite, and with a finite lifetime there will be a corresponding uncertainty in its energy. Typical natural lifetimes of

excited states in atoms and molecules range from μs to ns, corresponding to a natural linewidth in the range 0.1-100 MHz, and to be able to resolve these narrow linewidths in Doppler-free experiments, a free-running diode laser will often not be sufficient, and instead an external cavity diode laser has to be used.

3.3 Line strength

The line strength, as defined in Eq. 3.2, depends upon the temperature and not on pressure, and can be extrapolated to other temperatures T through

$$S(T) = S(T_0)\frac{Q(T_0)}{Q(T)}\exp\left[-\frac{E''}{k}\left(\frac{1}{T}-\frac{1}{T_0}\right)\right], \qquad [3.14]$$

where k is Boltzmann's constant, E'' is the energy of the lower state of the transition and T_0 is a reference temperature (296 K). Q(T) is the partition (sum) function given by the Boltzmann distribution for all possible energy states in the molecule

$$Q(T) = \sum_i d_i \exp\left[-\frac{E_i}{kT}\right], \qquad [3.15]$$

where d_i is the degeneration of energy level E_i. Expressions for the temperature dependence of the partition function are available [3.1]. A simplified expression for $Q(T_0)/Q(T)$ is $(T_0/T)^j$, where j = 1 for linear molecules and j = 1.5 for nonlinear molecules.

The line strength S' related by the absorption cross-section $\sigma_p(\nu)$, introduced in Eq. 3.4, according to $\sigma_p(\nu) = S'g(\nu-\nu_0)$, is connected to the line strength S through

$$S'(T) = S(T)N_0\frac{T_0}{T}, \qquad [3.16]$$

where N_0 is Loschmidt's number (2.479×10^{19} molecules/(cm^3 atm)) at the reference temperature T_0 =296 K.

Since the line strength defines the overall strength of an absorption line, a logical step to increase the sensitivity in absorption measurements on molecular species is to use lines with large line strengths. These are found in the middle infrared region (2-15 μm), where most molecules have fundamental rotational-vibrational transitions, and for some molecules also in the ultraviolet and visible region, where electronic transitions occur. Small line strengths are found in the near-infrared region, where overtone and intercombination bands are present. E.g., the methane transitions

around 2927 cm^{-1} studied in Paper VI have a line strength of about 2×10^{-20} $cm^{-1}/(molecule\ cm^{-2})$, while the line strength of the strongest transition around 1.65 μm (6060 cm^{-1}) is 1.3×10^{-21} $cm^{-1}/(molecule\ cm^{-2})$. The pressure-broadened linewidth at these two wavelengths are approximately equal, indicating that the peak absorption is about ten times larger at 2927 cm^{-1}.

3.4 Long path absorption

The Beer-Lambert law (Eq. 3.1) shows that one obvious way to improve the sensitivity in absorption measurement is to increase the path length, *L*. The aspect of path length will in this section be briefly discussed with reference to Fig. 3.2.

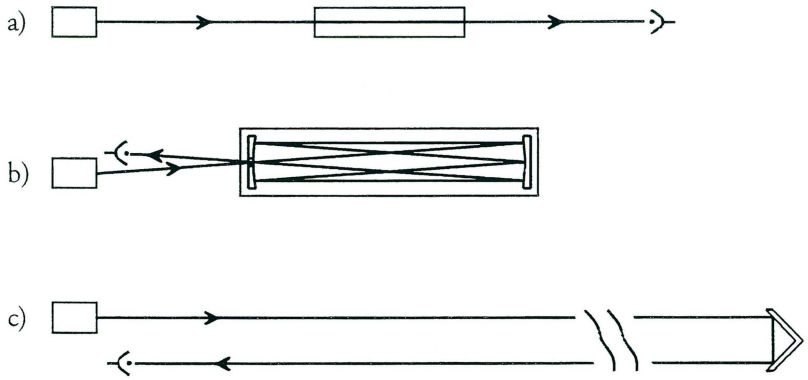

Fig. 3.2 *Three fundamental methods of conducting absorption measurements. a) Laboratory set-up for basic absorption measurements. b) Point monitoring using a multi-pass absorption cell. c) Remote sensing (long-path absorption).*

The set-up in Fig. 3.2a is a typical research laboratory arrangement used for fundamental studies of atomic or molecular transitions, often at low pressure and possibly also at high concentrations. Such a simple set-up has been used in absorption measurements performed within the present work, either for atomic spectroscopy (Papers II, III and V) or for convenient calibration of the remote sensing measurements (Papers IV and VI).

The other set-ups in Fig. 3.2 represent the two fundamental methods to achieve long path lengths in atmospheric sensing, either a multi-pass cell, which implements point sampling with path lengths of up to several hundred meters, or an open path double-pass system with a retroreflector. Two types of multi-pass cells are frequently used, the Herriot cell [3.5,3.6] or the White cell [3.7,3.8]. A variation of the Herriot cell achieving a longer path length for a given sampling volume using astigmatic mirrors has been developed [3.9], and is today commonly used in many trace-gas sensing

applications using diode lasers. In all multi-pass cell configurations, the sensitivity gained by increasing the path length is counter-acted by a reduced throughput of laser radiation. E.g., a multi-pass cell with 99% reflectivity mirrors and 100 passes (reflections) will exhibit a throughput of only 36%. A variety of the multi-pass cell concept is cavity ring-down spectroscopy [3.10,3.11] which can provide path lengths of more than 10 km from a one meter cell. This technique can be considered to be an extension of the intra-cavity absorption technique [3.12].

In the present work, multi-pass cells have not been used, since the emphasise has been on open-pass remote sensing applications and not on point monitoring. An advantage of free atmosphere monitoring is the absence of walls, gas extraction pipes etc., which makes the arrangements insensitive to sampling. Atmospheric turbulence can constitute a problem in open-air monitoring. By choosing a diode laser wavelength scanning rate of the order of 100 Hz or higher, problems with atmospheric turbulence, which typically occur at frequencies between 0.1 and 10 Hz, can be avoided. Another issue to be considered in remote sensing applications is the divergence of the light beam ($\theta \cong \lambda/d$). Using diode lasers, the beam size after collimation is about 1 mm × 3 mm. This in turn means that the beam size for a 630 nm diode laser (Paper IV) at a distance of 160 m would be about 10 cm × 3 cm. By expanding the beam in a telescope, the divergence will be reduced, and the beam is easier to collect at the detection side.

Apart from monitoring optical transmission in measurements of molecular and atomic absorption (absorption spectroscopy), other detection techniques can be employed, e.g., photo-acoustic spectroscopy [3.13,3.14] and opto-galvanic spectroscopy [3.15].

4. Modulation techniques

In order to improve the sensitivity and to effectively discriminate against background signals in absorption measurements some kind of modulation technique is employed. The fundamental concept of all modulation techniques is to shift the detection band to a high-frequency region, where the noise level is small. This also enables effective attenuation of low-frequency components by conventional filtering. The shift to a high-frequency region can be accomplished by either amplitude modulation (AM), frequency modulation (FM) or fast scan integration. An overview of the modulation techniques, and the different noise sources in diode laser spectrometry are presented.

4.1 Amplitude modulation

Amplitude modulation (AM) is accomplished by mechanically chopping the laser beam at frequencies not higher than a few kHz, which represents the highest modulation frequency of commercially available choppers. A typical AM set-up is shown in Fig. 4.1. AM is combined with phase-sensitive detection. The AM signal is detected by a lock-in amplifier operating at the chopper frequency while the diode laser wavelength is slowly scanned across the absorbing feature. The minimal detectable change in absorbance with this method is low, generally not better than 10^{-3}. The slow wavelength scan makes this method susceptible to environmental fluctuations, such as temperature changes and atmospheric turbulence along the laser beam path. However, advantages with this method are the very simple set-up and that the measured spectrum provides absolute calibration, since the absorption feature is recorded together with the off-absorption light intensity.

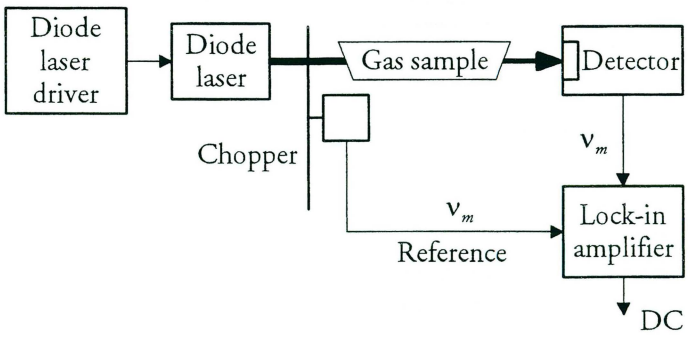

Fig. 4.1 *Illustration of a typical amplitude modulation (AM) arrangement using a diode laser and a mechanical chopper.*

4.2 Frequency modulation

Different frequency modulation (FM) techniques are very attractive in conjunction with diode lasers because of the ease with which such lasers can be modulated by applying an ac (modulation) current directly on the drive current. Typical FM set-ups using diode lasers are shown in Fig. 4.2.

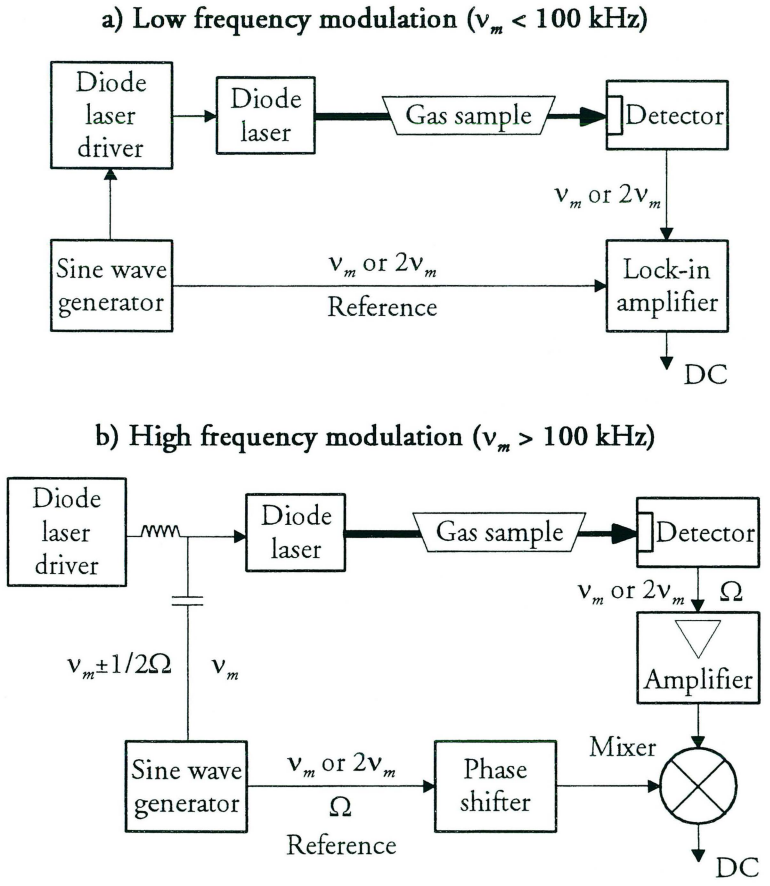

Fig. 4.2 *Illustration of the experimental set-up for frequency modulation techniques with diode lasers. The set-up in a) is applied for low modulation frequencies and the set-up in b) is used at high modulation frequencies. At high modulation frequencies, capacitive coupling of the modulation current to the drive current via a properly designed bias-T mounted close to the diode laser is used to impedance match the sine-wave generator (50 ohm) to the diode laser (about 5 ohm). The set-up used in a) is typically referred to as wavelength modulation spectroscopy.*

Generally speaking, modulation of the diode laser drive current leads to the generation of sidebands in the laser field, as show in Fig. 4.3. If no molecular absorption is present there is a cancellation of the beat notes prodded between the sidebands and the carrier. If the laser field is scanned across an absorbing feature, the balance is lost and a beat signal appears which is detected by frequency- and phase-sensitive electronics, either by a lock-in amplifier or by a mixer.

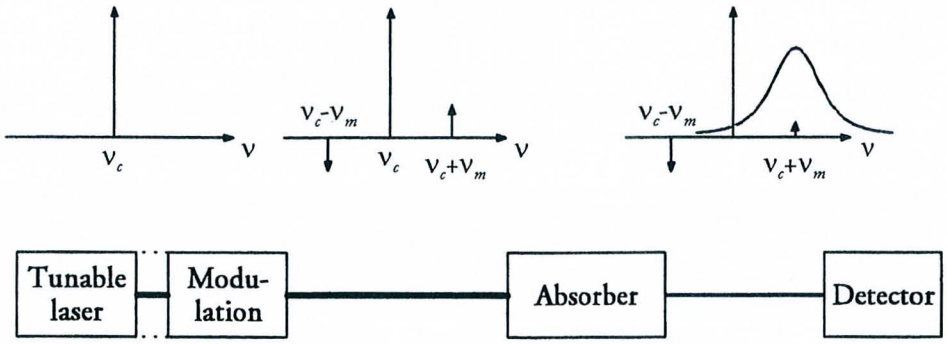

Fig. 4.3 *Schematic illustration of the generation of sidebands on an optical carrier frequency, and the imbalance induced by a molecular absorption influencing only one of the sidebands.*

Depending on the modulation frequency, the FM techniques are divided into three different subgroups, wavelength-modulation spectroscopy (WMS) [4.1,4.2], frequency-modulation spectroscopy (FMS) [4.3-4.6], and two-tone frequency-modulation spectroscopy (TTFMS) [4.7-4.13]. WMS makes use of modulation frequencies much smaller than the halfwidth of the absorption line, FMS uses a modulation frequency comparable to or larger than the halfwidth, while TTFMS for technical convenience uses two modulation frequencies also comparable to or larger than the halfwidth, usually separated by a few MHz.

After a brief description of the different FM techniques, the theory of FM is presented in some detail in Section 4.2.1. The available sensitivity (minimum detectable absorption) in the FM techniques is discussed in conjunction with Section 4.4. However, to introduce the topic an example with a direct absorption measurement and a corresponding one made with FM techniques will be given. Figs. 4.4a and b show water vapour absorption spectra recorded using direct detection of the transmitted intensity and TTFMS, respectively. The figure clearly illustrates the higher sensitivity obtainable with TTFMS.

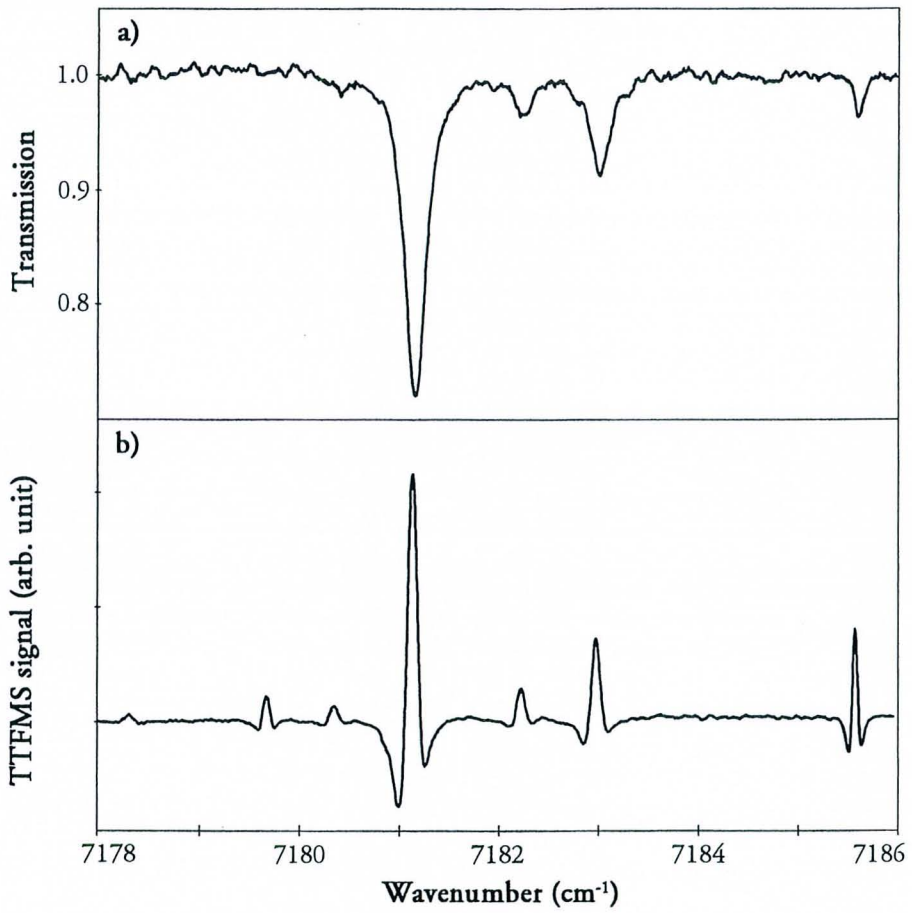

Fig. 4.4 a) *Direct absorption and b) TTFMS spectra of water vapour around 1.39 μm measured over a pathlength of 0.5 m in indoor air (relative humidity ≈ 40 %). The integration time for the two spectra is the same.*

WMS usually employs modulation frequencies in the 1-100 kHz (low-frequency WMS) and sometimes also in the 1-10 MHz (high-frequency WMS) region. Frequency and phase-sensitive detection can be made either at the fundamental frequency ($1f$) or at some harmonic. Most frequent is detection at twice the modulation frequency ($2f$), which produces lineshapes similar to the second-derivative of the original absorption lineshape. The recorded lineshape at $1f$ detection resembles the (first-)derivative of the original lineshape, and this has given rise to the often used name *derivative spectroscopy*. The implementation of low-frequency WMS is relatively simple: the modulation current is superimposed on the laser drive current

directly via the diode laser driver and commercially available lock-in amplifiers are used for detection. This is the reason for the extensive use of this technique.

FMS and TTFMS use much higher modulation frequencies than normally employed in WMS, typically in the radio-frequency region (0.1-3 GHz). In FMS and TTFMS only discrete components in the detection electronics are used (essentially a phase-shifter and a mixer), and a properly designed bias-T is essential to impedance match the sine-wave generator and the diode laser. The reason for applying FMS is two-fold: large modulation frequencies maximise the differential absorption experienced by the sidebands and the laser excess noise (see Section 4.4) is negligible at these frequencies. The study of atmospheric pressure-broadened absorption lines, with halfwidths of the order of 0.05 cm^{-1} (1.5 GHz), requires very large modulation frequencies to achieve optimum sensitivity. Thus, photo-detectors and detection electronics with matching bandwidths are required, which complicates and makes the signal detection expensive. TTFMS circumvents this problem. In TTFMS large modulation frequencies can be applied to maximise the differential absorption experienced by the sidebands. However, detection is performed at a lower beat frequency, typically in the MHz range, allowing the use of relatively inexpensive and low-bandwidth detectors and demodulation circuitry, which constitutes a technical convenience as mentioned above. A further advantage of TTFMS is that the phase-sensitive detection recovers the signal at a frequency that is different from those of the two signal generators. Thus, cross talk into the signal channel can be avoided, eliminating a potential noise source.

For all FM techniques, WMS, FMS as well as TTFMS, the absence of a large and sometimes sloping intensity background in the FM signals is a great advantage. However, the recorded spectrum does not provide any absolute calibration which constitutes a drawback. Owing to this, a separate signal calibration has to be made.

The best reported minimum detectable absorption (normally specified for a signal-to-noise ratio (SNR) of 1 and a detection bandwidth of 1 Hz) in FMS and TTFMS is of the order of 10^{-7} - 10^{-8} [4.14-4.18], whereas values in the range 10^{-5} - 10^{-7} pertain to lower frequencies [4.17,4.19-4.21].

4.2.1 Theory of frequency modulation

The differences between WMS and FMS (TTFMS) are slight, and partly semantic. The notations are somewhat misleading since in both cases it is the optical frequency of the laser that is modulated. WMS and FMS actually represent limiting cases of the same technique. The theoretical description of WMS is usually made in an intensity representation, while the FMS theory uses an electric field approach. The theory adopted for high-frequency modulation has general validity, while the prevalent WMS theory is limited to low modulation frequencies. The difference between WMS and

FMS theory has been elucidated in [4.22]. In this section the basic FMS theory is presented.

The electrical field of an unmodulated diode laser can be expressed as

$$E(t) = E_0 \exp\left[i\varphi(t)\right], \qquad [4.1]$$

where $\varphi(t) = 2\pi\nu t$ and ν is the oscillating frequency.

In FM, ν varies with time and is defined as the momentary frequency ν_i,

$$\nu_i = \frac{1}{2\pi}\frac{d\varphi(t)}{dt}. \qquad [4.2]$$

In FM systems, the momentary frequency varies as

$$\nu_i = \nu_c + \Delta\nu\cos(2\pi\nu_m t), \qquad [4.3]$$

where ν_c is the carrier frequency, ν_m is the modulation frequency, and $\Delta\nu$ is the amplitude of the modulated signal. Eqs. 4.2 and 4.3 yield

$$\varphi(t) = 2\pi\nu_c t + \frac{\Delta\nu}{\nu_m}\sin(2\pi\nu_m t). \qquad [4.4]$$

The FM index β is defined according to

$$\beta = \frac{\Delta\nu}{\nu_m}. \qquad [4.5]$$

Thus, the FM index relates the maximum frequency deviation to the modulation frequency.

The electric field of a modulated diode laser then becomes

$$E(t) = E_0 \exp\left[i2\pi\nu_c t + i\beta\sin(2\pi\nu_m t)\right]. \qquad [4.6]$$

Since the emission power of a diode laser depends on the operating current, simultaneous amplitude modulation (AM) of the frequency modulated electric field also occurs such that

$$E(t) = E_0\left[1 + M\sin(2\pi\nu_m t + \psi)\right]\exp\left[i2\pi\nu_c t + i\beta\sin(2\pi\nu_m t)\right], \qquad [4.7]$$

where M is the AM index and ψ is the phase difference between AM and FM. By expanding the AM term using Eulerian formulae we obtain

$$\sin(2\pi\nu_m t + \psi) = \frac{\exp(i2\pi\nu_m t + i\psi) - \exp(-i2\pi\nu_m t - i\psi)}{2i} \qquad [4.8]$$

and by replacing the exponential frequency term as a summation over Bessel functions according to

$$\exp\left[i\beta\sin(2\pi\nu_m t)\right] = \sum_{p=-\infty}^{\infty} J_p(\beta)\exp(i2\pi p\nu_m t), \qquad [4.9]$$

eq. 4.7 becomes

$$E(t) = E_0\sum_{p=-\infty}^{\infty} r_p(\beta, M, \psi)\exp\left[i2\pi(\nu_c + p\nu_m)t\right], \qquad [4.10]$$

where r_p is defined as

$$r_p(\beta, M, \psi) \equiv J_p(\beta) + \frac{M}{2i}\left[\exp(i\psi)J_{p-1}(\beta) - \exp(-i\psi)J_{p+1}(\beta)\right]. \qquad [4.11]$$

The electric field (spectral distribution of the frequency components) of the FM modulated laser field is described by Eq. 4.10. Pure frequency modulation (M = 0) leads to sideband coefficients $r_p = J_p(\beta)$ and a 180° phase shift for upper and lower sidebands with odd p, as illustrated in Fig. 4.3 (middle part) for the case of a low modulation index β. In the general case the intensities in the upper and lower sidebands with equal p differ in magnitude due to superposition of AM and FM signals. This asymmetry leads to RAM-induced noise (see Section 4.4).

The interaction of an electrical field at frequency ν with an absorber can be characterised by a complex transmission function defined as

$$T(\nu) = \exp\left[-\delta(\nu) - i\phi(\nu)\right]. \qquad [4.12]$$

The electric field attenuation $\delta(\nu)$ is related to the intensity absorption coefficient (defined in Chapter 3) as $\delta(\nu)=\alpha(\nu)L/2 = \sigma(\nu)NL/2$, and the electric field dispersion

$\phi(\nu)$ (the optical phase shift) is given by $\phi(\nu)=n(\nu)L\nu/c$, where $n(\nu)$ is the frequency dependent index of refraction.

The complex transmission function interacts with the individual frequency components $\nu_c+p\nu_m$ in the modulated beam. The electric field after interaction with the absorber is

$$E(t) = E_0 \sum_{p=-\infty}^{\infty} T(\nu_c + p\nu_m) r_p(\beta, M, \psi) \exp\left[i2\pi(\nu_c + p\nu_n)\right] \qquad [4.13a]$$

or

$$E(t) = E_0 \sum_{p=-\infty}^{\infty} r_p(\beta, M, \psi) \exp\left[i2\pi(\nu_c + p\nu_m)t - \delta(\nu_c + p\nu_m) - i\phi(\nu_c + p\nu_m)\right]. \qquad [4.13b]$$

Experiments measure the intensity which is proportional to the square of the electric field. The transmitted intensity is given by

$$I(t) = \frac{c\,\varepsilon_0}{2}\left|E(t)\right|^2$$

$$= \frac{c\,\varepsilon_0}{2} E_0^2 \sum_{p,p'}^{\infty} r_p r_{p'}^* \exp\left[i2\pi(p - p')\nu_m t\right]$$

$$\exp\left[-\delta(\nu_c + p\nu_m) - \delta(\nu_c + p'\nu_m) - i\phi(\nu_c + p\nu_m) + i\phi(\nu_c + p'\nu_m)\right], \quad [4.14]$$

where r^* is the complex conjugate of r. The detector photocurrent is analysed at ν_m or at some harmonic $\Lambda = n\nu_m$ (n=1,2,3,...). The resulting signal is obtained by setting p-p' = $\pm n$ in Eq. 4.14:

$$I_\Lambda(t) = \frac{c\,\varepsilon_0}{2} E_0^2 \exp(i2\pi\Lambda t) \sum_{p=-\infty}^{\infty} r_p r_{p-n}^* \exp\left[-\delta(\nu_c + p\nu_m) - \delta(\nu_c + (p-n)\nu_m)\right.$$

$$\left. - \phi(\nu_c + p\nu_m) + \phi(\nu_c + (p-n)\nu_m)\right] + c.c. \qquad [4.15]$$

It is convenient to re-write this equation as

$$I_\Lambda(t) = \frac{c\,\varepsilon_0}{2} E_0^2 \left[Z \exp(i2\pi\Lambda t) + Z^* \exp(-i2\pi\Lambda t)\right], \qquad [4.16]$$

where

$$Z = \sum_{p=-\infty}^{\infty} r_p r_{p-n}^{*} \exp\left[-\delta(\nu_c + p\nu_m) - \delta(\nu_c + (p-n)\nu_m)\right]$$

$$\exp\left[-i\phi(\nu_c + p\nu_m) + i\phi(\nu_c + (p-n)\nu_m)\right]. \qquad [4.17]$$

It follows from this that

$$I_{\Lambda}(t) = \frac{c\,\varepsilon_0}{2} E_0^2 \left[2\mathrm{Re}(Z)\cos(2\pi\Lambda t) - 2\mathrm{Im}(Z)\sin(2\pi\Lambda t)\right]. \qquad [4.18]$$

By selecting the detection system phase angle, the signal can be detected as the pure real or the pure imaginary part of Z (corresponding to pure absorption or pure dispersion), or as a mixture.

In a similar way, the slightly more complicated TTFMS can be mathematically described. The key feature of this description is that the signal retrieved at the low-difference frequency of the two primary modulations is directly related to the full high-frequency differential absorption (Cf. optical heterodyne detection).

4.3 Fast scan integration

Most diode laser absorption measurements include fast scanning of the diode laser across the absorption profile at around 100 Hz, and the accumulation of multiple spectra. This enables a high signal-to-noise ratio (SNR) by the integration of the signal, and systematic drifts are effectively eliminated. The technique is frequently used in direct absorption measurements and then much resembles the slotted-disc scanning used in DOAS (differential optical absorption spectroscopy) measurements employing classical light sources [4.23]. However, fast scan integration is also combined with WMS, TTFMS and TTFMS. The method, also referred to as sweep integration [4.24,4.25], effectively reduces the influence from low frequency (1/f) noise in the recorded spectra. A detection sensitivity as good as 10^{-5}-10^{-6} can be obtained even in direct absorption measurements.

4.4 Noise and sensitivity

Noise is all unwanted signal that appears at the detection side. Noise has different origins:

- *Thermal noise* originates from the random fluctuations of charge carriers. It does not depend on the incident power and has a white noise spectrum, i.e. it is independent of the frequency.

- *Laser excess noise (flicker (1/f) noise).* This source of noise is the main motivation for adopting a modulation scheme. It is due to the effect of intrinsic laser properties and to external noise sources. External noise sources are injection-current noise, temperature instabilities and optical feedback, and intrinsic noise sources are photon and carrier density fluctuations, index of refraction fluctuations and partition noise. The noise spectrum has an $1/f$ dependence.

- *Shot noise* originates from the quantum nature of light. It depends on the incident flux of photons (incident power). The quantum noise, like the thermal noise, is independent of frequency.

- *RAM-induced noise.* FM is always accompanied by residual amplitude modulation and introduces a non-zero background in the recorded spectra. The measurements in Paper III were essentially limited by this type of noise.

- *Interference fringes* constitute an annoying source of noise, which is further discussed below.

Several published papers compare the sensitivity of the different frequency modulation techniques [4.17,4.19-4.21]. The results are not entirely consistent. It seems like the sensitivity reported for a particular modulation scheme is closely related to the laser employed and the experimental arrangement used. Thus, general statements about superiority of a specific modulation technique are difficult to make.

Summarising, one can say that any of the high-frequency WMS, FMS and TTFMS techniques can in principle achieve shot-noise limited detection, corresponding to a minimum detectable absorption of the order of 10^{-7} or better. However, the minimum detectable absorption is in practice often set to 10^{-6} by the presence of interference fringes. These originate from spurious reflections between parallel optical surface in the laser beam path. These accidental interference fringes manifest themselves as an oscillating intensity background. If the fringe widths are comparable to the linewidth of the absorbing species under investigation, they can easily obscure the detection of

weak absorptions. Fringes can be reduced by careful angling of all transmissive optics, and by the use of reflective optics, wedged windows and beamsplitters. A large variety of methods to reduce the effect of interference fringes has been proposed, e.g., dithering of optical components [4.26-4.28] or filtering techniques [4.14,4.29-4.31].

Noise aspects and detection limits in FM are discussed in detail in Paper III and in Refs. [4.4,4.10,4.20,4.21,4.32,4.33].

5. Nonlinear optical frequency conversion

Nonlinear optical frequency conversion refers to the generation of new frequency components by mixing laser light of different frequencies in nonlinear media. Utilising nonlinear optical frequency conversion, coherent radiation can be generated in wavelength regions where no convenient laser sources are available. Thus, for room-temperature operated diode lasers, which, as described in Chapter 2, emit light in the wavelength region between 400 nm and 2 μm, nonlinear optical frequency conversion is a practical way of producing tuneable radiation at ultraviolet and infrared wavelengths. Nonlinear optical frequency conversion comprises a large variety of different nonlinear optical processes, and a comprehensive description of such processes can be found in textbooks in the field of nonlinear optics [5.1,5.2]. Here only a brief survey of techniques related to the present work will be given.

5.1 Frequency mixing

Typically, only laser light is intense enough to induce a nonlinear optical response in a material system and, in fact, the first observation of a nonlinear response was made in 1961, shortly after the demonstration of the first laser. Second-harmonic generation (at 347.15 nm) was observed by shining a ruby laser beam (at 694.3 nm) through a sample of crystalline quartz [5.3]. When light of sufficiently strong intensity propagates through a nonlinear optical medium, the response of the medium can be expressed as

$$P(t) = \varepsilon_0(\chi^{(1)}E(t) + \chi^{(2)}E^2(t) + \chi^{(3)}E^3(t)+\ldots), \qquad [5.1]$$

where E is the applied optical field, P is the polarisation of the medium, ε_o is the permittivity of free space, $\chi^{(1)}$ denotes the linear susceptibility, and $\chi^{(2)}$, $\chi^{(3)}$, ... are the nonlinear optical susceptibilities. The first term in Eq. 5.1, the linear polarisation, is responsible for ordinary optical phenomena such as reflection and absorption, and the third term, the third-order nonlinear polarisation, gives rise to third-harmonic generation and related mixing phenomena, the Kerr effect and the stimulated Raman effect. The second term, the second-order nonlinear polarisation, gives rise to difference-frequency, sum-frequency, and second-harmonic generation, which are the phenomena to be discussed in this chapter. Using symmetry arguments it can be shown that the second-order susceptibility $\chi^{(2)}$ vanishes in media with a centre of

symmetry. The phenomena of interest can thus only be observed in non-centrosymmetrical crystals.

In a simplified form, the generation of new frequency components through the second-order nonlinear polarisation can be described as follows. If an electromagnetic optical field $E(t)$, consisting of two distinct frequencies ω_1 and ω_2, represented in the form

$$E(t) = E_1 \exp(i\omega_1 t) + E_2 \exp(i\omega_2 t) + c.c. \qquad [5.2]$$

is applied to a medium with a non-vanishing second-order susceptibility, the second-order nonlinear polarisation created in the medium will be given by

$$P^{(2)}(t) = \varepsilon_0 \chi^{(2)} \Big[E_1^2 \exp(i2\omega_1 t) + E_2^2 \exp(i2\omega_2 t) + 2E_1 E_2 \exp(i(\omega_1 + \omega_2)t) +$$

$$2E_1 E_2 \exp(i(\omega_1 - \omega_2)t) + c.c. \Big] + 2\varepsilon_0 \chi^{(2)} \Big[E_1 E_1^* + E_2 E_2^* \Big]. \qquad [5.3]$$

As seen from this expression, apart from a dc optical rectification component, four new frequency components in the nonlinear polarisation are generated; the doubled frequencies (second harmonics) $2\omega_1$ and $2\omega_2$, the sum frequency $\omega_1+\omega_2$ and the difference frequency $\omega_1-\omega_2$. These new frequency components of the nonlinear polarisation will, according to the Maxwell equations, act as driving terms for the generation of new frequency components also in the electromagnetic field. Although Eq. 5.3 indicates that four different frequency components can be present in the radiation generated by the nonlinear interaction process, typically only at most one of the frequency components will have any appreciable intensity. The reason for this is that efficient generation of new frequency components requires that certain phase-matching conditions between the interacting waves are fulfilled and these conditions can usually only be achieved for one of the processes at a time.

More generally, difference-frequency, sum-frequency and second-harmonic generation basically involves the interactions between three different light waves, with frequencies ω_1, ω_2 and ω_3. The three waves are sometimes referred to as the idler, the signal and the pump wave, respectively. By convention, $\omega_3 > \omega_2$ and $\omega_2 \geq \omega_1$. The three frequencies are constrained by the energy conservation

$$\omega_3 = \omega_2 + \omega_1 . \qquad [5.4]$$

This equation is a convenient way of expressing the mutual interaction between the three light waves, and allows difference-frequency, second-harmonic and sum-

frequency generation to be described by the same expression. The interaction processes (abbreviated DFG, SFG and SHG, respectively) are thus characterised by

$$\begin{aligned} \omega_2 &= \omega_3 - \omega_1 \quad \text{or} \quad \omega_1 = \omega_3 - \omega_2 \quad \text{(DFG)} \\ \omega_3 &= \omega_2 + \omega_1 \quad \text{(SFG)} \\ \omega_3 &= 2\omega_1 \quad \text{or} \quad \omega_3 = 2\omega_2 \quad \text{(SHG)} \end{aligned} \qquad [5.5]$$

It is important to notice that, using this formalism as opposed to the form in Eq. 5.3, the input frequencies are not always given by ω_2 and ω_1, and the output frequency by ω_3, i.e. for difference-frequency generation, the indices are interchanged. This formalism is used in the following presentation.

Difference-frequency generation is frequently used for conversion of short-wave radiation (e.g., visible and near-infrared radiation) to long-wave radiation (e.g., infrared radiation). On the other hand, to convert long-wave radiation to the short wavelength region, sum-frequency generation is used. Second-harmonic generation is a special case of sum-frequency generation ($\omega_1 = \omega_2$) and is typically employed to convert the radiation from lasers in the near-infrared and visible to the visible and ultraviolet spectral regions. One well-known example is the second-harmonic generation at 532 nm of the 1064 nm Nd:YAG laser output. In the present work sum-frequency generation to 254 nm for mercury detection has been achieved by combining two diode lasers emitting at 404 nm and 684 nm, respectively, in a BBO (β-BaB_2O_4) crystal (Paper V). Difference-frequency generation in periodically poled lithium niobate ($LiNbO_3$) to 3.4 μm for methane detection has also been achieved using a 760 nm and a 980 nm diode laser (Paper VI).

5.2 Phase-matching

In frequency mixing one is concerned with efficient generation of electromagnetic radiation at the difference, sum or second-harmonic frequencies of the applied electromagnetic fields. A crucial issue in this context is the phase-matching between the interacting waves. Due to dispersion, waves oscillating at different frequencies normally propagate with different phase velocities in a nonlinear medium. The relative phase between the interacting waves will then vary along the nonlinear medium, and since the direction of power flow is determined by the phase difference between the waves, there will be a periodic transfer of power between the waves along the length of the nonlinear medium. For efficient generation of the difference, sum or second-harmonic frequencies it is therefore essential to phase-match the interaction so that the intensity of the newly generated wave continuously increases at the expense of the intensity of the applied radiation throughout the whole length of the nonlinear medium. Phase-matching between the interacting waves can be accomplished by *birefringent phase-matching*, which uses the birefringence displayed by many crystals

[5.4-5.6], or by *quasi phase-matching*, in which a periodic structure is built into the nonlinear medium so that the relative phase is corrected in regular intervals [5.7,5.8].

5.2.1 Birefringent phase-matching

Birefringent phase-matching makes use of, as the name implies, the birefringence displayed by uniaxial and biaxial crystals. Birefringence is the dependence of the refractive index on the propagation and polarisation direction of the electromagnetic radiation, and since the refractive index determines the phase velocity of a propagating wave, phase-matching can be achieved by proper orientation of the nonlinear crystal and the polarisation of the input radiation.

The phase mismatch, $\Delta\boldsymbol{k}$, in difference frequency ($\omega_2=\omega_3-\omega_1$), sum-frequency ($\omega_3=\omega_2+\omega_1$) and second-harmonic generation ($\omega_3=2\omega_1$), respectively, is given by

$$\begin{aligned} \Delta\boldsymbol{k} &= \boldsymbol{k}_3 - \boldsymbol{k}_1 - \boldsymbol{k}_2 && \text{(DFG)} \\ \Delta\boldsymbol{k} &= \boldsymbol{k}_1 + \boldsymbol{k}_2 - \boldsymbol{k}_3 && \text{(SFG)} \\ \Delta\boldsymbol{k} &= 2\boldsymbol{k}_1 - \boldsymbol{k}_3 , && \text{(SHG)} \end{aligned} \qquad [5.6]$$

where $\boldsymbol{k}_i$ is the wave vector

$$|\boldsymbol{k}_i| = k_i = \frac{n_i \omega_i}{c} \qquad [5.7]$$

corresponding to the wave with frequency ω_i. $n_i=n(\omega_i)$ is the refractive index, and c is the speed of light. Phase-matching is achieved whenever

$$\Delta\boldsymbol{k} = 0 . \qquad [5.8]$$

Phase-matching can be accomplished using either scalar (collinear) phase-matching or vector (noncollinear) phase-matching. Scalar phase-matching is experimentally the most convenient method. Only scalar phase-matching has been used in the present work, and the following description will focus on this phase-matching method. Using collinear beams, the phase-matching condition for difference-frequency and sum-frequency generation is

$$k_3 = k_1 + k_2 \qquad \text{or} \qquad n_3\omega_3 = n_1\omega_1 + n_2\omega_2 \qquad [5.9]$$

and for second-harmonic generation ($\omega_1 = \omega_2$ and $\omega_3 = 2\omega_1$)

$$k_3 = 2k_1 \qquad \text{or} \qquad n_3 = n_1 . \qquad [5.10]$$

It can be seen from these expressions that the phase-matching condition can never be fulfilled if the interacting waves have the same polarisation because of normal dispersion: the refractive index is an increasing function of frequency. Mixing waves of different polarisation in uniaxial or biaxial crystals displaying birefringence is the only possible way of fulfilling the phase-matching condition.

Uniaxial crystals are characterised by one optical axis while biaxial crystals have two optical axes. The phase-matching considerations for uniaxial crystals are more straight-forward than for biaxial crystals, and since biaxial crystals have not been used in the present work, only uniaxial crystals will be considered in the following. In uniaxial crystals, a light wave polarised perpendicular to the plane containing the optical axis and the propagation vector $\boldsymbol{k}$ of the wave is called an *ordinary wave*, while a wave polarised in the plane is called an *extraordinary wave*. The refractive indices in the two orthogonal directions are called the ordinary n_o and the extraordinary n_e refractive indices, respectively, and it is the difference in refractive index between the ordinary and the extraordinary wave that is called birefringence. Uniaxial crystals are referred to as either negative or positive; in a positive uniaxial crystal, the extraordinary refractive index n_e is larger than the ordinary index n_o, while the opposite is true for negative uniaxial crystals. The refractive index of the ordinary wave does not depend on the propagation direction, while the refractive index of the extraordinary wave depends on the angle θ between the optics axis and the propagation vector $\boldsymbol{k}$ according to

$$\frac{1}{n_e(\theta)^2} = \frac{\sin^2\theta}{n_e^2} + \frac{\cos^2\theta}{n_o^2}, \qquad [5.11]$$

where it can be noted that $n_e(90°) = n_e$ and $n_e(0°) = n_o$. Expressions (the so called Sellmeier equations) for the ordinary and extraordinary refractive indices as a function of frequency, and for some crystals also of temperature, for different nonlinear crystals can be found with varying accuracy in the literature. A comprehensive description of the properties of a large variety of different nonlinear optical crystals has been given in [5.9].

For uniaxial crystals, two phase-matching methods, Type I and II, can be distinguished. The two methods are summarised in Table 5.1. Common for both methods is that the wave with the highest frequency (ω_3) is polarised in the direction with the lower of the two possible refractive indices. There are two possibilities for the two lower frequency waves (ω_1 and ω_2); Type I phase-matching is when both waves have the same polarisation and Type II phase-matching is when the waves have orthogonal polarisations.

Table 5.1 *Phase-matching methods for uniaxial crystals.*

	Positive uniaxial crystal ($n_e > n_o$)	Negative uniaxial crystal ($n_e < n_o$)
Type I	$n_3^o\omega_3 = n_1^e\omega_1 + n_2^e\omega_2$	$n_3^e\omega_3 = n_1^o\omega_1 + n_2^o\omega_2$
Type II	$n_3^o\omega_3 = n_1^o\omega_1 + n_2^e\omega_2$	$n_3^e\omega_3 = n_1^e\omega_1 + n_2^o\omega_2$

Birefringent phase-matching is achieved by adjusting the angle θ for a certain three-wave interaction in a particular crystal. The phase-matching angle for a three-wave interaction in the crystal is calculated using Eq. 5.11 and the appropriate expression in Table 5.1.

As an example of phase-matching, we can consider the sum-frequency generation in Paper V, where a wavelength of 254 nm (ω_3) was generated by mixing 404 nm (ω_2) and 684 nm (ω_1) in a BBO crystal. BBO is a negative uniaxial crystal, and Type I phase-matching was chosen. Fig. 5.1 is a schematic illustration of the phase-matching between the three waves. The phase-matching conditions for Type I phase-matching in a negative uniaxial crystal then becomes

$$\frac{1}{(n_1^o\omega_1 + n_2^o\omega_2)^2} = \frac{\sin^2\theta}{(n_3^e\omega_3)^2} + \frac{\cos^2\theta}{(n_3^o\omega_3)^2}. \qquad [5.12]$$

By replacing $\cos^2\theta$ by $1-\sin^2\theta$ and simplifying, the resulting expression becomes

$$\sin^2\theta = \frac{\dfrac{1}{(n_1^o\omega_1 + n_2^o\omega_2)^2} - \dfrac{1}{(n_3^o\omega_3)^2}}{\dfrac{1}{(n_3^e\omega_3)^2} - \dfrac{1}{(n_3^o\omega_3)^2}}. \qquad [5.13]$$

Thus, using the expressions for the ordinary and the extraordinary refractive indices, the orientation (θ) of the crystal can be calculated, so that efficient generation at 254 nm can be achieved. For our experimental arrangement configuration a value of θ = 48° was determined. In the experiments the crystal was slowly rotated until phase-matching was observed, basically at the expected angle.

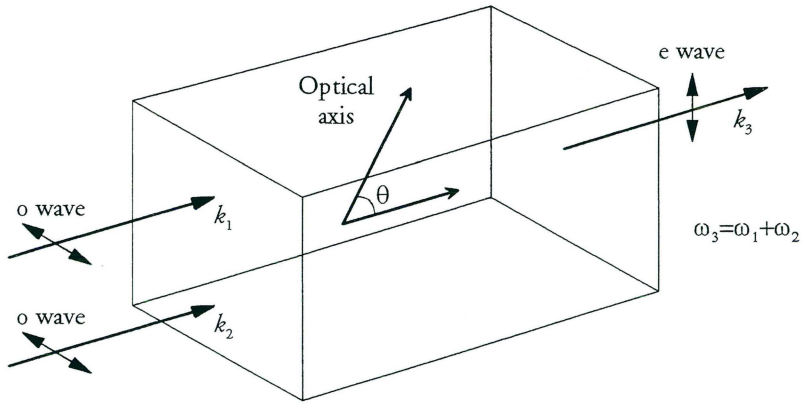

Fig. 5.1 *Arrangement of three beams and crystal orientation in sum-frequency generation for Type I phase-matching in a negative uniaxial crystal.*

A serious drawback of birefringent phase-matching is that the direction of propagation for an extraordinary wave generally does not coincide with that of the ordinary one. Whenever the phase-matching angle θ is not equal to 0° or 90°, a detrimental beam *walk-off* for the extraordinary wave occurs. The beam walk-off angle can be calculated according to [5.9]

$$\rho(\theta) = \pm \arctan\left(\left(\frac{n_0}{n_e}\right)^2 \tan(\theta)\right) \mp \theta \,. \qquad [5.14]$$

Here the upper signs pertain to negative and the lower sign to positive crystals. Beam walk-off can to some extent be compensated by vector (noncollinear) phase-matching. Temperature tuning is also possible for some crystals, so that phase-matching can be achieved with a phase-matching angle of 0° or 90°. The phase-matching is then often referred to as *non-critical*, while *critical phase-matching* otherwise pertains.

5.2.2 Quasi phase-matching

In quasi phase-matching (QPM), the waves propagate with different phase velocities, but as the direction of the power flow reverses, when the relative phase difference (the phase mismatch) has grown, the sign of the nonlinear susceptibility is also reversed so that the phase difference is "reset" and the power continues to flow monotically from the applied radiation to the generated radiation at the difference, sum or second-harmonic frequencies. A sign reversal of the nonlinearity can be obtained in ferroelectrics, such as $LiNbO_3$, $LiTaO_3$, and KTP, by a reversal of the domain

orientation. A description of the manufacturing process, typically involving lithography and electric field poling, can be found in, e.g., [5.10].

The important parameter in the quasi phase-matching scheme is the coherence length, L_c, the distance over which the relative phase difference changes by π. The coherence length is given by

$$\Delta k \cdot \pi = L_c, \qquad [5.15]$$

where Δk is the (scalar) phase mismatch according to Eq. 5.6. In analogy with the situation for birefringent phase-matching, the phase mismatch in quasi phase-matching is given by

$$\Delta k_{QPM} = \Delta k - \frac{2\pi}{\Lambda}, \qquad [5.16]$$

where Λ is the quasi phase-matching period. When the period is equal to twice the coherence length, the phase mismatch is zero and the efficiency of the process is maximised. Typical periods, Λ, for quasi phase-matching in $LiNbO_3$ (the crystal used in Paper VI), are of the order of 15 μm to 25 μm for difference-frequency generation and 5 μm to 15 μm for second-harmonic and sum-frequency generation. Quasi phase-matching typically involves temperature tuning, and the required period for a certain three-wave interaction is calculated using the same Sellmeier equations as for birefringent phase-matching. Fig. 5.2 illustrates perfect phase-matching (non-critical birefringent phase-matching), quasi phase-matching and no phase-matching.

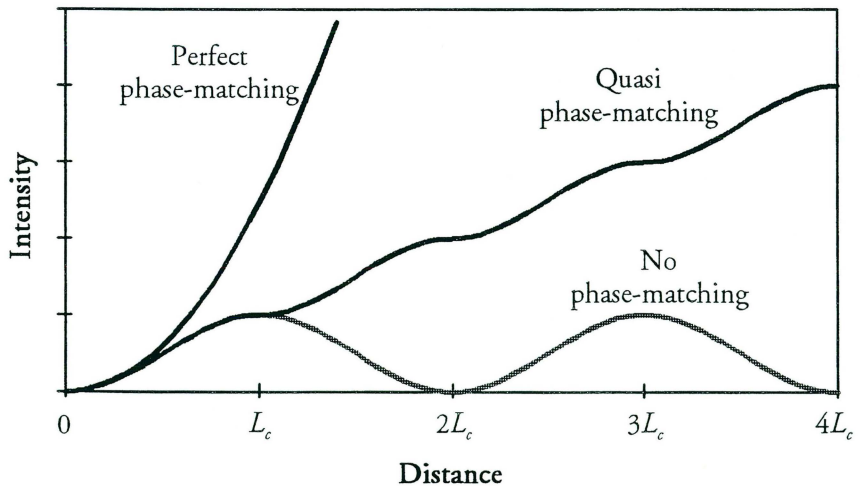

Fig. 5.2 *Illustration of three levels of phase-matching.*

A typical geometry of quasi phase-matching is shown in Fig. 5.3. This particular example shows difference-frequency generation as performed in Paper VI. It could be noted that all the waves have the same polarisation, allowing the largest coefficient in the nonlinear susceptibility tensor, fully describing the crystal, to be exploited. Since the quasi phase-matching technique does not rely on birefringence, the only fundamental limit is set by the transparency range of the material. Details about quasi phase-matching have been given in, e.g., [5.8,5.10]. Popular accounts can be found in [5.11,5.12].

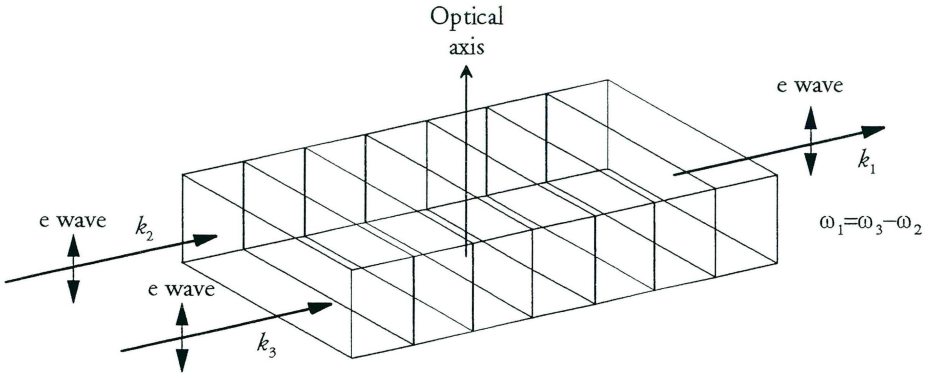

Fig. 5.3 *Quasi phase-matching in difference-frequency generation.*

5.3 Conversion efficiency

The conversion efficiency depends on the phase-matching, the nonlinear properties and the length of the crystal, the input powers, and a focusing factor. The general expressions governing the conversion efficiency for sum- and difference-frequency generation are given and discussed in Papers V and VI, respectively [5.13,5.14]. An important aspect that has not been discussed so far is the optimal focusing, which also can be theoretically predicted. Beam overlap is also essential. In this context, the possibility of rectification of the diode laser asymmetric beams through the use of anamorphic prism pairs (Fig. 2.2) is also valuable.

6. Applications in energy, environmental and medical research

6.1 Introduction

Laser spectroscopy provides powerful means for real-time analysis and diagnostics in many important application fields, such as energy, environmental and medical research. Many proof-of-principle experiments have been performed with complex and expensive equipment. Clearly, diode lasers have a particularly great attraction for applications because of the realistic costs and ease of operation, that frequently characterise these sources. In the present section the implications of the present work in the fields of combustion research, environmental monitoring and medical diagnostics are discussed. A brief perspective to the extensive research activities being pursued in these areas is also given.

Absorption is one of the modes of interaction between light and matter. Actually, in the present work mostly absorption, but also fluorescence and scattering have been used. In Chapter 2 issues regarding absorption were treated in detail. In this section, aspects of fluorescence as well as scattering will also be briefly considered with reference to Fig. 6.1.

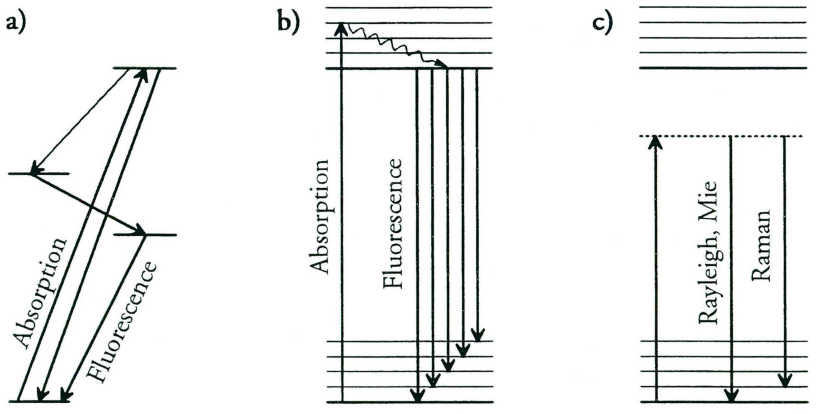

Fig. 6.1 *Schematic illustration of the interaction processes in atoms and molecules. a) and b) Resonant transitions in atoms and molecules, respectively. c) Non-resonant scattering processes.*

Following absorption of an incoming photon, the atom or molecule is excited to an upper level. Excited state lifetimes for unperturbed atoms are of the order of μs to ns. In the subsequent decay, resonance radiation back to the ground state or fluorescence (at longer wavelengths) occurs. Such radiation is detected for potassium atoms in Paper II. At atmospheric pressure or in solids or liquids the lifetime of the excited state is strongly reduced due to collisionless transitions, which also reduce the fluorescence yield. For molecules in solids and liquids, a very fast radiationless relaxation down to the lowest vibrational level of the excited state occurs. The subsequent fluorescence decay follows in a broad spectral distribution, which is related to the broadened ground state sublevel distribution. Since the upper-state relaxation occurs, the fluorescence spectral shape is largely independent of the exact excitation wavelength. Since the upper state structure is also smeared out, no demands on a very sharp or specific wavelength for the exciting light exist. In Paper VII, violet diode laser radiation was used to induce characteristic fluorescence (laser-induced fluorescence, LIF) in leaves of different degrees of senescence and in human malignantly transformed tissue.

Even if the incoming laser radiation is not resonant with an energy separation in the molecules under study, a weak interaction process can occur: elastic or inelastic scattering. Elastic scattering (Rayleigh scattering) does not involve any energy change for the outgoing radiation, whereas a shift, corresponding to vibrational or rotational splittings occurs in inelastic (Raman) scattering. The Raman shift is characteristic for the molecules under study. If elastic scattering against spherical macroscopic particles of extension much larger than the wavelength occurs, the process is referred to as Mie scattering [6.1,6.2]. Extensions of the theory can also handle non-spherical particles. Particle scattering is the subject of the work presented in Paper I.

6.2 Combustion diagnostics

Combustion remains the most important mode of energy conversion [6.3,6.4]. Measurements of combustion parameters, such as temperature, pressure, velocity and concentration are important in fluid flow, combustion and heat transfer research, and non-intrusive, laser-based techniques facilitate experimental studies considerably [6.5]. Among the diagnostic techniques for combustion zones, Mie and Raman scattering, laser-induced fluorescence, coherent anti-Stokes Raman scattering and degenerate four-wave mixing can be mentioned. Spatially resolved measurements can conveniently be performed by planar imaging using laser-induced fluorescence [6.6-6.11]. The technique is ideally suited for studies of transient phenomena and detection of minor species, due to the high sensitivity combined with a high spectral and temporal resolution. However, due to quenching, quantitative concentration measurements are difficult to perform.

Absorption spectroscopy using diode lasers has the advantage of providing fast, simple and sensitive quantitative measurements of combustion parameters. The most readily available parameter is concentration, but, as outlined in Chapter 3, the lineshape of an absorption line is strongly dependent on the environmental conditions under which it was recorded. Thus, important information regarding combustion can be inferred from the lineshape variations under varying environmental conditions. Diode laser absorption spectroscopy has been widely employed for the determination of concentration, temperature, pressure and velocity [6.12-6.21].

On the other hand, absorption measurements do not provide spatial information because of the line-of-sight integrating nature of the techniques. The detected absorption signal integrates the incremental absorptions from each of the spatial locations along the beam path from the laser to the detector. Combining multi-angular absorption spectroscopy with tomographic reconstruction techniques, spatially resolved measurements (2D) can be achieved [6.22-6.29]. In Paper VI simultaneous absorption measurements of methane, oxygen and water vapour, all of interest in combustion, are illustrated.

As an illustration of temperature and concentration measurements, which extends previous work in this laboratory [6.27], absorption measurements of molecular oxygen in a lean pre-mixed methane-oxygen flame (equivalence ratio 0.81) employing two-tone frequency-modulation spectroscopy (TTFMS) for increased sensitivity have been performed. The experimental set-up is schematically illustrated in Fig. 6.2 and results of the measurements are shown in Fig. 6.3. Descriptions of the TTFMS measurement scheme have been given in Paper III and in [6.27]. The wavelength of the diode laser was repetitively tuned by applying a jump scanning technique, which made it possible to measure several molecular oxygen lines at the same time. A dual-beam subtraction scheme was employed to effectively cancel the absorption signal from the ambient oxygen in the beam path outside the flame region. The burner, with a 4 × 18 mm rectangular nozzle, was constructed to give a laminar flow of pre-mixed methane and oxygen. Line-of-sight absorption measurements of molecular oxygen were performed 3 mm above the nozzle orifice by translating the nozzle along two directions 90° apart, the parallel and perpendicular direction, as illustrated in Fig. 6.3C. An algebraic reconstruction technique [6.27,6.30] can be employed for the reconstruction of the oxygen concentration and the flame temperature from data of this kind, but within the scope of the present work the somewhat elaborate task of a tomographic back-projection of the data has not been performed. Still, the major aspects of multi-angular measurements for spatially resolved measurements are illustrated in Fig. 6.3.

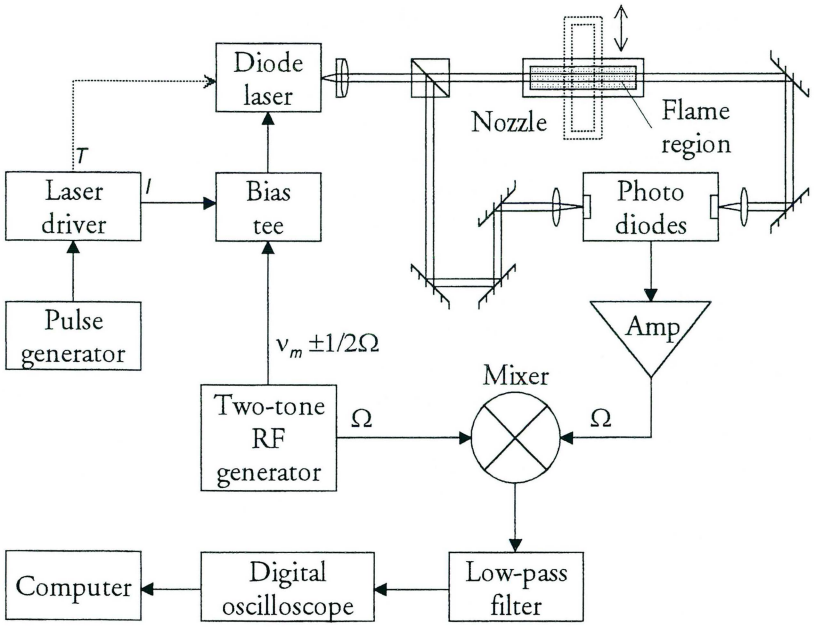

Fig. 6.2 *Experimental arrangement for sensitive detection of molecular oxygen in a methane-oxygen flame.*

The absorption measurements were performed on the R15Q16, R17R17, R23Q24 and R33Q34 lines in the oxygen A band at 760.094 nm, 760.074 nm, 759.660 nm and 759.636 nm, respectively. Examples of spectral recordings in the parallel direction are shown in Fig. 6.3A. The sharp peaks in the middle of the spectra display the arrival of the second current jump. Fig. 6.3B and D show the peak values of the TTFMS signals along the parallel and perpendicular directions. The spatial positions of the spectral recordings in Fig. 6.3A (a-d) are indicated in Fig. 6.3B. The energy (E'') of the lower state of the transitions are 344 cm^{-1} (R15Q16), 440 cm^{-1} (R17R17), 791 cm^{-1} (R23Q24) and 1605 cm^{-1} (R33Q34) [3.1]. Since the Boltzmann population factor is contained within the line strength S (see Eq. 3.14), it is clear that the intensity of the R33Q34 line is strongly dependent on the temperature in the flame and that the R15Q16 and R17R17 lines are more related to the concentration. The R23Q24 line is related both to the temperature and the concentration. Thus, by comparing the relative magnitudes of the TTFMS signals in Fig. 6.3B and D, information regarding both temperature and concentration in the flame can be obtained. E.g., according to Fig. 6.3B, the peak values of the R15Q16 (and R17R17) line are almost the same in the middle of the flame (position 0 mm) and far from the flame (position 18 mm), indicating approximately equal oxygen concentrations. One can also see that the temperature is high at the rim of the flame region (the luminous zone, position 2 mm), where the R33Q34 line peaks. This is where most of the

reactions takes place, and consequently, the concentration is also lower than in, e.g., the middle of the flame. However, the lowest concentration is found just outside the rim of the flame region (position 3 mm), where most of the ambient oxygen is consumed.

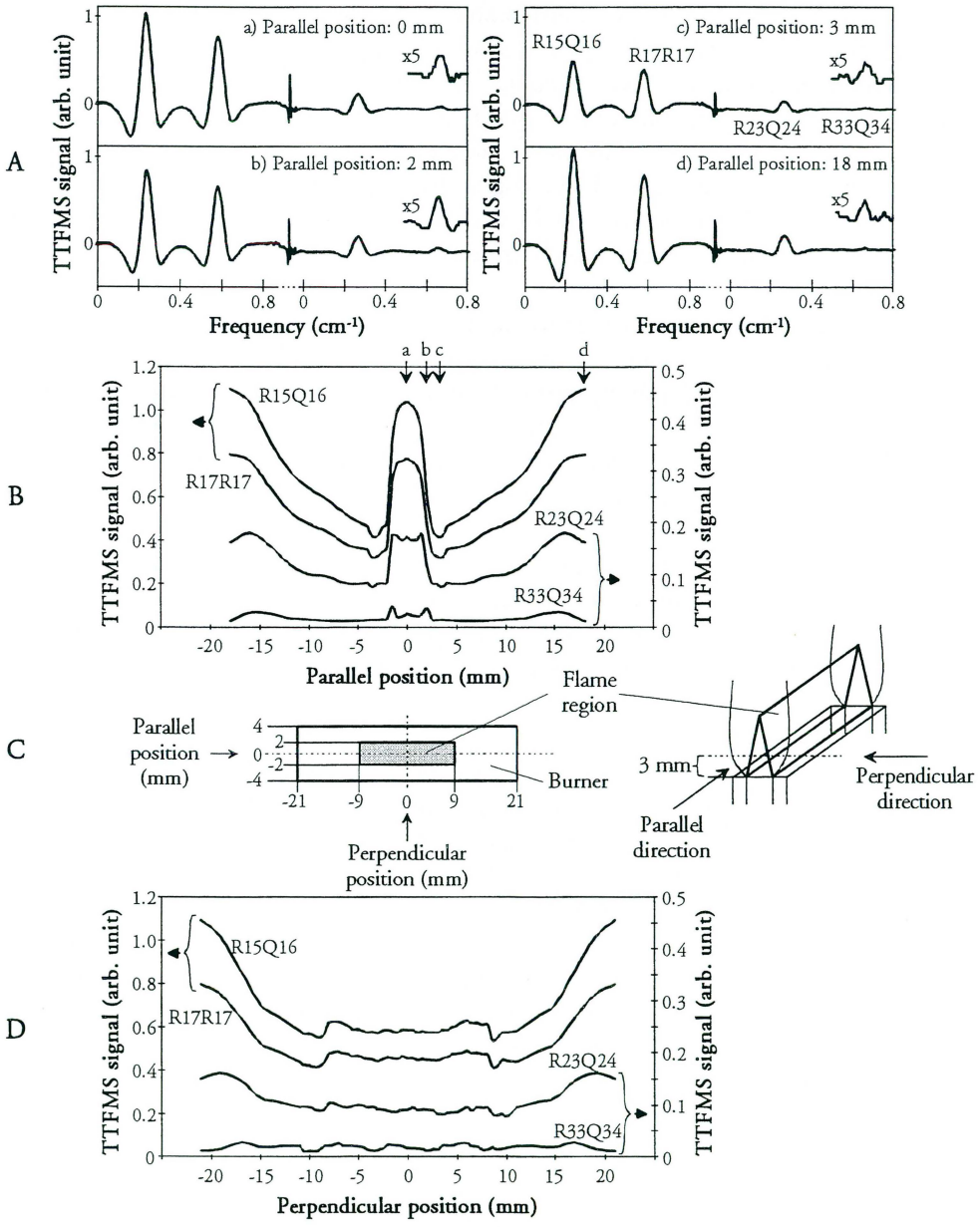

Fig. 6.3 *TTFMS absorption measurements of molecular oxygen through a methane-oxygen flame. A TTFMS signal of 1.0 corresponds to a peak absorption of* 6×10^{-4}.

6.3 Environmental monitoring

In all combustion of fossil fuels environmental pollutants are released. It is of considerable interest to develop methods for *in-situ*, real-time monitoring. Such measurement techniques are needed on global, regional as well as local scales. Remote-sensing techniques have a considerable advantage over point monitoring measurements. Optical techniques include long-path absorption measurements employing classical light sources or lasers. The DOAS (differential optical absorption spectroscopy) technique has proven itself as a particularly realistic and powerful method [6.31]. Diode lasers provide an alternative, which has been pursued within the present work (Paper IV). Lidar (light detection and ranging) provides range-resolved atmospheric measurements in a radar-like fashion. The DIAL (differential absorption lidar) allows species specific measurements [6.32].

In this department an extensive experience in the use of DOAS (see, e.g., [6.33]) and above all DIAL [6.32,6.34,6.35] exists. The work includes monitoring in urban, industrial [6.36-39] and mining areas [6.40,6.41], in geothermal fields [6.42,6.43] and at volcanoes [6.44,6.45]. The measurements have concentrated on SO_2, O_3, NO, NO_2 and Hg. A current trust is in the detection of hydrocarbons. The work presented in this thesis should be seen in this context.

Atomic mercury is an interesting geophysical tracer gas, related to ore deposits, geothermal energy and seismic and volcanic activity. In Paper V a compact system for mercury detection with isotopic specificity (for low-pressure samples) is presented. Such a system, fully engineered, could be of considerable interest for monitoring in connection with, e.g., seismic rift zones.

Methane is a greenhouse gas present in a typical 1.7 ppm outdoor abundance. It can serve as a model for general hydrocarbon monitoring, since it absorbs around 3.4 μm where the basic C-H stretch vibrational mode of hydrocarbons occurs. Paper VI reports on the development of a difference frequency diode laser spectrometer capable of remote monitoring of ambient methane concentration. At reduced pressure, isotopic selectivity was also achieved like for mercury, a feature which is of considerable geo- and biochemical interest [6.46]. The feasibility of diode-laser-based hydrocarbon monitoring is important for the detection of leaks and emissions from, e.g., petrochemical plants, refineries and pipelines. The techniques can also provide absolute calibration of passive gas correlation imaging measurements for hydrocarbons [6.47,6.48].

Atmospheric particulate matter can be studied with the lidar technique, where the backscattered signal is generated by elastic scattering from the particles. The extraction of information on particles is complex. A more detailed information can be obtained

in point monitoring, where the extinction loss in a coupled-cavity diode laser as well as the diffraction image from individual particles could be studied (Paper I).

Apart from monitoring of gases, optical measurements can also be used in reflectance and fluorescence schemes to monitor water and vegetation parameters. Broad-band signals are obtained since the molecules interact strongly. Reflectance information is largely obtained from satellites for earth resource monitoring. Active laser-induced fluorescence lidar systems can complement reflectance measurements but are necessarily restricted to short ranges [6.49-6.51]. LIF lidar systems yield information on water quality and on vegetation. Point monitoring of vegetation, e.g. as demonstrated in Paper VII, can be valuable also for a better understanding of observed LIF lidar signals.

6.4 Medical diagnostics

Optical spectroscopic techniques in medicine concern gas analysis (breath gases, anesthetic gases) but especially tissue diagnostics. Tissue investigations include quasi-elastic scattering (Doppler perfusion monitoring), and in particular LIF and Raman spectroscopy. Spectroscopic aspects are also very important in treatment based on lasers, since the tissue absorption and scattering largely govern the outcome. The field of laser applications in medicine is treated, e.g., in [6.52-6.54]. It includes thermal treatment, photodynamic therapy (PDT), cancer and atherosclerotic plaque monitoring and optical mammography. An extensive experience in these fields exists in our department. Whereas thermal treatment is the most widespread application of lasers in medicine, PDT is a strongly emerging field for selective tumour cell eradication based on selective uptake of tumour-seeking agents and a subsequent laser-mediated singlet-oxygen production in the tissue [6.55-6.58]. The generation of high-power visible diode laser light has been very beneficial for PDT, which can now be performed using compact 635 nm high-power diode lasers, replacing previously employed very bulky systems, weighing a few hundreds of kilograms.

Tumour diagnostics based in LIF rely on the occurrence of specific spectral signatures due to administered tumour-seeking fluorescence agents. Fibre-based fluorosensors of different types have been developed for clinical work [6.59,6.60]. In Paper VII the most compact LIF system developed so far is described. It constitutes a further illustration of the impact of the new blue/violet diode lasers. Point LIF monitors of this kind are used, e.g., through the biopsy channel of an endoscope [6.61-6.63]. Real-time imaging systems, which frequently are quite complex, have been developed to provide fast surveillance of larger areas [6.64-6.67].

Raman spectroscopy has the potential to yield more specific information on the tissue chemical composition since sharp peaks coupled to vibrational modes are observed [6.68,6.69]. The diploma thesis by the author falls in this field [6.70]. More recently,

extensive work has been pursued in the field of Raman and the related field of near-infrared spectroscopy (see, e.g., [6.71]).

As a further field of laser use in medicine the emerging activity in optical mammography should be mentioned [6.72]. Strong multiple scattering in tissue tends to blur image information, but using pulsed lasers and gated detection in a laser-radar-like fashion scattered light can be strongly suppressed [6.73-76].

Acknowledgements

First of all, I would like to express my gratitude to my supervisor, Sune Svanberg. His never-ending enthusiasm and positive attitude inspired me to start this work and also helped me carry it through.

The nice joint work and friendship with my further collaborators Jonas Sandsten, Petter Weibring, Gabriel Somesfalean, Janis Alnis, Sara Pålsson and Hans Edner is highly appreciated, as is the valuable assistance of all the Atomic Physics Division staff.

A special thank to Peter Kauranen, who guided me into the field of diode laser spectroscopy. The collaboration with Viacheslav Avetisov in the early stage of this project, especially regarding the flame data recording, is greatly acknowledged.

Finally, I would like to thank my family and friends, and express my sincerest appreciation for the support and encouragement that they have given me.

Summary of papers

Paper I. A new instruments based on a diode laser in a coupled cavity was developed for aerosol particle size and shape determinations. A novel feature is the simultaneous particle optical extinction measurement and diffraction image capture in the near-forward scattered light.

Paper II. This paper constitutes, to our knowledge, the first submitted paper demonstrating atomic laser spectroscopy with continuous-wave tuneable blue diode lasers. Measurements were performed on free potassium atoms, and Doppler profiles recorded on the blue 404 nm transitions were compared to data for the near-infrared 770 nm line.

Paper III. First sensitive frequency-modulation spectroscopy measurements with blue continuous-wave diode lasers were demonstrated on ground-state potassium atoms, and lead atoms in very weakly populated meta-stable states.

Paper IV. Long-path-absorption monitoring of atmospheric NO_2 using high-frequency two-tone frequency modulation spectroscopy with a continuous-wave 635-nm diode laser was demonstrated. The possibility of using comparatively weak NO_2 absorption lines was pointed out.

Paper V. This paper constitutes, to our knowledge, the first published atomic laser spectroscopy paper employing blue diode lasers. Sum-frequency generation to the mercury 254 nm lines was accomplished and low-pressure isotope selective spectroscopy as well as atmospheric pressure monitoring were demonstrated.

Paper VI. Simultaneous open-air monitoring of CH_4, H_2O and O_2 using diode laser absorption spectroscopy was accomplished using a difference-frequency generation scheme employing two near-infrared diode lasers. The simultaneous spectroscopic use of all three laser wavelengths involved had previously not been exploited. The CH_4 monitoring at 3.4 μm was possible with ambient CH_4 levels over a 15 m path and an isotopic molecular selectivity at reduced pressures was demonstrated.

Paper VII. A very compact instrument for spectroscopic measurements using laser-induced fluorescence was constructed and employed in monitoring of malignant human tumours. This is the most compact spectrally resolving fluorosensor described, exploiting the recent availability of violet diode lasers and integrated spectrometers.

Paper VIII. Temporal compression of optical pulses and pulse trains was performed using the photon echo process. Using a high-speed-frequency tuneable external cavity diode laser, single pulse temporal compression by a factor of almost 500 and pulse train compression by almost a factor 100 were demonstrated.

Contributions by the author to the different papers

Paper I. Contributions to the experimental work, data evaluation, figure and manuscript preparation.

Paper II. Major part of experimental and evaluation work. Contributions to the manuscript, and all figure preparation.

Paper III. Experimental build-up and major contributions to the experiments. Major part of the data evaluation and manuscript preparation.

Paper IV. Contribution to system integration and some measurements.

Paper V. Involvement in measurements and analysis.

Paper VI. Main responsible for system integration. Heavy involvement in measurements and manuscript preparations.

Paper VII. Shared work in system integration, measurements, data evaluation and figure preparation.

Paper VIII. Assistance to younger graduate students starting up in diode laser spectroscopy.

References

2.1 W. Chow, S. W. Koch, and M. Sargent III, *Semiconductor-Laser Physics* (Springer Verlag, Heidelberg 1994).

2.2 P. Agrawal and N. K. Dutta, *Semiconductor Lasers* (Van Nostrand Reinhold, New York 1993, 2nd Edition).

2.3 K. Petermann, *Laser Diode Modulation and Noise* (Kluwer Academic Publishers, Dordrecht 1988).

2.4 J. Hecht, *The Laser Guidebook*, (McGraw-Hill, New York 1992, 2nd edition), p. 297.

2.5 R. N. Hall, G. E. Fenner, J. D. Kingsley, T. J. Soltys, and R. O. Carlson, *Coherent light emission from a GaAs junction*, Phys. Rev. Lett. **9**, 366 (1962).

2.6 M. I. Nathan, W. P. Dumke, G. Burns, F. H. Dill, Jr., and G. Lasher, *Stimulated emission of radiation from GaAs p-n junctions*, Appl. Phys. Lett. **1**, 62 (1962).

2.7 N. Holonyak, Jr. and S. F. Bevacqua, *Coherent (visible) light emission from* $Ga(As_{1-x}P_x)$ *junctions*, Appl. Phys. Lett. **1**, 82 (1962).

2.8 T. M. Quist, R. H. Rediker, R. J. Keyes, W. E. Krag, B. Lax, A. L. McWhorter, and H. J. Zeigler, *Semiconductor maser of GaAs*, Appl. Phys. Lett. **1**, 91 (1962).

2.9 J. F. Butler, A. R. Calawa, R. J. Phelan, Jr., T. C. Harman, A. J. Strauss, and R. H. Rediker, *PbTe diode laser* , Appl. Phys. Lett. **5**, 75 (1964).

2.10 H. Kroemer, *A proposed class of heterojunction injection lasers*, Proc. IEEE 51, 1782 (1963).

2.11 Zh. I. Alferov and R. F. Kazarinov, Inventor's certificate 181737 (U.S.S.R.), 1963.

2.12 I. Hayashi, M. B. Panish, P. W. Foy, and S. Sumski, *Junction lasers which operate continously at room temperature*, Appl. Phys. Lett. **17**, 109 (1970).

2.13 Zh. I. Alferov, V. M. Andreev, D. Z. Garbuzov, Yu. V. Zhilyaev, E. P. Morozov, E. L. Portnoi, and V. G. Trofim, *Investigations of the influence of the AlAs-GaAs heterostructure parameters on the laser threshold current and the realization of continuous emission at room temperature*, Sov. Phys. Semicond. **4**, 1573 (1971).

2.14 K. Oe, S. Ando, and K. Sugiyama, *1.3 μm cw operation of GaInAsP/InP DH diode lasers at room temperature*, Jpn. J. Appl. Phys. **16**, 1273 (1977).

2.15 S. Akabi, K. Sakai, Y. Matsushima, and T. Yamamoto, *Room temperature c.w. operation of InGaAsP/InP heterostructure lasers emitting at 1.56 μm*, Electron. Lett. **15**, 606 (1979).

2.16 G. D. Henshall and P. D. Greene, *Low-threshold (Ga, In) (As, P) D.H. lasers emitting at 1.55 μm grown by L.P.E.*, Electron. Lett. **15**, 621 (1979).
2.17 H. Kawaguchi, T. Takahei, Y. Toyoshime, H. Nagai and G. Iwane, *Room-temperature c.w. operation of InP/InGaAsP/InP double heterostructure diode lasers emitting at 1.55 μm*, Electron. Lett. **15**, 669 (1979).
2.18 I. P. Kaminow, R. E. Nahory, M. A. Pollak, L. W. Stulz, and J. C. Dewinter, *Single-mode c.w. ridge-waveguide laser emitting at 1.55 μm*, Electron Lett. **15**, 763 (1979).
2.19 K. Kobayashi, S. Kawata, A. Gomyo, I. Hino, and T. Suzuki, *Room-temperature cw operation of AlGaInP double-heterostructure visible lasers*, Electron. Lett. **21**, 931 (1985).
2.20 M. Ikeda, Y. Mori, H. Sato, K. Kaneko, and N Watanabe, *Room-temperature continous-wave operation of an AlGaInP double heterostructure laser grown by atmospheric pressure metalorganic chemical vapor deposition*, Appl. Phys. Lett. **47**, 1027 (1985).
2.21 K. Itaya, M. Ishikawa, and Y. Uematsu, *636 nm room temperature cw operation by heterobarrier blocking structure InGaIP*, Electron. Lett. **26**, 839 (1990).
2.22 G. Hatakoshi, K. Itaya, M. Ishikawa, M. Okajima, and Y. Uematsu, *Short-wavelength InGaAlP visible diode lasers*, IEEE J. Quantum Electron. **QE-27**, 1476 (1991).
2.23 H. Hamada, M. Shono, S. Honda, R. Hiroyama, K. Yodoshi, and T. Yamaguchi, *AlGaInP visible laser diode grown on misoriented substrates*, IEEE J. Quantum Electron. **QE-27**, 1483 (1991).
2.24 S. Nakamura and G. Fasol, *The Blue Laser Diodes* (Springer Verlag, Heidelberg 1997).
2.25 H. C. Casey, Jr. and M. B. Panish, *Heterostructure Lasers, Part A and B* (Academic Press, Orlando 1978).
2.26 H. I. Schiff, G. I. Mackay, and J. Bechara, *The use of tunable diode laser absorption spectroscopy for atmospheric measurements*, in *Air Monitoring by Spectroscopic Techniques*, Ed. M. W. Sigrist, Chemical Analysis Series vol. 127, p. 239, (John Wiley & Sons, New York 1994).
2.27 P. Werle, *A review of recent advances in semiconductor laser based gas monitors*, Spectrochim. Acta A **54**, 197(1998).
2.28 J. C. Camparo, *The diode laser in atomic physics*, Contemp. Phys. **26**, 443 (1985).
2.29 C. E. Wieman and L. Hollberg, *Using diode lasers for atomic physics*, Rev. Sci. Instrum. **62**, 1 (1991).
2.30 A. Fried, B. Henry, and J. R. Drummond, *Tunable diode laser ratio measurements of atmospheric constituents by employing dual fitting analysis and jump scanning*, Appl. Opt. **32**, 821 (1993).
2.31 B. Dahmani, L. Hollberg, and L. Drullinger, *Frequency stabilisation of semiconductor lasers by resonant optical feedback*, Opt. Lett. **12**, 876 (1987).

2.32 M. W. Fleming and A. Mooradian, *Spectral characteristics of external-cavity controlled semiconductor lasers*, IEEE J. Quantum. Electron. **QE-17**, 44 (1988).

2.33 K. B. MacAdam, A. Steinbeck, and C. Wieman, *A narrow-band tunable diode laser system with grating feedback, and saturated absorption spectroscopy for Cs and Rb*, Am. J. Physics **60**, 1098 (1992).

2.34 K. G. Libbrecth, R. A. Boyd, P. A. Willems, T. L. Gustavson, and D. K. Kim, *Teaching physics with 670 nm diode lasers - construction of stabilized lasers and lithium cells*, Am. J. Phys. **63**, 729 (1995).

2.35 L. Ricci, M. Weidemüller, T. Esslinger, A. Hemmerich, C. Zimmerman, V. Vuletic, W. König, and T. W. Hänsch, *A compact grating-stabilized diode laser system for atomic physics*, Opt. Comm. **117**, 541 (1995).

2.36 R. Nilsson, *Konstruktion och test av en externkavitetsdiodlaser med snabb frekvensavstämning*, Diploma Paper (Lund Reports on Atomic Physics **LRAP-241**, Lund 1998).

2.37 K. Liu and M. G. Littman, *Novel geometry for single-mode scanning tunable lasers*, Opt. Lett. **6**, 117 (1981).

2.38 K. C. Harvey and C. J. Myatt, *External-cavity diode laser using a grazing-incidence diffraction grating*, Opt. Lett. **16**, 910 (1991).

2.39 D. Wandt, M. Laschek, K. Przyklenk, A. Tünnermann, and H. Welling, *External cavity laser diode with 40 nm continous tuning range around 825 nm*, Opt. Comm. **130**, 81 (1996).

2.40 D. Wandt, M. Laschek, A. Tünnermann, and H. Welling, *Continously tunable external-cavity diode laser with a double-grating arrangement*, Opt. Lett. **22**, 390 (1997).

2.41 M. de Labachelerie and G. Passedat, *Mode-hop suppression of Littrow grating-tuned lasers*, Appl. Opt. **32**, 269 (1993).

2.42 P. McNicholl and H. J. Metcalf, *Synchronous cavity mode and feedback wavelength scanning in dye laser oscillators with gratings*, Appl. Opt. **24**, 2757 (1985).

2.43 F. S. Luecke, *Tuning system for external cavity diode laser*, United States Patent 53919668 (1994).

2.44 F. Favre, D. Le Guen, J. C. Simon, and B Landousiers, *External-cavity semiconductor laser with a 15 nm continous tuning range*, Electron Lett. **22**, 795 (1986).

3.1 L. S. Rothman, C. P. Rinsland, A. Goldman, S. T. Massie, D. P. Edwards, J.-M. Flaud, A. Perrin, C. Camy-Peyret, V. Dana, J.-Y. Mandin, J. Schroeder, A. McCann, R. R. Gamache, R. B. Wattson, K. Yoshino, K. V. Chance, K. W. Jucks, L. R. Brown, V. Nemtchinov, and P. Varanasi, *The HITRAN molecular spectroscopic database and HAWKS (HITRAN Atmospheric Workstation): 1996 edition*, J. Quant. Spectrosc. Radiat. Transfer **60**, 665 (1998).

3.2 W. Voigt, *Über das Gesetz der Intensitetsverteilung innerhalb der Linien eines Gasspektrums*, Sitzber. Acad. Wiss. München, Volume of 1912, 603 (1912).
3.3 J. Humlicek, *Optimized computation of the Voigt and the complex probability function*, J. Quant. Spectrosc. Radiat. Transfer **27**, 437 (1982).
3.4 J. J. Olivieri and R. L. Longbothum, *Empirical fits to the Voigt line width: a brief review*, J. Quant. Spectrosc. Radiat. Transfer **17**, 233 (1977).
3.5 D. R. Herriot, H. Kogelnik, and R. Kompfner, *Off-axis paths in spherical mirror resonators*, Appl. Opt. **3**, 523 (1964).
3.6 D. R. Herriot and H. J. Schulte, *Folded optical delay lines*, Appl. Opt. **4**, 883 (1965).
3.7 J. U. White, *Long optical paths of large aperture*, J. Opt. Soc. Am. **32**, 285 (1942).
3.8 J. U. White, *Very long optical paths in air*, J. Opt. Soc. Am. **66**, 411 (1976).
3.9 J. B. MacManus, P. L. Kebabian, and M. S. Zahniser, *Astigmatic mirror multipass cell for long-path-length spectroscopy*, Appl. Opt. **34**, 3336 (1995).
3.10 A. O'Keefe and D. A. G. Deacon, *Cavity ring-down spectrometer for absorption measurements using pulsed laser sources*, Rev. Sci. Instrum. **59**, 2544 (1988).
3.11 M. D. Wheeler, S. M. Newman, A. J. Orr-Ewing, and M. N. R. Ashfold, *Cavity ring-down spectroscopy*, J. Chem. Soc. Faraday Trans. **94**, 337 (1998).
3.12 V. M. Baev, J. Eshner, E. Paeth, R. Schüler, and P. E. Toschek, *Intra-cavity spectroscopy with diode lasers*, Appl. Phys. B **55**, 463 (1992).
3.13 M. W. Sigrist, *Air monitoring by laser photoacoustic spectroscopy*, in *Air Monitoring by Spectroscopic Techniques*, Ed. M. W. Sigrist, Chemical Analysis Series vol. 127, p. 163, (John Wiley & Sons, New York 1994).
3.14 P. Hess (Ed.), *Photoacoustics* (Springer Verlag, Heidelberg 1990).
3.15 J. Travis and G. Turk (Eds.), *Laser-Enhanced Ionization Spectrometry* (John Wiley & Sons, New York 1996).

4.1 E. I. Moses and C. L. Tang, *High sensitivity laser wavelength modulation spectroscopy*, Opt. Lett. **1**, 115 (1977).
4.2 J. Reid and D. Labrie, *Second-harmonic detection with tunable diode lasers - comparison of experiment and theory*, Appl. Phys. B **26**, 203 (1981).
4.3 G. C. Bjorklund, *Frequency-modulation spectroscopy: a new method for measuring weak absorptions and dispersions*, Opt. Lett. **5**, 15 (1980).
4.4 G. C. Bjorklund, M. D. Levenson, W. Lenth, and C. Ortiz, *Frequency modulation (FM) spectroscopy. Theory of lineshapes and signal-to-noise ratios*, Appl. Phys. B **32**, 145 (1983).
4.5 W. Lenth, *High frequency heterodyne spectroscopy with current modulated diode lasers*, IEEE. J. Quantum Electron. **QE-20**, 1045 (1984).
4.6 W. Lenth, M. Gerthz, and A. T. Young, *High frequency modulation spectroscopy with tunable GaAs and lead salt diode lasers*, J. Opt. Soc. Am. A **2**, 99 (1985).

4.7 D. E. Cooper and T. F. Gallagher, *Double frequency modulation spectroscopy: high modulation frequency with low-bandwidth detectors*, Appl. Opt. **24**, 1327 (1985).

4.8 G. R. Janik, C. B. Carlisle and T. F. Gallagher, *Two-tone frequency-modulation spectroscopy*, J. Opt. Soc. Am. B **3**, 1070 (1986).

4.9 D. E. Cooper and J. P. Watjen, *Two-tone optical heterodyne spectroscopy with a tunable lead-salt diode laser*, Opt. Lett. **11**, 606 (1986).

4.10 D. E. Cooper and R. E. Warren, *Two-tone optical heterodyne spectroscopy with diode lasers: theory of line shapes and experimental results*, J. Opt. Soc. Am. B **4**, 470 (1987).

4.11 J. A. Silver and A. C. Stanton, *Two-tone optical heterodyne spectroscopy using buried double heterostructure lead-salt diode lasers*, Appl. Opt. **27**, 4438 (1988).

4.12 V. G. Avetisov and P. Kauranen, *Two-tone frequency-modulation spectroscopy for quantitative measurements of gaseous species: theoretical, numerical and experimental investigations*, Appl. Opt. **35**, 4705 (1996).

4.13 V. G. Avetisov and P. Kauranen, *High-resolution absorption measurements by use of two-tone frequency modulation spectroscopy with diode lasers*, Appl. Opt. **36**, 4043 (1997).

4.14 C. B. Carlisle, D. E. Cooper, and H. Preier, *Quantum noise-limited FM spectroscopy with a lead-salt diode laser*, Appl. Opt. **28**, 2567 (1989).

4.15 C. B. Carlisle and D. E. Cooper, *Tunable-diode-laser frequency-modulation spectroscopy using balanced homodyne detection*, Opt. Lett. **14**, 1306 (1989).

4.16 P. Werle, F. Slemr, M. Gehrtz, and C. Bräuchle, *Quantum-limited FM-spectroscopy with a lead salt diode laser*, Appl. Phys. B **49**, 99 (1989).

4.17 F. S. Pavone and M. Inguscio, *Frequency- and wavelength-modulation spectroscopies: comparison of experimental methods using an AlGaAs diode laser*, Appl. Phys. B **56**, 118 (1993).

4.18 G. Modugno, C. Corsi, M. Gabrysch, F. Marin, and M. Inguscio, *Fundamental noise sources in high-sensitivity two-tone frequency modulation spectrometer and detection of CO_2 at 1.6 μm and 2 μm*, Appl. Phys. B **67**, 289 (1998).

4.19 L. Wang, H. Riris, C. B. Carlisle and T. F. Gallagher, *Comparison of approaches to modulation spectroscopy with GaAlAs semiconductor lasers: application to water vapor*, Appl. Opt. **27**, 2071 (1988).

4.20 J. A. Silver, *Frequency-modulation spectroscopy for trace species detection: theory and comparison among experimental methods*, Appl. Opt. **31**, 707 (1992).

4.21 D. S. Bomse, A. C. Stanton and J. A. Silver, *Frequency modulation and wavelength modulation spectroscopies: comparison of experimental methods using a lead-salt diode laser*, Appl. Opt. **31**, 718 (1992).

4.22 J. M. Supplee, E. A. Whittaker, and W. Lenth, *Theoretical description of frequency modulation and wavelength modulation spectroscopy*, Appl. Opt. **33**, 6294 (1994).

4.23 U. Platt, *Differential optical absorption spectroscopy (DOAS)*, in *Air Monitoring by Spectroscopic Techniques*, Ed. M.W. Sigrist, Chemical Analysis Series 127, p. 27 (John Wiley, New York 1994).

4.24 D. E. Jennings, *Absolute line strength in ν_4 $^{12}CH_4$: a dual beam diode laser spectrometer with sweep integration*, Appl. Opt. **19**, 2695 (1980).

4.25 D. T. Cassidy and J. Reid, *High-sensitivity detection of trace gases using sweep integration and tunable diode lasers*, Appl. Opt. **21**, 2527 (1982).

4.26 H. G. Wang, D. A, Tate, H. Riris, and T. F. Gallagher, *High-sensitivity frequency-modulation spectroscopy with GaAlAs diode laser*, J. Opt. Soc. Am. B **6**, 871 (1989).

4.27 C. R. Webster, *Brewster-plate spoiler: a novel method for reducing the amplitude of interference fringes that limit tunable-laser absorption sensitivities*, J. Opt. Soc. Am. B **2**, 1464 (1985).

4.28 J. A. Silver and A. C. Stanton, *Optical interference fringe reduction in laser absorption measurements*, Appl. Opt. **27**, 1914 (1988).

4.29 D. E. Cooper and C. B. Carlisle, *High-sensitivity FM spectroscopy with lead-salt diode lasers*, Opt. Lett. **13**, 719 (1988).

4.30 H. Riris, C. B. Carlisle, R. E. Warren, and D. E. Cooper, *Signal-to-noise ratio enhancement in frequency-modulation spectrometers by digital signal processing*, Opt. Lett. **19**, 144 (1994).

4.31 H. Riris, C. B. Carlisle, and R. E. Warren, *Kalman filtering of tunable diode laser spectrometer absorbance measurements*, Appl. Opt. **33**, 5506 (1994).

4.32 P. Werle, F. Slemr, M. Gehrtz, and C. Bräuchle, *Wideband noise characteristics of lead salt diode laser: possibility of quantum noise limited TDLAS performance*, Appl. Opt. **28**, 1638 (1989).

4.33 P. Werle, *Laser excess noise and inteferometric effects in frequency-modulated diode-laser spectrometers*, Appl. Phys. B. **60**, 449 (1995).

5.1 Y. R. Shen, *The Principles of Nonlinear Optics* (John Wiley & Sons, New York 1992).

5.2 R. W. Boyd, *Nonlinear Optics* (Academic Press, San Diego 1992).

5.3 P. A. Franken, A. E. Hill, C. W. Peters, and G. Weinreich, *Generation of optical harmonics*, Phys. Rev. Lett. **7**, 118 (1961).

5.4 J. A. Giordmaine, *Mixing of light beams in crystals*, Phys. Rev. Lett. **8**, 19 (1962).

5.5 P. D. Maker, R. W. Terhune, M. Nisenoff, and C. M. Savage, *Effects of dispersion and focusing on the production of optical harmonics*, Phys. Rev. Lett. **8**, 21 (1962).

5.6 J. E. Midwinter and J. Warner, *The effects of phase matching method and of uniaxial crystal symmetry on the polar distribution of second-order non-linear optical polarization*, Brit. J. Appl. Phys. **16**, 1135 (1965).

5.7 J. A. Armstrong, N. Bloembergen, J. Ducuing, and P. S. Pershan, *Interaction between light waves in a nonlinear dielectricum*, Phys. Rev. **127**, 1918 (1962).

5.8 M. M. Fejer, G. A. Magel, D. H. Jundt, and R. L. Byer, *Quasi-phase-matched second harmonic generation: tuning and tolerances*, IEEE. J. Quantum. Electron. **28**, 2631 (1992).

5.9 V. G. Dmitriev, G. G. Gurzadyan, and D. N. Nikogosyan, *Handbook of Nonlinear Optical Crystals* (Springer Verlag, Heidelberg 1991).

5.10 L. E. Myers, R. C. Eckhardt, M. M. Fejer, R. L. Byer, W. R. Rosenberg, and J. W. Pierce, *Quasi-phase-matched optical parametric oscillators in bulk periodically poled $LiNbO_3$*, J. Opt. Soc. Am. B **12**, 2102 (1995).

5.11 M. M. Fejer, *Nonlinear optical frequency conversion*, Physics Today May 1994, p. 25.

5.12 G. J. Dixon, *Periodically poled lithium niobate shines in the IR*, Laser Focus World May 1997, p. 105.

5.13 G. D. Boyd and D. A. Kleinman, *Parametric interaction of focused Gaussian light beams*, J. Appl. Phys. **39**, 3597 (1968).

5.14 T.-B. Chu and M. Broyer, *Intracavity cw difference frequency generation by mixing three photons and using Gaussian laser beams*, J. Physique **46**, 523 (1985).

6.1 G. Mie, *Beiträge zur Optik trüber Medien, speziell kolloidaler Metallösungen*, Ann. Physik **25**, 377 (1908).

6.2 C. van de Hulst, *Light Scattering by Small Particles* (John Wiley & Sons, New York 1957).

6.3 W. C. Strahle, *An Introduction to Combustion* (Gordon and Breach, Langhorne 1993).

6.4 G. Cox, *Combustion Fundamentals of Fire* (Academic, London 1995).

6.5 A. C. Eckbreth, *Laser Diagnostics for Combustion Temperature and Species* (Gordon & Breach, Amsterdam 1996).

6.6 M. Aldén, H. Edner, G. Holmstedt, S. Svanberg, and T. Högberg, *Single-pulse laser-induced OH fluorescence in an atmospheric flame, spatially resolved with a diode array detector*, Appl. Opt. **21**, 1236 (1982).

6.7 M. Aldén, H. Edner, and S. Svanberg, *Simultaneous spatially resolved monitoring of C_2 and OH in a C_2H_2/O_2 flame using a diode array detector*, Appl. Phys. B **29**, 93 (1982).

6.8 R. K. Hanson, *Planar laser-induced fluorescence imaging*, J. Quant. Spectrosc. Radiat. Transfer **40**, 343 (1988).

6.9 U. Westblom and M. Aldén, *Simultaneous multiple species detection in a flame using laser-induced fluorescence*, Appl. Opt. **28**, 2592 (1989).

6.10 R. K. Hanson, J. M. Seitzman, and P. H. Paul, *Planar laser-fluorescence imaging of combustion gases*, Appl. Phys. B **50**, 441 (1990).

6.11 W. Reckers, L. Huwel, G. Grunewald, and P. Andresen, *Spatially resolved multispecies and temperature analysis in hydrogen flames*, Appl. Opt. **32**, 907 (1993).
6.12 R. K. Hanson, P. A. Kuntz, and C. H. Kruger, *High-resolution spectroscopy of combustion gases using a tunable ir diode laser*, Appl. Opt. **16**, 2045 (1977).
6.13 R. K. Hanson and P. K. Falcone, *Temperature measurement technique for high-temperature gases using a tunable diode laser*, Appl. Opt. **17**, 2477 (1978).
6.14 X. Ouyang and P. L. Varghese, *Line-of-sight absorption measurements of high temperature gases with thermal and concentration boundary layers*, Appl. Opt. **28**, 3979 (1989).
6.15 X. Ouyang and P. L. Varghese, *Selection of spectral lines for combustion diagnostics*, Appl. Opt. **29**, 4884 (1990).
6.16 L. C. Philippe and R. K. Hanson, *Laser diode wavelength-modulation spectroscopy for simultaneous measurements of temperature, pressure, and velocity in shock-heated oxygen flows*, Appl. Opt. **32**, 6090 (1993).
6.17 D. S. Baer, R. K. Hanson, M. E. Newfield, and N. K. J. M. Gopaul, *Multiplexed diode-laser sensor system for simultaneous H_2O, O_2, and temperature measurements*, Opt. Lett. **19**, 1900 (1994).
6.18 R. G. Daniel, K. L. McNesby, and A. W. Miziolek, *Applications of tunable diode laser diagnostics for temperature and species concentration profiles of inhibited low-pressure flames*, Appl. Opt. **35**, 4018 (1996).
6.19 V. Nagali, S. I. Chou, D. S. Baer, R. K. Hanson, and J. Segall, *Tunable diode-laser measurements of methane at elevated temperatures*, Appl. Opt. **35**, 4026 (1996).
6.20 R. M. Mihalcea, D. S. Baer, and R. K. Hanson, *Diode laser sensor for measurements of CO, CO_2, and CH_4 in combustion flows*, Appl. Opt. **36**, 8745 (1997).
6.21 I. Linnerud, P. Kaspersen, and T. Jaeger, *Gas monitoring in the process industry using diode lasers*, Appl. Phys. B **67**, 297 (1998).
6.22 P. J. Emmerman, R. Goulard, R. J. Santaro, and H. G. Semerjian, *Multiangular absorption diagnostics of a turbulent argon-methane jet*, J. Energy **4**, 70 (1980).
6.23 K. E. Bennet, G. W. Faris, and R. L. Byer, *Experimental optical fan beam tomography*, Appl. Opt. **23**, 2678 (1984).
6.24 G. W. Faris and R. L. Byer, *Quantitative optical tomographic imaging of a supersonic jet*, Opt. Lett. **11**, 413 (1986).
6.25 G. W. Faris and R. L. Byer, *Beam-deflection optical tomography of a flame*, Opt. Lett. **12**, 155 (1987).
6.26 Q. V. Nguyen, R. W. Dibble, D. Hofmann, and S. Kampmann, *Tomographic measurements of carbon monoxide temperature and concentration in a Bunsen flame using diode laser absorption*, Ber. Bunsenges. Phys. Chem. **97**, 1634 (1993).

6.27 P. Kauranen, H. M. Hertz, and S. Svanberg, *Tomographic imaging of fluid flows by the use of two-tone frequency-modulation spectroscopy*, Opt. Lett. **19**, 1489 (1994).

6.28 K. L. McNesby, R. G. Daniel, J. B. Morris, and A. W. Miziolek, *Tomographic analysis of CO absorption in a low-pressure flame*, Appl. Opt. **34**, 3318 (1995).

6.29 J. A. Silver, D. J. Kane, and P. S. Greenberg, *Quantitative species measurements in microgravity flames with near-IR diode lasers*, Appl. Opt. **34**, 2787 (1995).

6.30 H. M. Hertz, *Kerr effect tomography for nonintrusive spatially resolved measurements of asymmetric electric field distributions*, Appl. Opt. **25**, 914 (1986).

6.31 U. Platt, *Differential optical absorption spectroscopy (DOAS)*, in *Air Monitoring by Spectroscopic Techniques*, Ed. M.W. Sigrist, Chemical Analysis Series 127, p. 27 (John Wiley, New York 1994).

6.32 S. Svanberg, *Differential absorption lidar (DIAL)*, in *Air Monitoring by Spectroscopic Techniques*, Ed. M. W. Sigrist, Chemical Analysis Series vol. 127, p. 85 (John Wiley & Sons, New York 1994).

6.33 H. Edner, P. Ragnarsson, S. Spännare, and S. Svanberg, *Differential optical absorption spectroscopy (DOAS) system for urban atmospheric pollution monitoring*, Appl. Opt. **32**, 327 (1993).

6.34 H. Edner, K. Fredriksson, A. Sunesson, S. Svanberg, L. Unéus, and W. Wendt, *Mobile remote sensing system for atmospheric monitoring*, App. Opt. **26**, 4330 (1987).

6.35 P. Weibring, M. Andersson, H. Edner, and S. Svanberg, *Remote monitoring of industrial emissions by combination of lidar and plume velocity measurements*, Appl. Physics B **66**, 383 (1998).

6.36 K. A. Fredriksson and H. M. Hertz, *Evaluation of the DIAL technique for studies on NO_2 using a mobile lidar system*, Appl. Opt. **23**, 1403 (1984).

6.37 H. Edner, G.W. Faris, A. Sunesson, and S. Svanberg, *Atmospheric atomic mercury monitoring using differential absorption lidar techniques*, Appl. Opt. **28**, 921 (1989).

6.38 R. Ferrara, B. E. Maserti, H. Edner, P. Ragnarson, S. Svanberg, and E. Wallinder, *Mercury emissions into the atmosphere from a chlor-alkali complex measured with the lidar technique*, Atmospheric Environment **26A**, 1253 (1992).

6.39 H. Edner, P. Ragnarsson, and E. Wallinder, *Industrial emission control using lidar techniques*, Environ. Sci. Technol. **29**, 330 (1995).

6.40 H. Edner, P. Ragnarson, S. Svanberg, E. Wallinder, R. Ferrara, B. E. Maserti, and R. Bargagli, *Atmospheric mercury mapping in a cinnabar mining area*, The Science of the Total Environment **133**, 1 (1993).

6.41 R. Ferrari, B. M. Maserti, M. Andersson, H. Edner, P. Ragnarson, S. Svanberg, and A. Hernandez, *Atmospheric mercury concentration and fluxes in the Almaden district (Spain)*, Atm. Environment **32**, 3897 (1998).

6.42 H. Edner, G. W. Faris, A. Sunesson, S. Svanberg, J. Ö. Bjarnason, K. H. Sigurdsson, and H. Kristmansdottir, *Lidar search for atomic mercury in Icelandic geothermal fields*, J. Geophys. Res. **96**, 2977 (1991).

6.43 H. Edner, P. Ragnarson, S. Svanberg, E. Wallinder, A. De Liso, R. Ferrara, and B. E. Maserti, *Differential absorption lidar mapping of atmospheric atomic mercury in Italian geothermal fields*, J. Geophys. Res. **97**, 3779 (1992).

6.44 H. Edner, P. Ragnarson, S. Svanberg, E. Wallinder, R. Ferrara, R. Cioni, B. Raco, and G. Taddeucci, *Total fluxes of sulphur dioxide from the Italian volcanoes Etna, Stromboli and Vulcano measured by differential absorption lidar and passive differential optical absorption spectroscopy*, J. Geophys. Res. **99**, 18827 (1994).

6.45 P. Weibring, H. Edner, S. Svanberg, G. Cecchi, L. Pantani, R. Ferrara, and T. Caltabiano, *Monitoring of volcanic sulphur dioxide emissions using differential absorption lidar (DIAL), differential optical absorption spectroscopy (DOAS), and correlation spectroscopy (COSPEC)*, Appl. Phys. B **67**, 419 (1998).

6.46 P. Bergamaschi, M. Schupp, and G. W. Harris, *High-precision direct measurements of $^{13}CH_4$ / $^{12}CH_4$ and $^{12}CH_3D$ / $^{12}CH_4$ ratios in atmospheric methane sources by means of long-path tunable diode laser absorption spectrometer*, Appl. Opt. **33**, 7704 (1994).

6.47 J. Sandsten, H. Edner, and S. Svanberg, *Gas imaging by infrared gas-correlation spectrometry*, Opt. Lett. **21**, 1945 (1996).

6.48 J. Sandsten, P. Weibring, H. Edner, and S. Svanberg, *Real-time gas-correlation imaging employing thermal background radiation*, Optics Express **6**, 92 (2000).

6.49 H. Edner, J. Johansson, S. Svanberg, and E. Wallinder, *Fluorescence lidar multi-color imaging of vegetation*, Appl. Opt. **33**, 2471 (1994).

6.50 S. Svanberg, *Fluorescence lidar monitoring of vegetation status*, Phys. Scr. T**58**, 79 (1995).

6.51 V. Raimondi, G. Cecchi, L. Pantani, and R. Chiari, *Fluorescence lidar monitoring of historical buildings*, Appl. Opt. **37**, 1089 (1996).

6.52 M. L. Wolbarsht, *Laser Applications in Medicine and Biology* (Plenum, New York 1991).

6.53 A. J. Welch and M. van Gemert, *Optical-Thermal Response of Laser-Irradiated Tissue* (Plenum, New York 1995).

6.54 S. Svanberg, *New developments in laser medicine*, Phys. Scr. T**72**, 69 (1997).

6.55 S. L. Marcus, *Photodynamic therapy: Clinical status, potential and needs*, in *Photodynamic Therapy of Human Cancer*, Ed. C. Gomer, p. 1 (SPIE Press, Bellingham 1990).

6.56 J. C. Kennedy, R. H. Potter, and D. C. Pross, *Photodynamic therapy with endogenous protoporphyrin IX: Basic principles and present clinical experience*, J. Photochem Photobiol. **6**, 143 (1990).

6.57 K. Svanberg, T. Andersson, D. Killander, I. Wang, U. Stenram, S. Andersson-Engels, R. Berg, J. Johansson, and S. Svanberg, *Photodynamic therapy of non-*

melanoma malignant tumours of the skin utilizing topical δ-amino levulinic acid sensitization and laser irradiation, British J. of Dermatology **130**, 743 (1994).

6.58 T. J. Dougherty, C. J. Gomer, B. W. Henderson, G. Jori, D. Kessel, M. Korbelik, J. Moan, and Q. Peng, *Photodynamic therapy*, J. Natl. Cancer Inst. **90**, 889 (1998).

6.59 S. Andersson-Engels, Å. Elner, J. Johansson, S.-E. Karlsson, L. G. Salford, K. Svanberg, and S. Svanberg, *Clinical recording of laser-induced fluorescence spectra for evaluation of tumour demarcation feasability in selected clinical specialities*, Lasers Med. Sci. **6**, 415 (1991).

6.60 C. af Klinteberg, M. Andreasson, O. Sandström, S. Andersson-Engels, and S. Svanberg, *Compact medical fluorosensor for minimally invasive tissue characterisation*, Manuscript (2000).

6.61 J. Hung, S. Lam, J. C. LeRiche, and B. Palcic, *Autofluorescence of normal and malignant bronchial tissue*, Lasers Surg. Med. **11**, 99 (1991).

6.62 L. Baert, R. Berg, B. Van Damme, M. A. d'Hallewin, J. Johansson, K. Svanberg, and S. Svanberg, *Clinical fluorescence diagnosis of human bladder carcinoma following low-dose photofrin injection*, J. Urology **41,** 322 (1993).

6.63 C. Eker, S. Montán, E. Jamarillo, K. Koizumi, C. Rubio, S. Andersson-Engels, K. Svanberg, S. Svanberg, and P. Slezak, *Clinical spectral characterization of colonic mucosial lesions using autofluorescence and δ-aminolevulinic acid sensitization*, Gut **44**, 511 (1999).

6.64 A. E. Profio, *Endoscopic fluorescence detection of early lung cancer*, in *Optical Methods for Tumor Treatment and Early Diagnosis: Mechanisms and Techniques,* Ed. T. J. Dougherty. SPIE **1426**, 44 (1991).

6.65 S. Andersson-Engels, C. af Klinteberg, K. Svanberg, and S. Svanberg, *In vivo fluorescence imaging for tissue diagnosis*, Phys. Med. Biol. **42**, 815 (1997).

6.66 G. A. Wagnières, W. M. Star, B. C. Wilson, *In vivo fluorescence spectroscopy and imaging for oncological applications*, Photochem. Photobiol. **68**, 603 (1998).

6.67 K. Svanberg, I. Wang, S. Colleen, I. Idvall, C. Ingvar, R. Rydell, D. Jocham, H. Diddens, S. Bown, G. Gregory, S. Montán, S. Andersson-Engels, and S. Svanberg, *Clinical multi-colour fluorescence imaging of malignant tumours - Initial experience*, Acta Radiol. **38**, 2 (1998).

6.68 J. J. Baraga, M. S. Feld, and R. P. Rava, *Rapid near-infrared Raman spectroscopy of human tissue with a spectrograph and CCD detector*, Appl. Spectr. **46**, 187 (1992).

6.69 J. J. Baraga, M. S. Feld, and R. P. Rava, *In situ histochemistry of human artery using near infrared Fourier transform Raman spectroscopy*, Proc. Natl. Acad. Sci. USA **89**, 3473 (1992).

6.70 U. Gustafsson, *Near-Infrared Raman Spectroscopy Using a Diode Laser and CCD Detector for Tissue Diagnostics* (Lund Reports on Atomic Physics **LRAP-138**, 1993).

6.71 T. J. Römer, J. F. Brennan III, M. Fitzmaurice, M. F. Feinstein, G. Deinum, J. L. Myles, J. R. Kramer, R. S. Lees, and M. S. Feld, *Histopathology of human coronary atherosclerosis by quantifying its composition with Raman spectroscopy*, Circulation **97**, 878 (1998).

6.72 G. Müller, B. Chance, R. Alfano, S. Arridge, J. Beuthan, E. Gratton, M. Kaschke, B. Masters, S. Svanberg, and P. van der Zee (Eds.), *Medical Optical Tomography, Functional Imaging and Monitoring*, SPIE Institute Series Vol. **11** (SPIE, Bellingham 1993).

6.73 S. Andersson-Engels, R. Berg, S. Svanberg, and O. Jarlman, *Time-resolved transillumination for medical diagnostics*, Opt. Letters **15**, 1179 (1990).

6.74 S. Andersson-Engels, R. Berg, and S. Svanberg, *Effects of optical constants on time-gated transillumination of tissue and tissue-like media*, J. Photochem. Photobiol. **16**, 155 (1992).

6.75 R. Berg, O. Jarlman, and S. Svanberg, *Medical transillumination imaging using short pulse diode lasers*, Appl. Opt. **32**, 574 (1993).

6.76 S. Andersson-Engels, R. Berg, A. Persson, and S. Svanberg, *Multispectral tissue characterization using time-resolved detection of diffusely scattered white light*, Opt. Lett. **18**, 1697 (1993).

I

ELSEVIER

1 September 1999

Optics Communications 168 (1999) 17–24

OPTICS COMMUNICATIONS

www.elsevier.com/locate/optcom

Single aerosol particle sizing and identification using a coupled-cavity diode laser

Jonas Sandsten *, Ulf Gustafsson, Gabriel Somesfalean

Department of Physics, Lund Institute of Technology, P.O. Box 118, S-221 00 Lund, Sweden

Received 17 July 1998; received in revised form 14 May 1999; accepted 20 June 1999

Abstract

A new instrument for aerosol particle size determination and identification by shape is presented. The instrument is based on a diode laser in a coupled cavity. An extinction loss determines the size of a single aerosol particle entering the coupled-cavity diode laser, and a Fourier transformed diffraction image of near-forward scattered light is used for shape and orientation analysis. We describe a model of the coupled-cavity diode laser using light scattering based on Mie theory. This model relates the extinction loss directly to the cross-sectional area of the aerosol particle and shows good agreement with experimental results on aerosol particles and fibers. It is demonstrated that the changes in extinction loss are essentially independent of refractive index of the aerosol particles. The measurable size range of the aerosol particles is 4–170 μm with an accuracy of ±0.5 μm. The lower limit of the range is set by the extinction loss S/N ratio, the upper limit is given by the laser beam cross-section, and the accuracy is imposed by the oscillations in the extinction efficiency factor.

PACS: 07.60.−j; 42.55.Px; 42.25.Fx
Keywords: Coupled cavity; Diode laser; Diffraction; Light scattering; Aerosol particle

1. Introduction

Allergy and asthma are known to increase because of poor indoor air quality and high levels of particulate contaminants and pollen in the outdoor environment [1]. Rapid changes in production technology and the introduction of new materials lead to new potential risks. It is desirable to be able to monitor and identify aerosol particles, such as fungal spores, microorganisms and fibers of hazardous materials, in a timely manner.

The new instrument presented in this paper allows size determination and identification by shape of aerosol particles in situ, using a commercially available diode laser in a coupled-cavity configuration with weak feedback. Detection and sizing are done by an extinction loss signal depending on light scattered out of the coupled cavity, and identification is performed using a diffraction image of near-forward scattered light.

Another technique based only on extinction loss uses an intra-cavity He–Ne laser with high mirror reflectivities [2]. A quality of our coupled-cavity configuration is the weak reflectivity of the external mirror which makes it possible to transmit near-for-

* Corresponding author. Tel.: +46-46-222-4805; fax: +46-46-222-4250; E-mail: jonas.sandsten@fysik.lth.se

0030-4018/99/$ - see front matter
PII: S0030-4018(99)00339-9

ward scattered light and distinguish aerosol particles with different shapes giving rise to the same extinction loss. Other optical techniques for aerosol particle sensing have been explored using lasers, for example time-of-flight monitoring and light scattering [3,4]. The instrument presented here distinguishes itself from existing techniques by combining an extinction loss with a diffraction image from a single particle measurement.

2. Description of the instrument

Our instrumental set-up, shown in Fig. 1, uses a diode laser in a coupled-cavity configuration, a digitizing oscilloscope, an infrared-sensitive CCD camera, and a high-resolution spectrometer. The coupled-cavity configuration consists of a single-mode AlGaAs diode laser (Sony SLD114VS) lasing at 780 nm with a free-running threshold current of 19.4 mA, an aspheric lens (Geltech 350230-B, N.A. = 0.55) which collimates the laser light to an approximately Gaussian elliptical beam with the 'top hat' full widths 0.38 mm $\times$ 0.16 mm, a 10 cm long coupled cavity and an external planar mirror with a reflectivity $R_{ext} = 4\%$. A specially designed piezo-controlled mirror mount with high angular resolution (< 1 arc sec) is used to align the coupled cavity. We also employ active control of the mirror mount with an autoalignment system (Melles Griot NanoTrak), which simplifies the alignment procedure before measurements. The reduction of the threshold current

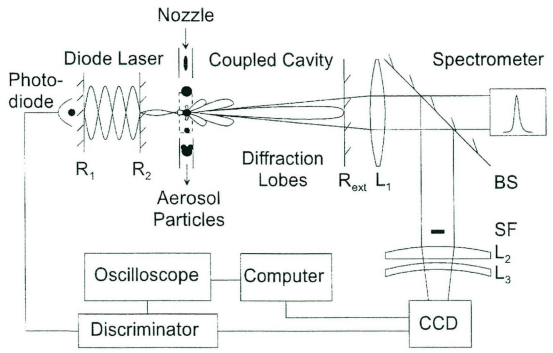

Fig. 1. Schematic of the instrumental set-up for aerosol particle measurements using extinction loss and near-forward scattered light. Laser diode facets, R_1 and R_2; planar external mirror, R_{ext}; Fourier lens, L_1; beamsplitter, BS; spatial filter, SF; Fourier-plane imaging lenses, L_2 and L_3.

with the coupled cavity is 6%. Coupling efficiency is mainly governed by the external mirror alignment, the numerical aperture of the collimator and the astigmatism of the diode laser. The coupling efficiency and the beam dimensions were investigated and simulated during the design of the instrument with an optics design software and a beam intensity profiler [5,6].

The working point, specified by the injection current, the temperature of the diode laser and the coupled-cavity length, was chosen so that the single-mode frequency of the free-running diode laser coincides with the coupled-cavity single-mode frequency. The injection current was set to 18.9 mA, which is above the threshold current of the coupled-cavity diode laser at 18.2 mA, but below the onset of the coherence collapse region at 20 mA [7]. During the design phase we have characterized the mode structure and optimized for single-mode operation of the coupled cavity with a spectrometer.

The sensing volume is comprised of the central part of the laser beam inside the coupled cavity together with the depth of field of the Fourier lens (L_1). Introduction of an aerosol particle into the sensing volume along the major axis of the beam is accomplished with a nozzle designed to position the aerosol particle in a laminar air flow passing through the center of the beam. In this way we assure the alignment of different aerosol particles due to their specific aerodynamic properties. A fiber will, for example, traverse the laser beam aligned parallel to the laminar air flow.

The extinction loss, which determines the size of the aerosol particles, is measured with the photodiode integrated in the diode-laser housing. With a level discriminator it is possible to set the instrument to sample aerosol particles of the same size distribution. One feature of the measurement scheme is that there is no need for an external photodiode, which, in combination with folded rays of the diffraction image, makes the instrument fairly compact ($0.3 \times 0.3 \times 0.2$ m^3).

In addition to measuring the extinction loss, near-forward scattered light at angles between 2 and 10° is collected and transformed with the Fourier lens (L_1). The resulting diffraction pattern is imaged with the lenses (L_2 and L_3) onto the CCD. The capture of the diffraction image is triggered by the

discriminator and a background image is subtracted from the image. The spatial frequencies in the diffraction image give information on the cross-section of the aerosol particles. The angular region is set by a spatial filter (SF) in the Fourier plane used for filtering out the direct light from the diode laser, and by the aperture of lens L_1.

3. Coupled-cavity model with Mie scattering

In the following we present a model describing the coupled-cavity diode laser using light scattering based on Mie theory for the detection and sizing of aerosol particles. The model characterizes the changes in the monitored output power as a function of the size of the particles by relating the extinction loss directly to the particle cross-sectional area. It is demonstrated that the changes in output power are essentially independent of refractive index of the aerosol particles.

Our model is an extension of the work presented in previous articles describing diode lasers subject to varying levels of external optical feedback [8–10]. The coupled cavity is considered equivalent to a solitary diode laser by replacing the inner facet reflectivity R_2, and the external plane mirror reflectivity $R_3 = kR_{ext}$ $(0 \le k \le 1)$, with an effective reflectivity R_e (see Fig. 1). The coupling coefficient k accounts for optical losses in coupling the reflected light back into the diode laser. The single-reflection approximation is used due to weak feedback from the external plane mirror. This yields an effective reflectivity of the coupled facet with no particle perturbations

$$R_e = R_2 + (1 - R_2)^2 R_3. \tag{1}$$

Particles introduced in the radiation field inside the coupled cavity create losses due to scattering and absorption. The diffracted light becomes essentially divergent and is not coupled back into the diode cavity, while the central refracted light undergoes a phase shift and, being incoherently coupled, is also lost. Thus, the particle perturbation is completely described by light extinction in the direction of propagation. In Mie scattering theory, optical extinction is represented by the extinction cross-section C_{ext}, which is the product of the extinction efficiency factor Q_{ext} and the aerosol particle cross-sectional area A_p [11]. The extinction efficiency factor is, especially for small particle sizes, an oscillating function of the ratio of particle radius to wavelength and of the index of refraction. Q_{ext} quickly converges to a value of 2 for particles larger than about 4λ. In the presence of a particle inside the coupled cavity the effective reflectivity is

$$R_p = R_2 + (1 - R_2)^2 \left(1 - \frac{Q_{ext} A_p}{A_b}\right)^2 R_3, \tag{2}$$

where the additional factor $(1 - Q_{ext} A_p / A_b)^2$ accounts for the particle-induced extinction loss, and A_b is the equivalent 'top hat' laser beam cross-sectional area inside the coupled cavity.

The output power of the equivalent solitary diode laser can be expressed as a linear function of the threshold current reduction $I - I_{th,e}$ and of the total loss [12,13]. This relation is still valid for the perturbing particle case provided that the effective reflectivity, R_p, and the threshold current associated with the perturbation, $I_{th,p}$, replace R_e and $I_{th,e}$ respectively. The output power emitted from the uncoupled facet of the laser is

$$P_p = \frac{\hbar \omega}{e} (I - I_{th,p}) \eta_i \frac{\ln(1/R_1)}{2\alpha_i L + \ln(1/R_1 R_p)}, \tag{3}$$

where $\hbar$ is Planck's constant, e is the electron charge, I is the operating current, and the cavity parameters are: ω the radiation frequency of the diode, η_i the internal quantum efficiency to account for spontaneous emissions and leakage currents, α_i the intrinsic loss per unit length due to material absorption and scattering inside the laser diode cavity, and L the diode cavity length.

We make a linear approximation for the threshold current change as a function of the variable effective reflectivity R_p,

$$I - I_{th,p} = (I - I_{th,e}) \frac{R_p - R_2}{R_e - R_2}. \tag{4}$$

In the unperturbed case, i.e. $R_p = R_e$, it follows from this relation that $I_{th,p} = I_{th,e}$, while if the particle is totally obstructing the beam, i.e. $R_p = R_2$, the operating current equals the threshold current $I = I_{th,p}$ and the system stops lasing.

The particle-induced extinction loss S is defined as the proportional reduction of the initial output

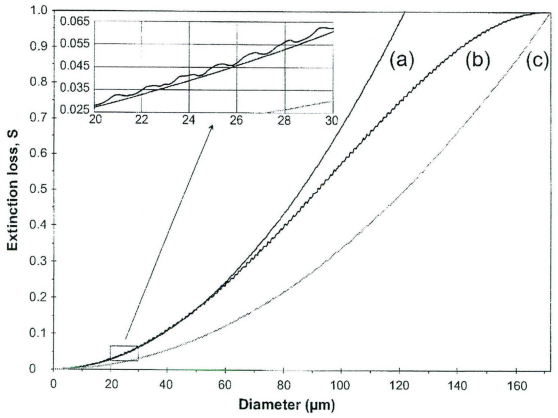

Fig. 2. The extinction loss vs. particle diameter. (a) Curve from the simple expression for the extinction loss (Eq. (6)). (b) Curve according to the complete coupled-cavity model (Eq. (5)). (c) Classical extinction curve. The insert is a magnification of the curves in the diameter range 20–30 μm.

power P_e, according to $S = (P_e - P_p)/P_e$. Substituting Eq. (3) and Eq. (4) into this expression yields

$$S = 1 - \frac{P_p}{P_e}$$

$$= 1 - \frac{(R_p - R_2)}{(R_e - R_2)} \frac{2\alpha_i L + \ln(1/R_1 R_e)}{2\alpha_i L + \ln(1/R_1 R_p)}. \qquad (5)$$

A plot of the extinction loss vs. particle diameter is shown in Fig. 2 (curve b) using the parameter values for the coupled cavity: $R_1 = 0.32$, $R_2 = 0.32$, $R_3 = 0.04$, $\alpha_i = 20\ \mathrm{cm}^{-1}$, $L = 300$ μm, $A_b = 0.048\ \mathrm{mm}^2$ and $\lambda = 780$ nm. Q_{ext} is calculated according to the routine in Ref. [11] by simulation of the Mie scattering theory for a homogeneous sphere with refractive index $n = 1.55$ and cross-sectional area $A_p = \pi r^2$. With these parameters the extinction loss reaches its maximum value for a particle diameter of about 170 μm.

A simple expression for the extinction loss can be derived from a few assumptions as to the physical properties of the aerosol particles. We first make the assumption that the particle cross-sectional area is much smaller than that of the beam, $A_p \ll A_b$. We then set the lower limit for particle size to 4λ, so that $Q_{ext} \approx 2$. The result is that

$$S \approx 2\frac{Q_{ext} A_p}{A_b} \approx 4\frac{A_p}{A_b}, \qquad (6)$$

which is also plotted in Fig. 2 (curve a) using the same parameter values as above. This simple expression for the extinction loss agrees well with the actual extinction loss for particle diameters up to about 70 μm, where the assumption $A_p \ll A_b$ is valid. In classical extinction, i.e. illuminating the particles outside a laser cavity, the extinction loss can be expressed as $S = Q_{ext} A_p/A_b \approx 2A_p/A_b$, see Fig. 2 (curve c). That is, comparing with Eq. (6), the coupled-cavity extinction loss is twice as large as in classical extinction for aerosol particles up to 70 μm. For larger particles the coupled-cavity extinction loss approaches the classical extinction loss. When $2A_p = A_b$, i.e. for a particle having a diameter of 170 μm, the classical and the coupled-cavity extinction loss have the same value.

The insert in Fig. 2 emphasizes that the oscillatory behavior of the extinction efficiency factor is reflected in the extinction loss variation. Calculations of the extinction efficiency factor with different refractive indices (ranging from 1.3 to 3.0) indicates that this oscillation sets the accuracy of the size measurements to ± 0.5 μm. Thus, the extinction process is essentially independent of refractive index and implies that correct size measurements can be performed on particles with unknown or varying refractive indices.

4. Experiments on aerosol particles

The instrument was used to measure individual nonabsorbing silica gel particles with irregular shapes and varying sizes, ranging from 15–40 μm (Merck Silica Gel 60, refractive index $n = 1.55$). The particle concentration was diluted in purified air, and the particles were aligned in a laminar airflow and passed through the sensing volume individually. The oscilloscope traces for particle sizes from 14–34 μm, triggered in real time, are shown together in Fig. 3 to demonstrate the effect of particle size on extinction losses. For validation, 14 diffraction images were used to estimate the size of the individual particles, and the results are plotted in Fig. 4 together with the theoretical curves given by Eq. (5) and Eq. (6). The error bars were defined as twice the standard deviation in the extinction loss. The deviations from the theoretical curves are explained by uncer-

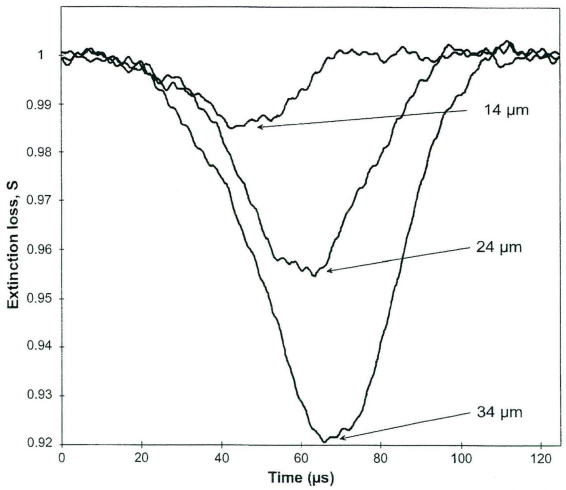

Fig. 3. Extinction losses from silica gel aerosol particles passing the sensing volume. The particle sizes are 14, 24 and 34 μm.

tainties of the size determination using the diffraction images. We use the measured extinction loss to calculate the distribution of 100 silica gel particles applying Eq. (5) of the coupled-cavity model, see Fig. 5. This is feasible when the particles are approximated as being spherical. According to the specifications, 90% of the particle sizes should be between 15–40 μm, which is in good agreement with our results. The current signal-to-noise ratio implies that the smallest detectable size is 4 μm. The size sensitivity of the instrument can be improved by reducing the laser beam diameter.

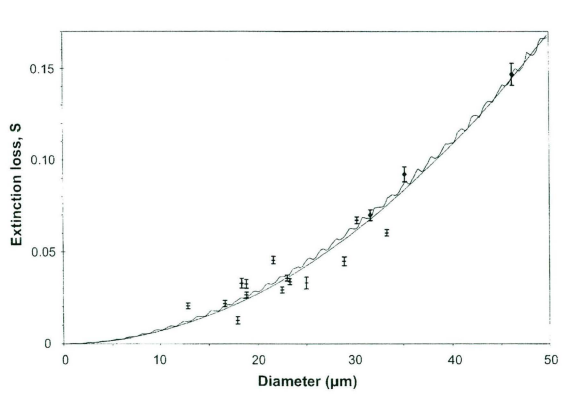

Fig. 4. Extinction loss from silica gel particles (—) and fibers (♦) together with theoretical curves (Eq. (5) and (6)). The error bars of the silica gel particles are set by the noise in the measured extinction loss, while the error bars for the fibers are equal to one standard deviation of five measurements.

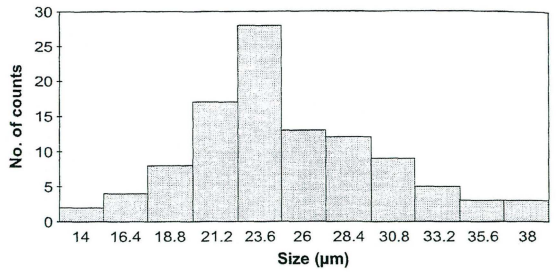

Fig. 5. Aerosol particle distribution obtained using the coupled-cavity model (Eq. (5)).

5. Experiments on fibers

We have also performed measurements on fibers with varying refractive indices, and evaluated the results with the model developed. Mie theory simulations applied on infinite cylindrical objects show that the cross-section of the fiber is governing the extinction loss. The fiber materials used were glass, carbon and kevlar®; the glass fibers were made by stretching melted sodium glass, while the kevlar and carbon fibers come from reinforcement materials used in surgery. The diameter of the fibers were measured with a calibrated microscope and detailed experiments were performed on three selected samples; a

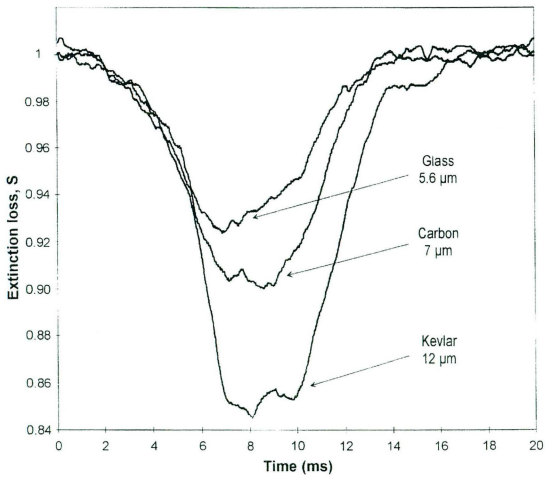

Fig. 6. Extinction loss measured for glass, carbon and kevlar fibers.

Table 1
Experimental and calculated data for the fiber measurements

Material	Microscope measured diameter (μm)	Optical equivalent diameter (μm)	Measured extinction loss, S	Calculated diameter (μm)
Glass	5.6 ± 0.1	31.6 ± 0.3	0.070 ± 0.003	5.5 ± 0.3
Carbon	7.0 ± 0.1	35.3 ± 0.3	0.092 ± 0.004	7.4 ± 0.4
Kevlar	12 ± 0.1	46.2 ± 0.2	0.147 ± 0.006	12.1 ± 0.5

Fiber measurements.

glass fiber with a diameter of 5.6 μm; a carbon fiber with a diameter of 7 μm and a kevlar fiber with a diameter of 12 μm. The experiments were performed by manually translating the fibers, which were 10 mm long and mounted in holders, through the sensing volume of the coupled cavity.

In Fig. 6 we present the single recordings of the time-resolved extinction losses from the three fibers. Scaling is needed in order to compare the resulting extinction losses with those obtained from spherical particles passing through the Gaussian beam. The diameter and length of the fiber are consequently

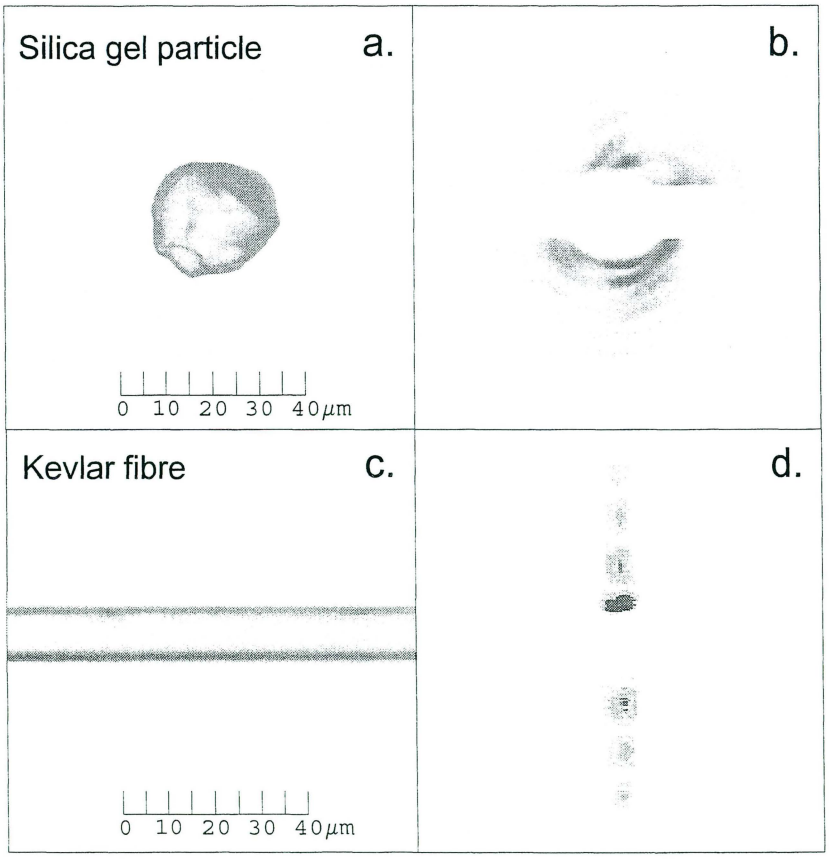

Fig. 7. (a) Microscope image of a silica gel particle with a diameter of 25 μm, and (b) corresponding experimental diffraction image of near-forward scattered light. (c) Microscope image of a kevlar fiber with a diameter of 12 μm, and (d) corresponding experimental diffraction image.

used to derive the diameter of an equivalent spherical particle which induces the same optical power extinction. Given an undisturbed optical power $P_i = I_0 A_b$ and an integrated power extinction P_s caused by a fiber, then an optical equivalent radius can be defined and calculated from the relation $P_s = I_0 \pi r^2$. The fiber extinction losses vs. the optical equivalent diameter are plotted together with the silica gel particles in Fig. 4. Experimental and calculated data from all the fiber measurements are summarized in Table 1. The optical equivalent diameter was calculated by scaling the microscope measured diameter, and the measured extinction loss was used to derive the calculated diameter.

The results show good agreement with this extension of the model to non-spherical particles. It is also verified that the extinction process is essentially independent of refractive index of the fiber material. Thus, correct size measurements can be performed on aerosol particles with unknown or varying refractive indices.

6. Identifying aerosol particles and fibers

Information on shape and orientation of the aerosol particle is obtained from the captured Fourier transformed diffraction image of near-forward scattered light. An aerosol particle inside the sensing volume forms a two-dimensional diffraction image determined by its shape. Irregularly shaped aerosol particles produce a more complex but specific image. These diffraction images can be used to identify the aerosol particle. Fig. 7 shows microscope images and corresponding Fourier transformed diffraction images of near-forward scattered light from a silica gel particle and a kevlar fiber inside the sensing volume. Image processing was done on the diffraction images to reduce the noise and enhance the contrast in the images. The central part of the diffraction images is obscured by the spatial filter (SF). The diffraction pattern of the silica gel particle has a concentric appearance thus indicating a spherical object. The kevlar fiber, which extends outside the sensing volume, produce mainly a one-dimensional diffraction image consisting of a series of light spots perpendicular to the fiber direction. Quantitative information about the relative proportions in the shape of a particle can be inferred by analyzing the position of diffraction light intensity minima.

7. Conclusions

We have presented an instrument based on a commercially available diode laser in a coupled-cavity configuration, that utilizes extinction loss and near-forward scattered light to detect and identify aerosol particles. The compact instrument combines single-particle sizing with shape analysis of the aerosol particles. The experimental results clearly show that aerosol particles and fibers induce extinction losses that increase with increasing diameter, in good agreement with the developed coupled-cavity model. It is demonstrated that the extinction loss is essentially independent of refractive index. Information on shape and orientation of the aerosol particle is obtained from the diffraction image of near-forward scattered light. The measurable size range of the aerosol particles is 4–170 μm with an accuracy of ±0.5 μm.

An optical trap [14] could be used for detailed investigation of the shape of a single aerosol particle by analyzing the diffraction images for different alignments in the sensing volume. The information obtained from these measurements can be used to compose a database of diffraction images for pattern recognition and automatic identification of various aerosol particles.

Acknowledgements

We wish to thank S. Svanberg, M. Bohgard, E. Swietlicki, J. Smith and H. Edner for support and many helpful discussions. This research was financed by the Swedish Research Council for Engineering Sciences (TFR), the Environmental Fund of the Swedish Association of Graduate Engineers (CF) and the Knut and Alice Wallenberg Foundation.

References

[1] L. Morawska, N.D. Bofinger, M. Maroni (Eds.), Indoor Air, Elsevier Science, Oxford, 1995.
[2] B.G. Schuster, R. Knollenberg, Appl. Opt. 11 (1972) 1515.

[3] J. Gebhart, D.J. Rader, T.J. O'Hern, P.A. Baron, M.K. Mazumder, Y.S. Cheng, in: K. Willeke, P.A. Baron (Eds.), Aerosol Measurement, Chapters 15–17, Van Nostrand Reinhold, New York, 1993.
[4] A. Macke, M.I. Mishchenko, K. Muinonen, B.E. Carlson, Opt. Lett. 20 (1995) 1934.
[5] OSLO, Optics Software for Layout and Optimization, Ver. 5.1, Sinclair Optics, 1996.
[6] M. Bottlinger, H. Umhauer, Appl. Opt. 30 (1991) 4732.
[7] J. Kitching, R. Boyd, A. Yariv, Opt. Lett. 19 (1994) 1331.
[8] R.P. Salathé, Appl. Phys. 20 (1979) 1.
[9] R. Lang, K. Kobayashi, IEEE J. Quantum Electron. QE-16 (1980) 347.
[10] J. Sigg, IEEE J. Quantum Electron. 29 (1993) 1262.
[11] C.F. Bohren, D.R. Huffman, Absorption and Scattering of Light by Small Particles, John Wiley and Sons, New York, 1983.
[12] K.J. Ebeling, Integrated Optoelectronics: Waveguide Optics, Springer-Verlag, 1993.
[13] D.M. Kane, A.P. Willis, Appl. Opt. 34 (1995) 4316–4325.
[14] A. Ashkin, J.M. Dziedzic, J.E. Bjorkholm, S. Chu, Opt. Lett. 11 (1986) 288.

II

Atomic spectroscopy with violet laser diodes

U. Gustafsson, J. Alnis, and S. Svanberg
Department of Physics, Lund Institute of Technology, P.O. Box 118, S-221 00 Lund, Sweden

(Received 28 June 1999; accepted 27 October 1999)

Laser spectroscopy with laser diodes can now also be performed in the violet/blue spectral region. A 5 mW commercially available CW laser diode operating at 404 nm was used to perform spectroscopy on potassium atoms with signal detection in absorption as well as fluorescence when operating on a potassium vapor cell and with optogalvanic detection on a potassium hollow cathode lamp. The $4s\,^2S_{1/2}-5p\,^2P_{3/2,1/2}$ transitions were observed at 404.5 and 404.8 nm, respectively. The laser diode was operated with a standard laser diode driver, and with or without an external cavity. The $4s\,^2S_{1/2}-4p\,^2P_{1/2}$ transition at 770.1 nm was also observed with a different laser diode. Here, Doppler-free saturated-absorption signals were also observed, enabling the evaluation of the ground-state hyperfine splitting of about 460 MHz. The data recorded allows an experimental verification of the theory for Doppler broadening, and thus of the gas kinetic theory. © *2000 American Association of Physics Teachers.*

I. INTRODUCTION

The development of narrow-band tunable lasers, in particular dye lasers, has allowed the emergence of powerful spectroscopic techniques for atomic and molecular spectroscopy.[1,2] The Doppler width of the transitions is normally of the order of 1 GHz and is much larger than the laser linewidth, allowing an easy study of the Doppler-broadened transitions. Using Doppler-free techniques, a resolution limited only by the natural radiative linewidth (typically a few MHz) can be obtained for narrow-band lasers. Much data on atomic structure including hyperfine splittings and isotopic shifts have been obtained through the years.

The development of single-mode near-IR (infrared) laser diodes made the techniques of laser spectroscopy accessible for student laboratories also. The most readily available experiment was to induce the $5s\,^2S_{1/2}-5p\,^2P_{3/2,1/2}$ transitions in rubidium atoms using easily available AlGaAs semiconductor lasers at 780.2 and 794.7 nm, respectively. Such experiments using free-running diode lasers on an atomic beam were described by Camparo and Klimac.[3] At our university, a laboratory session on rubidium laser diode spectroscopy has been offered for all physics students since 1990. Doppler-broadened transitions in an atomic vapor cell are observed, and by back-reflecting the laser diode beam, Doppler-free saturation signals are also recorded. We recently helped implement such experiments on isotopically enriched cells of ^{85}Rb and ^{87}Rb at four African universities, in Dakar (Senegal), Khartoum (Sudan), Nairobi (Kenya), and Cape Coast (Ghana) (see, e.g., Ref. 4). Laser diode spectroscopy for teaching purposes has also been demonstrated for Cs (852.3 nm)[5,6] and Li (671.0 nm).[7,8] Here, an improved laser performance (extended tuning range and narrow linewidth) was achieved by employing an external cavity including a Littrow grating.

The purpose of the present paper is to bring to the attention of the reader the fact that diode laser spectroscopy can now be extended to the violet/blue spectral region, due to the recent remarkable progress in GaN semiconductor lasers at Nichia Corporation by Nakamura and collaborators.[9,10] Blue diode laser spectroscopy is illustrated with experiments on the second resonance lines $4s\,^2S_{1/2}-5p\,^2P_{3/2,1/2}$ of potassium at 404.5 and 404.8 nm. For reference and comparison, the near-IR potassium line $4s\,^2S_{1/2}-4p\,^2P_{1/2}$ at 770.1 nm was induced with a different semiconductor laser. With the near-IR laser diode used it was not possible to observe the $4s\,^2S_{1/2}-4p\,^2P_{3/2}$ line at 766.7 nm.

Natural potassium consists of two isotopes, ^{39}K (93%) and ^{41}K (7%), both with a nuclear spin of $\frac{3}{2}$. Because of the dominance of ^{39}K we only need to consider this isotope. The structures of the near-IR and blue lines are given in Fig. 1, where the hyperfine structure splittings are obtained from Ref. 11. We note that, because of the small magnetic moment of the ^{39}K nucleus, the hyperfine structure splittings are small. The ground-state splitting is 462 MHz; for ^{41}K it is even smaller, 254 MHz. Thus, the Doppler-broadened line is not expected to show any structure, while a saturated absorption spectrum should be dominated by two peaks separated by about 460 MHz and broadened by upper-state unresolved hyperfine structure. Because of the fact that the excited state hyperfine structure is small and in the present context nonresolvable, while the ground-state splitting produces sharp separated peaks, it could be argued that potassium is pedagogically better suited than Li, Rb, and Cs for a student laboratory session at a particular level of atomic physics knowledge.

It is not our intention to record and evaluate high-resolution atomic spectra in the present work. Instead we would like to emphasize the use of free-running laser diodes and laser diode use in a simple feedback cavity, to demonstrate, evaluate, and experimentally verify the theory for Doppler broadening while also drawing attention to the phenomenon of hyperfine structure.

II. EXPERIMENTAL SETUP

The experimental arrangements employed in the present experiments are shown in Fig. 2. Direct absorption monitoring, laser-induced fluorescence, and optogalvanic detection are indicated. The violet semiconductor laser enabling the experiments on the $4s-5p$ transition was acquired from Nichia Corporation (Type NLHV500) and has a nominal wavelength at 25 °C of 404 nm and an output power of 5 mW. The near-IR $4s-4p$ transition was induced by a more conventional GaAlAs semiconductor laser (Mitsubishi ML4102) with a nominal wavelength of 772 nm and output power of 5

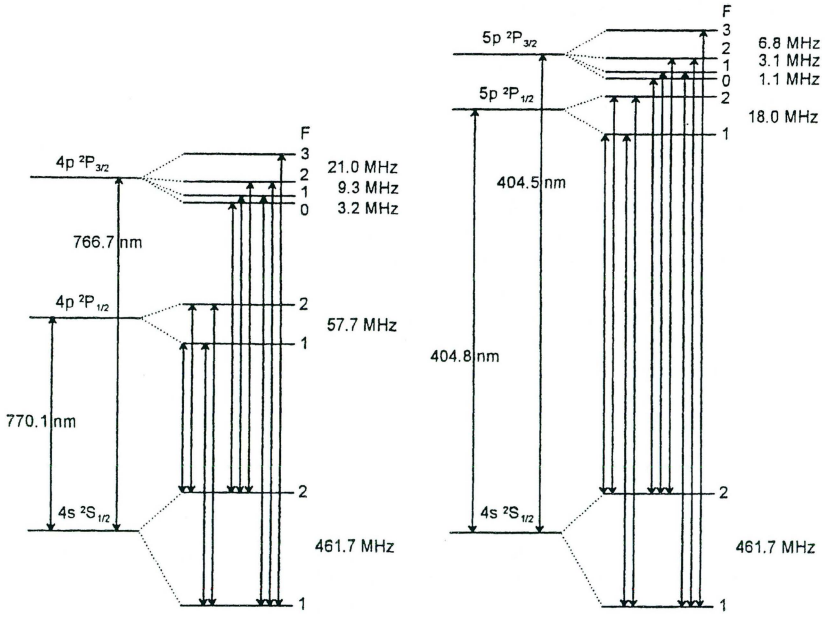

Fig. 1. Hyperfine structure diagrams of the $4s\,^2S_{1/2}-5p\,^2P_{3/2,1/2}$ and the $4s\,^2S_{1/2}-4p\,^2P_{3/2,1/2}$ transitions in ^{39}K. The energy splittings are not given to scale.

mW. The laser diodes were placed in a thermo-electrically cooled mount (Thorlabs TCLDM9) and operated with a low-noise laser diode driver (Melles Griot 06DLD103). Typically, the operating currents of the two laser diodes were set to 40 and 59 mA, respectively. Wavelength tuning of the laser diodes was accomplished by changing the temperature of the laser capsule. Once the temperature was set, a current ramp with a frequency of 100 mHz or 100 Hz was added to the operating current by means of a function generator (Tektronix FG504), allowing us to record the whole line profile in a single scan. The lower frequency was used for the optogalvanic detection while the higher frequency was used for the absorption and fluorescence measurements. In some of the experiments with the violet diode laser, a simple external feedback cavity with a Littrow grating was used to ensure single-mode operation, since the free-running laser typically lased on a few modes, separated by about 0.05 nm. External cavity laser arrangements are commercially available from several suppliers, e.g., New Focus, Newport, Thorlabs, and Tui Optics, and we used the Thorlabs system based on the laser diode mount, a piezo-electric mirror mount (KC1-PZ), a piezo-electric driver (MDT-690), and a 2400 l/mm grating (Edmund Scientific 43224). A molded glass aspheric lens (Geltech C230TM-A) was used to collimate the output beam from the diode laser. The 4 cm long potassium cell, which was prepared on a vacuum station by distilling a small amount of the metal into the cell after thorough bake-out at elevated temperatures, was placed in a small electrically heated oven. The oven had small windows for transmitting the laser beam and a larger window for observing laser-induced fluorescence.

The transmitted laser beam was focused on a detector (Hamamatsu S1223 pin photo-diode in a home-made transimpedance amplifier module) by an $f=50$ mm lens (Thorlabs BSX060-A). The detector output voltage was fed via a low noise amplifier (Stanford Research Systems SR560) to a signal averaging oscilloscope (Tektronix TDS520B). Finally, the recorded waveform could be transferred to a PC for processing and evaluation. A small part of the laser beam was split off by a beam splitter (neutral density filter) and sent to a low-finesse solid glass etalon with a free spectral range of 991 MHz in the near-IR region and 979 MHz in the violet. The generated fringes, which were detected by another detector, allow us to frequency calibrate each individual scan.

As an alternative detection method, the fluorescence induced by the violet transition could be monitored. The $4p-4s$ near-IR transitions, isolated by a Schott interference filter ($\lambda_{peak}=768$ nm), were used. By employing transitions from the $4p$ state, populated in cascade decays via the $5s$ and $3d$ states, instead of the direct decays on the violet $5p-4s$ transition, problems with background due to scattered light from cell windows and oven structures could be completely avoided. A photomultiplier tube (EMI 9558) was employed and the signal was fed via a current-to-voltage amplifier (Ithaco 1212) to the oscilloscope. We also tested a simple large-area photo-diode (Hamamatsu S-1226-8BK) for recording the fluorescence with quite satisfactory results.

The use of a hollow-cathode discharge lamp and optogalvanic detection is a further alternative for observing the blue potassium transitions. We used an Instrumentation Laboratory hollow-cathode lamp (Model 89227), intended for an atomic absorption spectrophotometer. A discharge current of 5 mA, also passing through a ballast resistor, was driven by an Oltronik photomultiplier supply (Model A2.5K-10HR), set for typically 300 V when the discharge was running. A rotating chopper (Stanford Research System SR540) was used for modulating the laser beam at 340 Hz, and the ac voltage across the ballast resistor occurring when atoms are excited was detected with a lock-in amplifier (EG&G 5209).

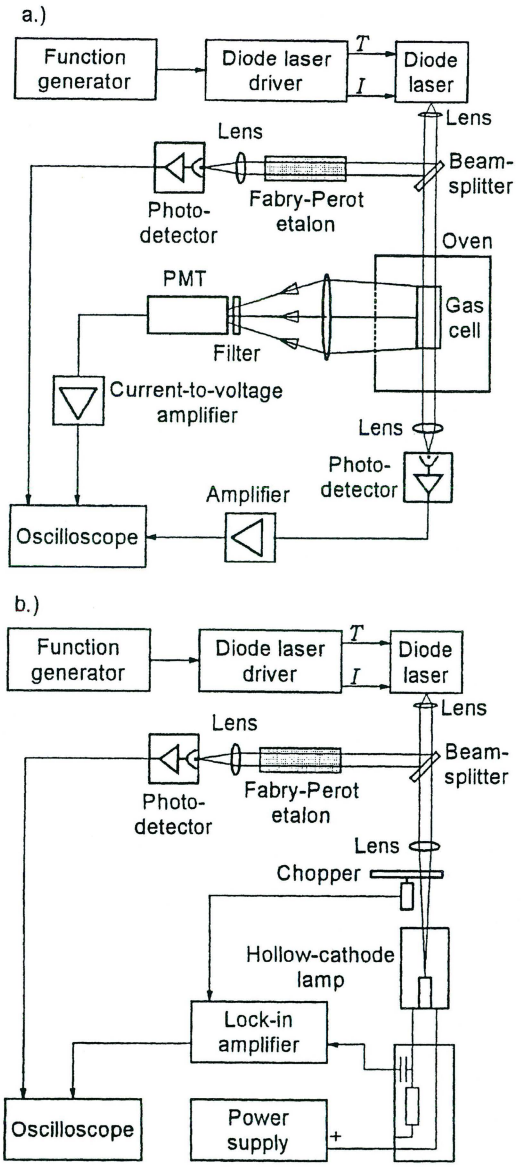

Fig. 2. Experimental setup for absorption, fluorescence (a) and optogalvanic spectroscopy (b) on potassium atoms.

III. MEASUREMENTS

The experimental setup was first tested by inducing the $4s\,^2S_{1/2}-4p\,^2P_{1/2}$ transition in the near-IR spectral region. This transition has, like the corresponding resonance lines in Rb and Cs,[3–8] high oscillator strengths, meaning a strong absorption already at atomic densities of $10^{15}/m^3$, corresponding to about 50 °C for potassium. Thus, the transitions are easily observable in absorption measurements. The near-IR transition was induced with the Mitsubishi laser operated without an external cavity. Raw data for a potassium absorption measurement are shown in Fig. 3, where the low-finesse Fabry–Perot fringes are also displayed. It can be noted that the laser output power increases during the scan,

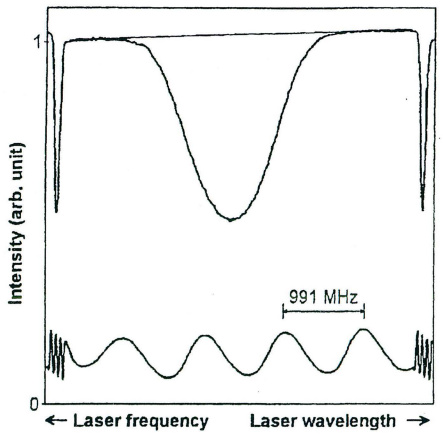

Fig. 3. Raw data obtained in an absorption recording of the $4s\,^2S_{1/2}-4p\,^2P_{1/2}$ potassium transition. Note the increasing laser output over the scan, but the quasi-linear frequency sweep as evidenced by equidistant Fabry–Perot fringes. The signals associated with the retrace at the end of the saw-tooth sweep are also evident.

but that the frequency sweep is quite linear. Thus, no frequency scale rectification was employed in our experiments, but the recorded curves were normalized the case of a constant laser output by dividing the recorded curve by a curve without atomic absorption. This procedure, like all subsequent data processing, was readily performed within the Microsoft EXCEL data package. The data shown in the rest of this paper are all preprocessed in this way. Typical normalized recordings for different vapor cell temperatures are shown in Fig. 4(a). By reflecting the laser beam back onto itself, saturated absorption signals with increased transmission are seen separated by about 460 MHz as displayed in Fig. 4(b). The excited state hyperfine structure is not resolved. In between the two signals a strong cross-over signal[1] is observed. In these measurements, performed with a beam size of about 1 mm×3 mm, care was exercised to avoid a direct feedback of the reflected beam into the diode laser which causes unstable oscillation. In the figure, an experimental curve recorded without beam reflection is superimposed, making an isolation of the nonlinear spectroscopic features easy.

Since the fluorescence is strong on the near-IR lines, the background due to scattering in cell windows, etc., is not severe, allowing the laser-induced fluorescence to be readily observed as shown in Fig. 5. Fitted curves, to be discussed later, are included in the figure. The lower trace shows the Doppler-free features due to the back-reflection of the beam into itself from the glass cell with normal-incidence windows.[12] The cross-over signal and one of the Doppler-free signals is clearly discernible. In the upper trace, we have misaligned the gas cell to only record the Doppler-broadened profile.

The $4s-5p$ violet transitions in potassium have much smaller oscillator strength than the near-IR transitions. Thus, considerably higher temperatures are needed on the cell to observe line absorption. In contrast, fluorescence detection, which in this case is background free, is already possible at temperatures as low as 30 °C. A transmission trace showing the violet line absorption on the $4s\,^2S_{1/2}-5p\,^2P_{3/2}$ transition is displayed in Fig. 6(a). This recording is performed with

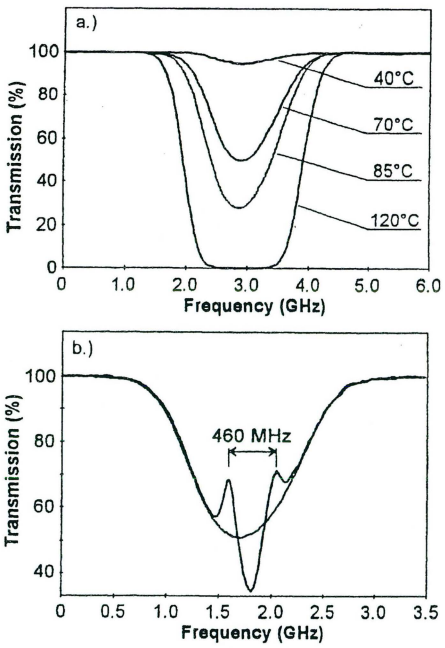

Fig. 4. Absorption recording on the $4s\ ^2S_{1/2}-4p\ ^2P_{1/2}$ potassium transition recorded for (a) different cell temperatures and (b) saturated absorption signal when the laser beam is reflected back on itself for a cell temperature of 70 °C.

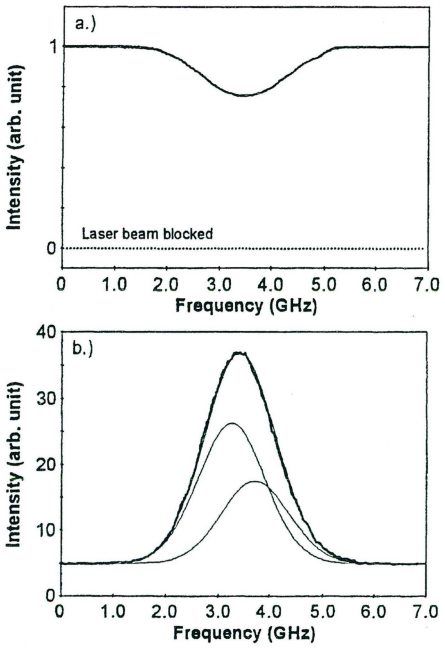

Fig. 6. Absorption (a) and fluorescence (b) recordings of the $4s\ ^2S_{1/2}-5p\ ^2P_{3/2}$ transition in potassium. The cell temperature was about 130 °C for the absorption recording and 70 °C for the fluorescence recording.

the violet laser operating in the external cavity. The $4s\ ^2S_{1/2}-5p\ ^2P_{1/2}$ transition was observed in a separate scan. For the weak violet transitions it is more difficult to reach strong saturation conditions and the Doppler-free signals were not observed in our experiments. A fluorescence recording of the same transition is shown in Fig. 6(b), together with fitted curves to be discussed later.

Optogalvanic detection[1,2] in a discharge relies on the fact that excited atoms are more easily ionized by electronic impact than ground-state atoms. Thus, when chopping the excitation beam, a corresponding ac component occurs in the discharge current at resonance. An optogalvanic lock-in recording of the $4s\ ^2S_{1/2}-5p\ ^2P_{3/2}$ transition is shown in Fig. 7. Here the violet laser was operated in free-run without using an external cavity. As mentioned above, the laser was then not running in a single longitudinal mode, as evidenced in separate tests using a high-resolution spectrometer. Laser output spectra without and with an external cavity are given in the insert of the figure. Note that for free atoms with isolated spectral features as in our case, the general spectral appearance is not influenced since only one of the oscillating modes interacts with the atoms. However, some broadening of the individual mode linewidth in multi-mode operation make spectral recordings less suited for line-shape studies such as those in the present experiments. For molecules with

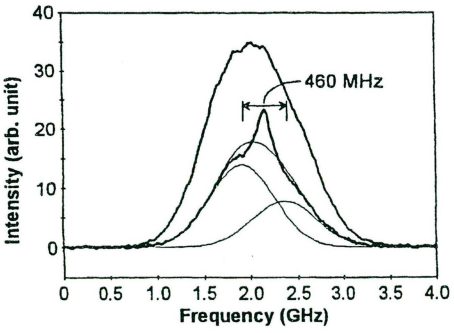

Fig. 5. Fluorescence recordings of the $4s\ ^2S_{1/2}-4p\ ^2P_{1/2}$ transition using a single laser beam, crossing a potassium vapor cell. The lower trace (magnified 4×) shows Doppler-free features by a back-reflection from the cell windows. The cell temperature was 40 °C for the lower trace and 60 °C for the upper trace.

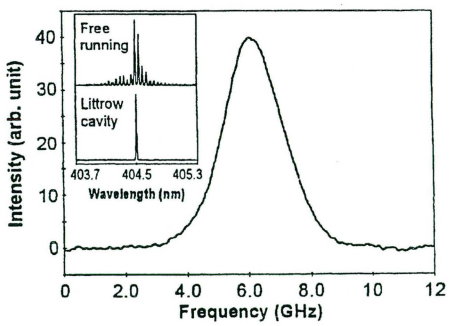

Fig. 7. Optogalvanic spectrum of the $4p\ ^2S_{1/2}-5p\ ^2P_{3/2}$ transition in potassium. The insert shows the laser diode output spectra when the laser diode is operating without and with an external cavity.

a multitude of close-lying lines, multi-mode behavior is, of course, unacceptable.

IV. DISCUSSION

Diode laser spectroscopy for the violet and near-IR $s-p$ transitions in potassium was demonstrated using simple equipment. Potassium has not previously been used in student laboratory work. With the very recent availability of violet semiconductor lasers, it became possible to directly excite, for the first time to our knowledge, a more highly excited state of an alkali atom with a laser diode. The outcome could then be compared with the results from experiments involving the first excited state, performed with the same simple setup.

The pedagogical value of a laboratory session along the lines discussed in this paper in part consists of running and scanning the diode lasers, and of adjusting the optical components and electronic devices for allowing the spectroscopic recordings, which could be demonstrated with three different detection methods. The other part is the atomic physics and gas kinetics contents. For this part, a useful approach is to record the near-IR $4s\,^2S_{1/2}-4p\,^2P$ transition in fluorescence and absorption for single and double laser beam passage through the cell. Since the upper-state hyperfine structure for the present purpose could be considered to be absent, the two Doppler-free peaks directly allow the ground-state splitting to be evaluated. The fluorescence line-shape $S(\nu)$ recorded for single-beam passage can then be fitted to a sum of two Gaussians with a half-width (FWHM) of $\Delta\nu$, separated by 460 MHz and having an intensity ratio of $A:B$,

$$S(\nu)=A\exp(-4\ln(2)(\nu/\Delta\nu)^2) + B\exp(-4\ln(2)((\nu+460)/\Delta\nu)^2). \quad (1)$$

The value for $\Delta\nu$ obtained is then compared with the theoretical value $\Delta\nu_D$:

$$\Delta\nu_D=\sqrt{\frac{(8\ln 2)RT}{c^2M}}\,\nu_0, \quad (2)$$

where ν_0 is the transition frequency at line center, R is the gas constant [8.3143 J/mol K], c is the speed of light, T is the cell temperature (in K), and M is the atomic mass number (39). The Doppler width for the near-IR transition is about 0.8 GHz for the temperatures discussed here (20 °C–120 °C).

With the violet laser a substantially broader fluorescence lineshape is then recorded and fitted to Eq. (1), and the Doppler width is extracted. Now the transition frequency is a factor of 1.90 higher and the violet theoretical Doppler width is correspondingly larger, typically 1.5 GHz using Eq. (2).

For both lines, good fits and experimental widths close to the calculated ones are obtained, e.g., the fits included in the fluorescence recordings in Figs. 5 and 6 yield 0.82 GHz (40 °C) and 1.55 GHz (70 °C), respectively, for the Doppler widths, to be compared with the theoretical values of 0.79 and 1.57 GHz, respectively. The good curve fits obtained using Gaussians and the experimental Doppler width values obtained in two widely separated wavelength ranges strongly support the theory for Doppler broadening, and thus the kinetic gas theory. A discussion of the velocity Maxwellian distribution and Doppler broadening can be found, e.g., on p. 67 of Ref. 1 and p. 86 of Ref. 2.

The ratio of the statistical weights of the two hyperfine ground state levels ($F=2$ and $F=1$) is 5:3, which is also the expected line intensity ratio (A/B) for transitions to an unresolved excited state. The experimentally deduced intensity ratios, 1.80 and 1.71, respectively, for the curves in Figs. 5 and 6 are close to the theoretical ratio, 1.67.

A further suitable violet transition for a student laboratory session is the aluminum 397 nm line. The $3p\,^2P_{1/2}-4s\,^2S_{1/2}$ transition at 396.2 nm for the single aluminum isotope ^{27}Al with a 1.26 GHz S-state hyperfine splitting allows very pedagogical optogalvanic recordings from an aluminum hollow-cathode lamp. A calcium hollow-cathode lamp run at a somewhat higher discharge current than normal produces Ca^+ ions with its potassium-like resonance transitions at 393.5 and 397.0 nm, respectively, which could be monitored by optogalvanic spectroscopy. An interesting pedagogical observation is, then, that the first excited state in potassium-like Ca^+ is located at about the same energy as the second excited state in potassium, due to the excess charge of the calcium nucleus.

V. CONCLUSION

We have performed laser diode spectroscopy in the near-IR and violet spectral region on potassium. The experiments demonstrate the possibility to perform simple and inexpensive laser spectroscopy on Doppler-broadened profiles of the same atom in different spectral regions, allowing the experimental verification of the theory for Doppler broadening and thus the gas kinetic theory.

ACKNOWLEDGMENTS

This work was supported by the Swedish Research Council for Engineering Sciences (TFR) and the Knut and Alice Wallenberg Foundation.

[1]W. Demtröder, *Laser Spectroscopy* (Springer Verlag, Heidelberg, 1996), 2nd ed.

[2]S. Svanberg, *Atomic and Molecular Spectroscopy—Basic Aspects and Practical Applications* (Springer Verlag, Heidelberg, 1997), 2nd ed.

[3]J. C. Camparo and C. M. Klimac, "Laser spectroscopy on a shoestring," Am. J. Phys. **51** (12), 1077–1081 (1983).

[4]S. Diop, "Utilisation des lasers a semi-conducteurs (AlGaAs) en spectroscopie d'absorption de saturation et de modulation de frequence dans le rubidium (^{85}Rb et ^{87}Rb)," Thesis for Maitre es Science, Universite Cheikh Anta Diop de Dakar, 1997.

[5]K. B. MacAdam, A. Steinbach, and C. Wieman, "A narrow-band tunable diode laser system with grating feedback, and a saturated absorption spectrometer for Cs and Rb," Am. J. Phys. **60** (12), 1098–1111 (1992).

[6]C. Wieman and L. Hollberg, "Using diode lasers for atomic physics," Rev. Sci. Instrum. **62** (1), 1–20 (1991).

[7]K. G. Libbrecht, R. A. Boyd, P. A. Willems, T. L. Gustavson, and D. K. Kim, "Teaching physics with 670 nm diode lasers—construction of stabilized lasers and lithium cells," Am. J. Phys. **63** (8), 729–737 (1995).

[8]L. Ricci, M. Weidemüller, T. Esslinger, A. Hemmerich, C. Zimmermann, V. Vuletic, W. König, and T. W. Hänsch, "A compact grating-stabilized diode laser system for atomic physics," Opt. Commun. **117** (5–6), 541–549 (1995).

[9]S. Nakamura and G. Fasol, *The Blue Laser Diodes* (Springer Verlag, Heidelberg, 1997).

[10]S. Nakamura and W. Kaenders, "Market-ready blue diodes excite spectroscopists," Laser Focus World **May 1999**, 69–75 ().

[11]E. Arimondo, M. Inguscio, and P. Violino, "Experimental determinations of the hyperfine structure in the alkali atoms," Rev. Mod. Phys. **49** (1), 31–75 (1977).

[12]T. P. Duffey, D. Kammen, A. L. Schawlow, S. Svanberg, H. R. Xia, G. G. Xiao, and G. Y. Yan, "Laser spectroscopy using beam overlap modulation," Opt. Lett. **10** (12), 597–599 (1986).

III

Frequency modulation spectroscopy with blue diode lasers

Ulf Gustafsson, Gabriel Somesfalean, Janis Alnis and Sune Svanberg

Department of Physics, Lund Institute of Technology,
P.O. Box 118, S-221 00 Lund, Sweden.

J. Alnis is also with the Institute of Atomic Physics and Spectroscopy,
University of Latvia, Rainis Blvd. 19, LV-1586 Riga, Latvia.

Abstract

Frequency-modulation spectroscopy provides ultra-sensitive absorption measurements. The technique is especially adapted to diode lasers which can easily be modulated and has been extensively used in the near-infrared and infrared spectral regions. With the recent availability of blue diode lasers, the accessible wavelength region can be increased. In the present paper we successfully demonstrate wavelength-modulation spectroscopy and two-tone frequency-modulation spectroscopy for the weak second resonance line of potassium at 404.8 nm and for the transition at 405.8 nm in lead, starting from the thermally populated $6p^2\ ^3P_2$ metastable level. Information regarding the modulation parameters is obtained using a fitting procedure. Experimental signal-to-noise ratios at different absorption levels are compared with theoretical signal-to-noise ratios and show good agreement. A detection sensitivity of 2×10^{-6} and 5×10^{-6} for wavelength and two-tone frequency modulation spectroscopy, respectively, in a 120-Hz bandwidth is demonstrated.

OCIS codes: 300.6260, 300.6380, 300.1030, 999.9999 (Blue diode laser)

1. Introduction

Diode laser absorption spectroscopy based on frequency modulation (FM) is a commonly used method for fast and ultra-sensitive detection of minute gas concentrations.[1-6] The interaction between a modulated laser field and an absorbing sample leads to the generation of an absorption related signal that can be detected at the applied modulation, at an overtone or at an intermediate frequency using frequency and phase-sensitive electronics. The characteristic of this process is to shift the detection band to a high-frequency region, where the laser excess (1/f) noise is avoided. Although a variety of FM methods have been implemented, they actually represent limiting cases of the same technique. Depending on the number of modulation tones, the choice of the modulation frequency relative to the spectral width of the absorbing feature, and the detection frequency, the different methods are referred to either as wavelength-modulation spectroscopy (WMS),[7] single-tone frequency-modulation spectroscopy (STFMS)[8] or two-tone frequency-modulation spectroscopy (TTFMS).[9]

In WMS the modulation frequency is much smaller than the half-width of the absorbing feature, while STFMS and TTFMS are characterised by modulation frequencies that are comparable or larger than the halfwidth of the absorbing feature. Usually, WMS is performed at kilohertz frequencies and a large modulation index using conventional lock-in amplifiers for signal detection. The sensitivity can be significantly improved applying megahertz modulation frequencies and harmonic detection at moderate modulation indices.[10-12] Since STFMS and TTFMS use high modulation frequencies, high sensitivity can be accomplished with a low modulation index.[10-12] STFMS applied on broad atmospheric pressure lines with linewidths of some gigahertz requires detection electronics with matching bandwidths. Such instruments are complicated, expensive and not always available in the wavelength region of interest. TTFMS circumvents this problem by using high-frequency modulation of the laser at two closely spaced frequencies, and detecting the signal at the difference frequency, often in the megahertz range. Thus, in TTFMS it is possible to use detection electronics of moderate bandwidths and still preserve high sensitivity at a low modulation index. The use of FM at high frequencies offers the possibility of quantum noise limited detection.[13-17]

Diode lasers are especially well suited for high-sensitivity absorption spectroscopy since their emission wavelength can both be tuned over the whole absorption profile by changing the temperature of the laser capsule, and their frequency can be modulated directly by applying an ac current on the drive current. Very recently, Nichia Corporation introduced blue cw GaN diode lasers emitting around 400 nm.[18] We have recently demonstrated their usefulness for spectroscopy by performing experiments on potassium vapour.[19] No attempts for sensitive detection were made in these experiments which employed direct absorption, laser-induced fluorescence and optogalvanic spectroscopy. In the present paper we extend this study using the blue diode laser and perform WMS and TTFMS on potassium

as well as on lead. We study the second resonance line 4s $^2S_{1/2}$ - 5p $^2P_{3/2}$ in potassium (^{39}K) at 404.8 nm. We also record the transition in lead (^{208}Pb) at 405.8 nm starting from the thermally very weakly populated $6p^2$ $^3P_2$ metastable level, situated 1.3 eV above the ground state. Absorption signals are measured at different temperatures and thus at different absorptions. By means of a fitting procedure information regarding the modulation parameters is obtained. We examine the possibilities of high-sensitive absorption measurements in this for diode lasers new and interesting wavelength region, and compare experimentally deduced and theoretically calculated signal-to-noise ratios (SNR:s). In order to achieve high sensitivity for both WMS and TTFMS, WMS is performed in the high-frequency wavelength modulation regime applying a modulation frequency of 5 MHz and detecting the second harmonic at 10 MHz, while TTFMS uses modulation frequencies around 900 MHz, i.e. larger than the Doppler widths (HWHM) which are less than 800 MHz for the transitions studied, and beat-signal detection at the same frequency as for WMS.

2. Experimental

A schematic of the set-up for WMS and TTFMS experiments is shown in Fig. 1. The blue diode laser (Nichia NLHV500) has a nominal wavelength of 404 nm at 25°C and a typical output power of 5 mW. The laser diode is placed in a thermo-electrically cooled mount and is current and temperature controlled by a precision diode laser driver (Melles Griot 06DLD103). The diverging laser beam is collimated by a moulded glass aspheric lens (Geltech C230TM-A), and is divided by a neutral

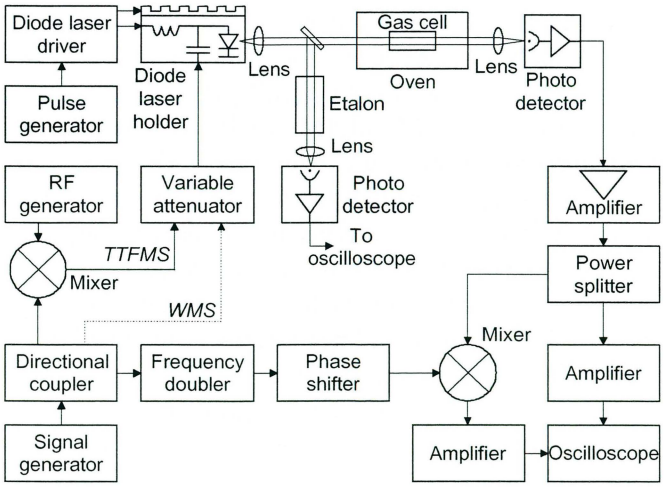

Fig. 1. Experimental set-up for direct absorption spectroscopy, WMS and TTFMS on potassium and lead vapour in sealed off cells.

density filter. One part of the beam is transmitted through a small electrically heated oven in which either a 4 cm long potassium cell or a 3.5 cm long lead cell is placed. The other part of the beam is directed through a low-finesse confocal Fabry-Perot etalon (free spectral range 1.5 GHz) for frequency calibration of the absorption spectrum. Both beams are focused on detectors which contain pin photodiodes (Hamamatsu S-1190) and a home-made transimpedance amplifier. Wavelength scanning is achieved by repetitively applying a rectangular current pulse (Tektronix RG501) with a duration of 1-2 ms and a repetition rate of 100 Hz to the diode laser drive current, which is biased below the threshold current. This ensures an almost constant frequency modulation index during the scan,[20,21] and also the possibility to simultaneously record the absorption line and the zero intensity level in direct absorption. The free-running laser typically lases on a few modes separated by about 0.05 nm, as evidenced in a separate test using a high-resolution spectrometer. However, a judicious choice of temperature and drive current ensures nearly single-mode operation.

The frequency modulation schemes for WMS and TTFMS are almost identical, the only difference being the generation of the modulation frequencies. In TTFMS, the two modulation frequencies are generated by mixing a 905 MHz signal (Wavetek 2510A) and a 5.35 MHz signal (Tektronix SG503) in a frequency mixer (Mini-Circuits ZFM-4H). For WMS only the 5.35 MHz modulation frequency is used. The modulation current, prior to superimposing it on the laser drive current, passes a variable attenuator, allowing the radio-frequency (rf) power to the diode laser to be varied. The TTFMS and WMS signals are detected by mixing (Mini-Circuits ZFM-3) the filtered and amplified (Mini-Circuits ZFL-1000LN) beat and second-harmonic signals (at 10.7 MHz) from the detector, with the frequency-doubled (Mini-Circuits FD-2) and appropriately phase-shifted (Synergy PP-921) 5.35 MHz signal. We adjust the rf power for highest possible WMS and TTFMS signal amplitudes without introducing any significant modulation broadening. One part of the detector signal is split off (Mini-Circuits ZFRSC-2050) before the frequency mixer in order to observe the direct absorption signal. Where appropriate, band-, high- and low-pass filters are inserted to prevent the modulation frequencies to reach the demodulation mixer, the detection frequency signal to reflect back towards the laser, and the modulated absorption related signals to influence the direct absorption signals. The direct and demodulated signals are amplified and low-pass filtered at 30 kHz in low-noise preamplifiers (Stanford SR560), and then averaged 256 times in a digital oscilloscope (Tektronix TDS520B). Thus, the effective bandwidth of the detection system is approximately 120 Hz. Finally, the recorded wave-forms are transferred to a computer for processing and evaluation.

In WMS it is possible to record both the absorption and the dispersion related to the probed medium. Here we only consider the absorption related signal by making a proper choice of the detection phase. This can be achieved since the in-phase (0 or π) component of the signal corresponds to pure absorption, while the

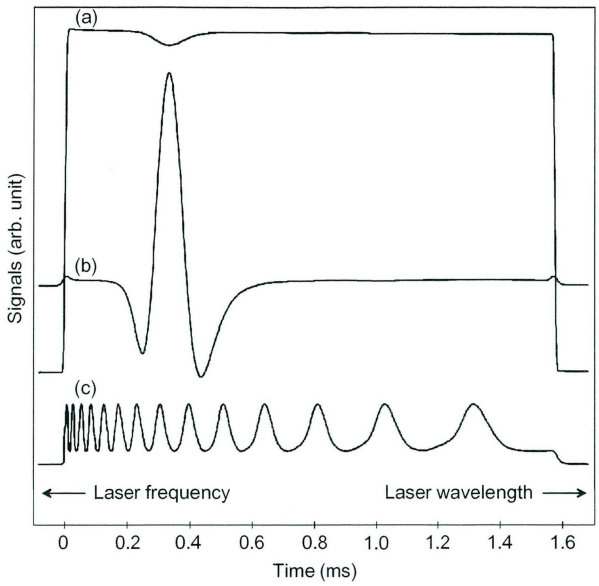

Fig. 2. (a) Direct absorption and (b) TTFMS spectra on the 4s $^2S_{1/2}$ - 5p $^2P_{3/2}$ line at 404.8 nm recorded with a rectangular current pulse. (c) Corresponding recording of the Fabry-Perot etalon fringes.

quadrature ($\pm\pi/2$) component corresponds to pure dispersion. In TTFMS a small part of the dispersion component will fall into the detection angle provided that the detection phase (around 0 or π) is adjusted for optimum signal amplitude.[22] However, for the transitions studied, the chosen modulation frequencies and the precision of the detection phase adjustment ($\pm$5%), the dispersion component is less than 0.1 % of the absorption component, and thus negligible.

3. Measurements

Natural potassium consists of two isotopes, ^{39}K (93%) and ^{41}K (7%), both with a nuclear spin of 3/2. The studied sealed-off potassium gas cell contains only the isotope ^{39}K. We note that the existence of a non-zero nuclear spin for potassium gives rise to a hyperfine splitting of the 4s $^2S_{1/2}$ - 5p $^2P_{3/2}$ transition. However, because of the small magnetic moment of the potassium nucleus the hyperfine splittings are small, for ^{39}K the ground-state splitting is only 462 MHz, and the upper-state splitting is around two orders of magnitude smaller.[23] Thus, the Doppler-broadened potassium line, with a halfwidth of around 800 MHz for the temperatures used here, is not expected to show any structure.

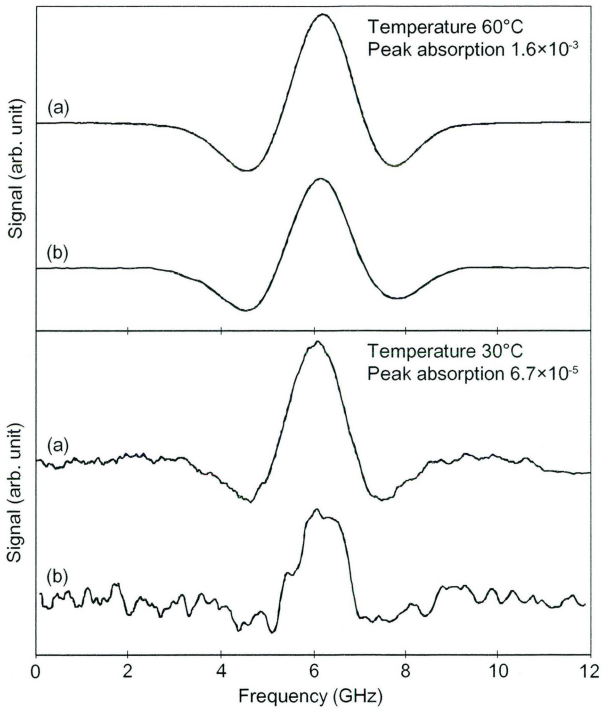

Fig. 3. Linearized (a) WMS and (b) TTFMS recordings for potassium at two different cell temperatures.

Typical recorded spectra for direct absorption and TTFMS measurements at 90°C in potassium are shown in Fig. 2, where the low finesse etalon fringes are also displayed. The WMS lineshape is almost identical to that of TTFMS and is not shown. Due to the use of a rectangular current pulse for wavelength scanning, the laser output power is almost constant during the scan, the zero intensity level can be seen in the direct absorption recording, and the frequency sweep is quite non-linear. This means that neither any laser output power rectification nor any separate zero intensity recording in direct absorption are necessary. It means, though, that linearization of the frequency scale has to be employed, and subsequently, this is done on all spectra shown in the rest of this paper.

WMS and TTFMS lineshapes for potassium vapour have been recorded from around 90°C down to room temperature. In Fig. 3, linearized recordings at 60°C and 30°C, corresponding to peak absorptions of 1.6×10^{-3} and 6.7×10^{-5}, respectively, are displayed. Interference fringes, caused by reflections between the neutral density filter and the detector surface, are clearly visible in the recording of the TTFMS lineshape at 30°C. Although FM spectroscopy offers the possibility of quantum noise limited detection, the minimum achievable sensitivity is in practice often set by

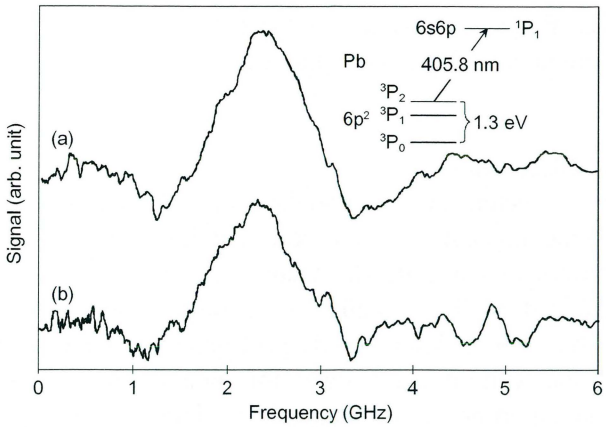

Fig. 4. Linearized (a) WMS and (b) TTFMS recordings on the lead 405.8 nm line. The insert show the lead structure diagram.

interference fringes, seen as a periodic oscillating background and originating from spurious reflections along the laser beam path. The interference effect can often be removed or highly reduced by careful angling of all transmissive optics, and as seen in the WMS recording in Fig. 3b, a slight adjustment of the neutral density filter removes the interference fringes.

Considerably higher temperatures are needed to observe the absorption in lead, due to the high vapour pressure of this metal. We study the transition at 405.8 nm starting from the thermally weakly populated $6p^2\ ^3P_2$ metastable level, situated 1.3 eV above the ground state. The lead experiments have been performed between 500°C and 700°C, corresponding to ground state atomic densities between 2×10^{17} m^{-3} and 7×10^{19} m^{-3} and Boltzman factors of 2×10^{-8} to 9×10^{-7}. This can be compared with the atomic density in the potassium cell that ranges from 3×10^{14} m^{-3} (20°C) to 3×10^{17} m^{-3} (90°C). The lead gas cell contains a natural mixture of lead isotopes, but the specific measurements are performed on the transition corresponding to the ^{208}Pb isotope with a nuclear spin of 0. The isotope, not having any hyperfine splitting because of the zero nuclear spin, has a Doppler width of around 550 MHz.

The linearized WMS and TTFMS recordings at 600°C (peak absorption 2.0×10^{-4}) are shown in Fig. 4. These recordings are also influenced by interference fringes which originate from a reflection between the detector surface back into the diode laser cavity. Despite cautious angling of all optics as well as the diode laser and the detector, we have not been able to completely suppress the interference fringes in the lead experiments. We explain the difference between the potassium and lead experiments by different diode laser behaviour at the two wavelengths due to different current and temperature settings. Another unwanted and limiting effect in the lead experiments is a diode laser mode jump close to the transition on the low

frequency side. The frequency position of the mode jump varies in time and this variation adds an irregular background to the recorded lineshapes.

4. Results and Discussion

In this section we first determine the modulation parameters in WMS and TTFMS by means of a fitting procedure of the recorded lineshapes. Then we use these modulation parameters to calculate the theoretical SNR:s and compare with the experimentally deduced SNR:s. Finally, we estimate the maximally achievable sensitivity of this blue diode laser based spectrometer. The evaluation is mainly performed using the experimental data for potassium, because, as noticed previously, the lead experiments are hampered by interference fringes and a diode laser mode jump. Thereby, the SNR is set by these effects rather than by the fundamental noise sources in an FM spectrometer. The formalism describing the FM theory, including calculations of TTFMS and WMS lineshapes and SNR:s can be found in, e.g. Refs. [22,24-26].

Frequency modulation of diode lasers is always accompanied by residual amplitude modulation (RAM), noticeable in the WMS and TTFMS recordings as a lineshape asymmetry. This RAM, accounted for in the FM theory by the AM index M and the AM-FM phase difference ψ, is due to that the laser intensity is not

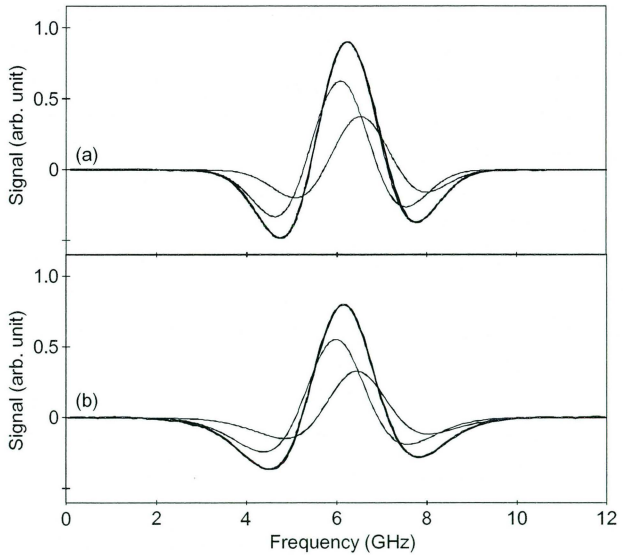

Fig. 5. Observed and calculated lineshapes for (a) WMS and (b) TTFMS on the potassium transition. The modulation parameters are $\beta = 230$ and $M = 0.045$ for WMS, and $\beta = 1.0$ and $M = 0.035$ for TTFMS.

exactly uniform over the FM range, and it is an undesirable effect because it carries some of the low-frequency noise into the FM signal. The AM index and the AM-FM phase difference are closely connected in theory and are difficult to determine independently. A value of $\psi = \pi/2$ for the AM-FM phase difference is generally considered to be a good approximation for diode lasers,[22,27,28] and in the following we adopt this value.

As mentioned previously, the studied transition in potassium actually consists of several hyperfine components. These can be divided mainly into two Gaussians with a halfwidth given by the Doppler width and separated by 462 MHz, having an intensity ratio of 5/3, equal to the statistical weights of the two hyperfine ground state levels (F = 2 and F = 1). The FM index, designated β in the FM nomenclature, and the AM index M are determined by fits to the WMS and TTFMS lineshapes recorded at different temperatures. The parameters obtained are $\beta = 230$ and $M = 0.045$ for WMS, and $\beta = 1.0$ and $M = 0.035$ for TTFMS. Using these parameter values, two calculated curves and their sum are displayed together with the experimentally recorded potassium line at 80°C in Fig. 5.

The AM to FM index ratio M/β is an intrinsic property of a diode laser and depends on the modulation frequency and the bias current.[29] Typically, the ratio scales with the modulation frequency, and for our experiments with equal bias current for WMS and TTFMS, the ratio of the AM to FM index ratio for TTFMS and WMS is 179, which is in excellent agreement with the ratio of the modulation frequencies, 181.

It can be observed in the experimental data that the signals (peak-to-peak value) in WMS are approximately 20% higher than those of TTFMS, see Fig. 3, 4 and 5. This agrees well with theoretically calculated signal values, that give a signal difference for the temperatures employed of about 21% for potassium, and 23% for lead. No modulation broadening is observed in either the WMS or the TTFMS lineshapes. This is consistent with the experimentally applied rf powers which we carefully adjust for highest possible signal amplitudes avoiding modulation broadening. Introducing modulation broadening makes the fitting procedure more difficult and inaccurate. WMS and TTFMS lineshapes, optimized only for maximum signal amplitudes show considerable modulation broadening.

In a frequency-modulated system the power SNR_P can be expressed as[25]

$$SNR_P = \frac{\langle i_s(t) \rangle^2}{i_{sn}^2 + i_{th}^2 + i_{RAM}^2 + i_{ex}^2} =$$

$$= \frac{\left(\frac{e\eta}{h\nu}\right)^2 2\langle P_0\rangle^2 |Q(\alpha,\varphi)|^2}{2\frac{e^2\eta}{h\nu}\langle P_0\rangle\left(1+\frac{M^2}{2}\right)^N \Delta f + \frac{4kT}{R_L}\Delta f + \left(\frac{e\eta}{h\nu}\right)^2 2R(M)\sigma_p^2 + \left(\frac{e\eta}{h\nu}\right)^2 \frac{\Delta f}{f^b}\sigma_{ex}^2} \quad (1)$$

where we keep the terms in the same order between the two expressions, and where the mean-square noise currents in the denominator are related to laser-induced detector shot noise, detector and amplifier thermal noise, amplitude modulation induced (RAM) noise, and laser source or excess noise, respectively, while the term in the numerator is the time-averaged mean-square detector current. The symbols in the equation are: e charge of the electron, η detector quantum efficiency, h Planck's constant, ν transition frequency, P_0 laser power, $Q(\alpha,\varphi)$ signal due to absorption α and dispersion φ, M AM index, N number of modulating tones, Δf detection bandwidth, k Boltzman's constant, T absolute temperature of the detector, R_L resistance of the detection system, $R(M)$ RAM function, σ_p standard deviation of the laser power within the noise equivalent bandwidth of the detector system, f detection frequency, and σ_{ex} system-dependent constant defined as the laser power fluctuations at 1-Hz bandwidth at 1-Hz frequency. The value of the exponent b is typically 1.0 but can range between 0.8 and 1.5.

The absorption and dispersion related lineshape function $Q(\alpha,\varphi)$, which depends on M, β and ψ, is calculated as the peak-to-peak value of the absorption component of the WMS and TTFMS lineshapes because the dispersion component vanishes by our choice of detection phase. The RAM function is the non-zero signal that is detected even in the absence of absorption, and is due to the amplitude modulation. The reason for employing second-harmonic detection instead of first-harmonic detection in WMS is to decrease the RAM influence. For WMS and second-harmonic detection $R(M) = ¼\, M^2 \cos(2\psi + \pi)$ and for TTFMS $R(M) = M^2$. The total power impinging on the detector is P_0 = 3 mW, and the parameters for detector and detection electronics in our set-up are η = 0.37 and R_L = 50 Ω. From direct absorption measurements, a value of $1\times10^{-3}\ P_0$ for the parameter σ_p has been deduced. The only adjustable parameter in the SNR calculations is σ_{ex}, and its value is estimated to be $4.5\times10^{-4}\ P_0$. These values of σ_p and σ_{ex} are approximately one order of magnitude higher than typical values for diode lasers used for frequency modulation in the NIR and IR.[10,14] We explain the difference by the multi-mode behaviour of our blue diode laser.

The experimental SNR is calculated as the ratio of the lineshape peak-to-peak value to the noise rms value, and as we in our experiments measure voltage and not power, the theoretical SNR is the voltage SNR_V, given by $SNR_V = (SNR_P)^{1/2}$. In Fig. 6, the experimental SNR:s for WMS and TTFMS are presented together with the theoretical SNR curves. Clearly, absorption signals less than the smallest

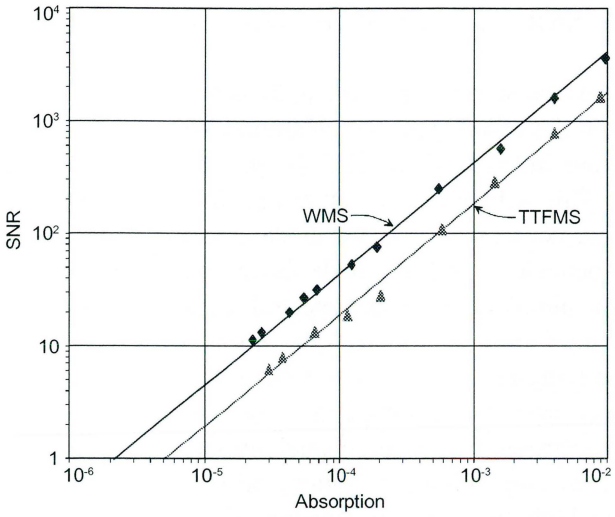

Fig. 6. Experimentally deduced SNR:s for WMS (◆) and TTFMS (▲) on potassium together with theoretical curves calculated using Eq. [1] and the parameter values mentioned in the text.

experimentally recorded absorption of 2×10^{-5} (at around 20°C) are detectable, but with our current set-up it is not possible to cool the gas cell and record signals below room temperature. The sensitivity limit that can be deduced is 2×10^{-6} for WMS and 5×10^{-6} for TTFMS. In the lead experiments, we have been able to record WMS and TTFMS signals down to a SNR of 1, which occur at temperatures around 500°C and correspond to an absorption of 5×10^{-5}. Thus, the interference fringes and the mode jump limit the detection sensitivity by about one order of magnitude.

There are two reasons for the approximately 2 times better SNR in WMS than in TTFMS. The first is the higher signal amplitude in WMS, and the second is the higher RAM noise level in TTFMS, as expected from the different RAM dependencies given by the RAM function. All other noise sources have the same amplitude in WMS and TTFMS. The ratio of the shot noise, the thermal noise, the laser excess noise, the TTFMS RAM noise, and the WMS RAM noise is 1: 1.7: 0.7: 5.4: 2.2, respectively. These figures clearly show that TTFMS is essentially limited by RAM noise, while the sensitivity in WMS is set both by RAM and thermal noise. We also note that the laser excess noise is below the shot-noise, and that the main purpose for employing frequency modulation is achieved. RAM noise and, as a consequence of the technique, laser excess noise can be highly reduced by the use of balanced homodyne detection.[13,15,21] However, the power transmitted through the absorbing medium is halved and the thermal noise is doubled in this technique. Theoretical calculations of the SNR:s in balanced homodyne detection, using the same parameter values as above, show that the SNR:s for TTFMS are almost the

same, while the SNR:s for WMS are lower, which we also have verified experimentally.

A possible extension of the present study is to monitor NO_2, which has strong absorption bands in the wavelength region around 400 nm. At atmospheric pressure these transitions are much broader than for potassium and lead, and might also partially overlap. This will require continous scans in the order of about 50 GHz, which at present are not feasible with the diode laser used. One should also note that the multi-mode behaviour of the diode laser does not influence the spectral appearance for free atoms with isolated spectral features like in our case, since only one of the oscillating modes interact with the atoms. However, for molecules with a multitude of close-lying lines multi-mode behaviour is, of course, unacceptable. As the blue diode laser used is a prototype laser, we believe that later versions will be better suited for spectroscopy, i.e. more single-mode. An external feed back cavity can be used to ensure single-mode operation and large frequency tuning ranges, but this will limit the high frequency modulation capabilities and thus the detection sensitivity.

5. Conclusions

We have performed FM spectroscopy on potassium and lead using a blue diode laser. The possibilities of high-sensitive absorption measurements in this for diode lasers new and interesting wavelength region are examined, employing WMS and TTFMS. In fits to experimental data the modulation parameters for the blue diode laser used in our experimental set-up are determined. It is shown that experimentally deduced SNR:s are in good agreement with theoretically calculated SNR:s. Additionally, the different noise sources are examined, and we conclude that TTFMS is dominated by RAM noise, while WMS is limited by both RAM and thermal noise. A minimum detectable absorption of 2×10^{-6} for WMS and 5×10^{-6} for TTFMS in a 120-Hz detection bandwidth is observed. By sum-frequency mixing blue and red diode lasers, even shorter emission wavelengths can be achieved, further extending the possibilities for sensitive absorption spectroscopy of many atomic and molecular transitions.[30]

This work was supported by the Swedish Research Council for Engineering Sciences (TFR) and the Knut and Alice Wallenberg Foundation. One of us (J. Alnis) would like to thank the Swedish Institute for a stipend supporting his stay in Sweden.

References

1. P. Werle, R. Mücke, F. D. Amato, and T. Lancia, "Near-infrared trace-gas sensor based on room-temperature diode lasers," Appl. Phys. B. **67**, 307-315 (1998).
2. G. Modugno, C. Corsi, M. Gabrysch, and M. Inguscio, "Detection of H_2S at ppm level using a telecommunication diode laser," Opt. Commun. **145**, 76-80 (1998).
3. H. Riris, C. B. Carlisle, D. F. McMillen, and D. E. Cooper, "Explosives detection with a frequency modulation spectrometer," Appl. Opt. **35**, 4694-4704 (1996).
4. J. A. Silver, D. J. Kane, and P. S. Greenberg, "Quantitative species measurements in microgravity flames with near-IR diode lasers," Appl. Opt. **34**, 2787-2801 (1995).
5. P. Kauranen, H. M. Hertz, and S. Svanberg, "Tomographic imaging of fluid flows by the use of two-tone frequency-modulation spectroscopy," Opt. Lett. **19**, 1489-1491 (1994).
6. P. Kauranen, I. Harwigsson, and B. Jönsson, "Relative vapor pressure measurements using a frequency-modulated tunable diode laser, a tool for water activity determination in solutions," J. Phys. Chem. **98**, 1411-1415 (1994).
7. E. G. Moses and C. L. Tang, "High sensitivity laser wavelength modulation spectroscopy," Opt. Lett. **1**, 115-117 (1977).
8. G. C. Bjorklund, "Frequency-modulation spectroscopy: a new method for measuring weak absorptions and dispersions," Opt. Lett. **5**, 15-17 (1980).
9. G. R. Janik, C. B. Carlisle, and T. F. Gallagher, "Two-tone frequency-modulation spectroscopy," J. Opt. Soc. Am. **B 3**, 1070-1074 (1986).
10. D. S. Bomse, A. C. Stanton, and J. A. Silver, "Frequency modulation and wavelength modulation spectroscopies: comparison of experimental methods using a lead-salt diode laser," Appl. Opt. **31**, 718-731 (1992).
11. F. S. Pavone and M. Inguscio, "Frequency- and wavelength-modulation spectroscopies: comparison of experimental methods using and AlGaAs diode laser," Appl. Phys. **B 56**, 118-122 (1993).
12. D. E. Cooper, R. U. Martinelli, C. B. Carlisle, H. Riris, D. B. Bour, and R. J. Menna, "Measurements of $^{12}CO_2$:$^{13}CO_2$ ratios for medical diagnostics with 1.6 μm distributed-feedback semiconductor diode lasers," Appl. Opt. **32**, 6727-6731 (1993).
13. G. Modugno, C. Corsi, M. Gabrysch, F. Marin, and M. Inguscio, "Fundamental noise sources in a high-sensitivity two-tone frequency modulation spectrometer and detection of CO_2 at 1.6 μm and 2 μm," Appl. Phys. **B 67**, 289-296 (1998).
14. C. B. Carlisle, D. E. Cooper, and H. Preier, "Quantum noise-limited FM spectroscopy with a lead-salt diode laser," Appl. Opt. **28**, 2567-2576 (1989).

15. C. B. Carlisle and D. E. Cooper, "Tunable-diode-laser frequency-modulation spectroscopy using balanced homodyne detection," Opt. Lett. **14**, 1306-1308 (1989).
16. P. Werle, F. Slemr, M. Gehrtz, and C. Bräuchle, "Quantum-limited FM-spectroscopy with a lead salt diode laser," Appl. Phys. B **49**, 99-108 (1989).
17. M. Gehrtz, G. C. Bjorklund, and E. A Whittaker, "Quantum-limited laser frequency-modulation spectroscopy," J. Opt. Soc. Am. B **2**, 1510-1526 (1985).
18. S. Nakamura and G. Fasol, *The Blue Laser Diodes* (Springer Verlag, Heidelberg 1997).
19. U. Gustafsson, J. Alnis, and S. Svanberg, "Atomic spectroscopy with violet laser diodes," Am. J. Phys., in press.
20. P. Kauranen and V. G. Avetisov, "Determination of absorption line parameters using two-tone frequency-modulation spectroscopy with diode lasers," Opt. Comm. **106**, 213-217 (1994).
21. V. G. Avetisov and P. Kauranen, "High-resolution absorption measurements using two-tone frequency-modulation spectroscopy with diode lasers," Appl. Opt. **36**, 4043-4054 (1997).
22. V. G. Avetisov and P. Kauranen, "Two-tone frequency-modulation spectroscopy for quantitative measurements of gaseous species: theoretical, numerical and experimental investigation of lineshapes," Appl. Opt. **35**, 4705-4723 (1996).
23. E. Arimondo, M. Inguscio, and P. Violino, " Experimental determinations of the hyperfine structure in the alkali atoms," Rev. Mod. Phys. **49** (1), 31-75 (1977).
24. D. E. Cooper and R. E. Warren, "Frequency modulation spectroscopy with lead-salt diode lasers: a comparison of single-tone and two-tone techniques," Appl. Opt. **26**, 3726-3732 (1987).
25. J. A. Silver, Frequency-modulation spectroscopy for trace species detection: theory and comparison among experimental methods," Appl. Opt. **31**, 707-717 (1992).
26. J. M. Supplee, E. A Whittaker, and W. Lenth, "Theoretical description of frequency modulation and wavelength modulation spectroscopy," Appl. Opt. **33**, 6294-6302 (1993).
27. W. Lenth, "High frequency heterodyne spectroscopy with current-modulated diode lasers," IEEE J. Quant. Electron. **QE-20**, 1045-1050 (1984).
28. S. Kobayasih, Y. Yamamoto, M. Ito and T. Kimura, "Direct frequency modulation in GaAlAs semiconductor lasers," IEEE J. Quant. Electron. **QE-18**, 582-595 (1984).
29. M. Osinski and J. Buus, "Linewidth broadening factors in semiconductor lasers: an overview," IEEE J. Quantum Electron. **QE-20**, 9-29 (1987).
30. J. Alnis, U. Gustafsson, G. Somesfalean, and S. Svanberg, "Blue diode laser in sum-frequency generation for mercury spectroscopy at 254 nm", Appl. Phys. Lett. 76, 1234-1236 (2000).

IV

Long-path monitoring of NO_2 with a 635 nm diode laser using frequency modulation spectroscopy

G. Somesfalean, J. Alnis*, U. Gustafsson, H. Edner and S. Svanberg
Department of Physics,
Lund Institute of Technology,
P.O. Box 118, S-221 00 Lund, Sweden

Abstract

In situ monitoring of traffic generated nitrogen dioxide emissions using long-path absorption spectroscopy is reported. A high sensitivity is achieved by employing two-tone frequency modulation spectroscopy at a visible absorption band of NO_2 using a tunable high-power diode laser operated around 635 nm. A real-time laser absorption spectrometer is accomplished by repetitively applying a rectangular current pulse to the diode laser DC drive current allowing detection of isolated NO_2 absorption lines. A detection limit of 10 $\mu g/m^3$ for NO_2 at atmospheric pressure with a 160 m absorption path is demonstrated. Continuous monitoring of NO_2 over a road intersection at peak traffic is performed.

1. Introduction

Nitrogen dioxide, NO_2, is an important agent in several atmospheric chemical cycles and is a common combustion-generated urban pollutant. There is a large interest in detection and precise measurement of this atmospheric trace gas, with many applications including air quality control, atmospheric chemistry, and traffic emission monitoring. Differential optical absorption spectroscopy (DOAS) [1,2] and light detection and ranging (LIDAR) [3,4] techniques are frequently used in optical environmental monitoring of NO_2, both methods normally requiring long absorption paths. To our knowledge, diode lasers have previously been used for NO_2 measurements only in connection with multiple-pass absorption cells, mostly at reduced pressures in order to minimize line broadening [5-10]. A disadvantage of using multiple-pass cells together with tunable diode lasers is that they usually introduce unwanted optical fringes due to etalon effects [5]. In our measurements long-path absorption is used instead, making remote sensing over several hundred meters possible in comparison to the point monitoring obtained in a multiple-pass absorption cell configuration. Thereby it is possible to obtain the concentrations in a large volume with less sensitivity to local fluctuations.

Until now, only a few investigations employing diode laser spectroscopy have been performed in gas monitoring using open-path configurations at atmospheric

pressure [11-14]. Field instruments for air pollution monitoring are preferably operated at ambient pressure, with the disadvantage of increased line broadening, reduced peak absorption and therefore lower detection sensitivity. The NO_2 spectrum is dense (~10 lines/cm^{-1}) and lines are partially overlapping at 1 atm due to pressure broadening. Another problem to be dealt with is interference from other molecular species, such as oxygen and water lines. The operating wavelength is therefore carefully chosen to be an isolated strong absorption line with sufficiently well resolved features that do not interfere with other species. At wavelengths longer than 350 nm, the absorption spectrum of NO_2 exhibits sharp spectral features [9]. NO_2 has strong absorption lines in the visible wavelength region. We use a diode laser emitting at a wavelength around 635 nm in order to probe the red wing of the $X\ ^2A_1 \rightarrow A\ ^2B_2$ visible absorption band of NO_2.

Previously a sensitivity of 0.2 μg/m^3 has been demonstrated using an optical cell at low pressure and monitoring with a cryogenically cooled diode laser operating around 6.2 μm [5]. Measurements using near IR [6] or red diode lasers [8, 9] have been performed with sensitivities of a few μg/m^3. The most common methods to enhance the sensitivity for small absorption measurements are to use balanced detection [8,9] or frequency modulation techniques [5,15-18].

In this work we reduce the noise bandwidth of the laser by employing a high-frequency modulation technique, namely two-tone frequency modulation spectroscopy (TTFMS) [19-21]. TTFMS using visible diode lasers is a convenient technique for trace gas detection in that it combines high-speed, high-precision, zero background, remote sensing capabilities and convenient access to wavelengths suitable for sensitive detection. However, modulation broadening is introduced at maximum sensitivity. At atmospheric pressure the absorption lines in NO_2 are broadened and the modulation frequency must be correspondingly high. The modulation amplitude applied to the diode must also be increased compared to low-pressure measurements. The resulting lineshapes resemble the second derivative, but are somewhat modified at atmospheric pressure because of overlapping lines.

2. Experimental

A schematic diagram of the experimental set-up is shown in Fig. 1, with the long-path absorption arrangement shown in the upper part and the TTFMS electronics in the lower part. The tunable high-power diode laser used was an InGaAsP index-guided device manufactured by Hitachi (HL6320G). It has a nominal wavelength of 635 nm at 25 °C and a typical output power of 10 mW. Wavelength stability is insured by controlling temperature and current of the laser diode with a precision diode laser driver (Melles Griot 06DLD103). The temperature of the diode laser capsule is stabilized to within 0.05°C over one hour of measurement. An antireflection-coated moulded glass aspheric lens (Geltech C240TM-B) collimates the laser output. A small mirror then directs the laser beam across a busy intersection about 5 m above the ground level until it hits a retro-reflector. The back reflected light is collected by a telescope with an aperture of 10 cm, and is focused onto the detector which contains a pin photodiode (Hamamatsu S-

1190) and a home-made transimpedance amplifier. The beam can also be sent through two reference cells containing known concentrations of NO_2 that are used for calibration purposes. The windows of the cells are tilted to the Brewster angle to avoid spurious optical feedback.

Spectral scanning is achieved by applying a rectangular current pulse with a duration of 1-2 ms and a repetition rate of 250 Hz to the diode laser drive current, which is biased below threshold. Thereby a longer wavelength scan is produced compared to a current ramp, and an almost constant frequency modulation index during the scan is ensured [20]. At the same time the sweep becomes highly non-linear, as can be seen on the signals from a low-finesse glass etalon (Fig. 2e) used for frequency calibration of the absorption spectrum. The tuning range produced is approximately 25 GHz, sufficient to capture a single atmospheric pressure-broadened transition of NO_2. A Burleigh WA-4500 wave meter is used to measure the laser frequency and to verify single-mode operation of the diode laser.

The two-tone frequency modulation set-up used here is described thoroughly in some previous articles of our group [15,16,20-22]. We have in this work used diode laser modulation at 935 and 925 MHz with a signal demodulation at 10 MHz. The demodulated signal is amplified and low-pass filtered in a low-noise preamplifier (Stanford SR560) which was set to 30 kHz, and subsequently averaged 256 times in a digital oscilloscope (Tektronix TDS520B), resulting in a total sampling time of 6 s. The TTFMS signal has a zero background, which is advantageous when the light intensity at the detector fluctuates due to atmospheric turbulence. The recorded waveforms are finally stored on floppy disks and transferred to a computer for post-processing and evaluation.

3. Measurements

Initially, measurements were performed to investigate the NO_2 absorption lines at different pressures. A reference cell was filled at 50 torr with a calibration gas containing 0.2% NO_2 in high purity synthetic air. A retro-reflector was placed at a few meters distance. Survey spectra in the visible wavelength region around 635 nm were used to identify isolated lines for sensitive measurement. A strong absorption feature was selected by temperature tuning the diode laser, and this wavelength was used for NO_2 monitoring. The valve of the cell was then opened and air was allowed slowly to enter. As the pressure increases, the absorption lines broaden with a corresponding decrease in the peak absorption. The TTFMS signal was maximized by significantly increasing the laser modulation index. At atmospheric pressure, the shape of the modulation signal is quite complex due to close-lying or overlapping absorption lines.

Atmospheric NO_2 measurements were performed using a round-trip path of 160 m. It is ensured that the absorption feature belongs to NO_2 by inserting a reference cell into the beam in front of the detector, as shown in Fig.1. The interference from oxygen or water lines can be easily avoided because these lines are not as dense as the NO_2 lines. The minimum detectable concentration is estimated using the reference cell containing NO_2 at atmospheric pressure. The peak-to-peak value of the recorded

TTFMS signal (Fig. 2b,c) is related to the absorption and also scales linearly with the power at the detector. The detection limit for the system corresponding to a signal-to-noise ratio S/N = 1 is found to be about 10 $\mu g/m^3$ in 160 m path and with a 256 times averaging. The main noise sources under monitoring conditions were the light intensity fluctuations, the detector noise and the residual optical interference. Using a long-path configuration we have not observed significant etalon fringes, which usually limit the minimum detectable absorption when short optical paths or multi-pass cells are employed.

Fig 3. shows the measured NO_2 concentration in air along the 160 m roundtrip path during consecutive measurements performed on two different occasions. The concentrations were acquired sequentially every minute. The wind strength and direction constitute important parameters because the measurements are performed 5 m above the pollution sources, i.e. the exhaust pipes of the passing cars. At the time of the measurements there were calm wind conditions. Two reference cells of the type discussed above, 30 and 5.6 cm long, respectively, were inserted into the beam for calibration (standard addition method). They contained 0.013% NO_2 at atmospheric pressure corresponding to an equivalent of 470 and 87 $\mu g/m^3$, respectively, of NO_2 uniformly spread over the 160 m path. We did not observe any direct increase of the signal after the passage of most of the individual cars because the beam passed too high above the exhaust pipes. However, at some occasions a high NO_2 emission was detected after the passage of some diesel trucks and buses.

4. Results and discussion

Comparison of the measured NO_2 sensitivity to other works shows that the detection limit is good, although the sensitivity is reduced due to smaller peak absorption at atmospheric pressure. The relatively high NO_2 concentrations are explained by the intense traffic during the measurements, averaging 70 vehicles in 5 minutes. Light intensity variations in the time range of several minutes appear to be caused mainly by thermal drifts in the optical alignment, because the optical power could be recovered by realignment. Longer absorption paths would be possible by using a better telescope in order to collect more light, thereby lowering the detection limit. Higher diode laser output powers are available at a wavelength of 670 nm. An additional advantage for operating at wavelengths near 670 nm is that interference with water absorption lines can be completely avoided [9]. Additionally, NO_2 presents larger absorption lines in the blue region and it is likely that the sensitivity could be further increased using blue diode lasers [22]. Unfortunately, presently available blue diode lasers typically operate on several modes, and are thus troublesome in spectroscopic measurements on molecules.

5. Conclusions

We have demonstrated the possibility to use diode laser based spectroscopic detection for long-path NO_2 concentration measurements in city air. The performance is comparable to that of a DOAS system where the wavelength region around 450 nm is scanned over tens of nanometers, thereby revealing larger absorption structures. In our case the TTFMS technique is used to increase the sensitivity for measurements of small absorption levels. The achieved detection sensitivity of 10 $\mu g/m^3$ in 160 m path at atmospheric pressure is lower than for low pressure NO_2 due to the decrease of peak absorption at atmospheric pressure.

In the present work the sensor is operated as a semi-portable device. Further development of this diode-laser-based trace gas detector into a compact, fully portable field instrument should find many applications in pollution monitoring measurements.

This work was supported by the Swedish Research Council for Engineering Sciences (TFR) and the Knut and Alice Wallenberg Foundation. One of us (JA) would like to thank the Swedish Institute for a stipend supporting his stay in Sweden.

References

1. U. Platt, "Differential optical absorption spectroscopy (DOAS)", in "Air Monitoring by Spectroscopic Techniques", ed. by M.W. Sigrist, Chemical Physics Series 127, p. 27 (John Wiley, New York 1994).
2. H. Edner, P. Ragnarson and S. Svanberg, "Differential optical absorption spectroscopy (DOAS) system for urban atmospheric pollution monitoring", Appl. Opt. **32**, 327 (1993).
3. K. A. Fredriksson and H. M. Hertz, "Evaluation of the DIAL technique for studies on NO_2 using a mobile lidar system", Appl. Opt. **23**, 1403 (1984).
4. H. Edner, P. Ragnarson, E. Wallinder, "Industrial emission control using lidar techniques", Environ. Sci. Technol. **29**, 330 (1995).
5. J. Reid, M. El-Sherbiny, B. K. Garside, and E. A. Ballik, "Sensitivity limits of a tunable diode laser spectrometer, with application to the detection of NO_2 at the 100-ppt level", Appl. Opt. **19**, 3349 (1980).
6. W. Lenth and M. Gehrtz, "Sensitive detection of NO_2 using high-frequency heterodyne spectroscopy with GaAlAs diode laser", Appl. Phys. Lett. **47**, 1263 (1985).
7. C. R. Webster, R. D. May, C. A. Trimble, R. G. Chave, and J. Kendall, "Aircraft (ER-2) laser infrared absorption spectrometer (ALIAS) for in-situ stratospheric measurements of HCl, N_2O, CH_4, NO_2, and HNO_3", Appl. Opt. **33**, 454 (1994).
8. M. G. Allen, K. L. Carleton, S. J. Davis, W. J. Kessler, C. E. Otis, D. A. Palombo, and D. M. Sonnenfroh, "Ultrasensitive dual-beam absorption and gain spectroscopy: applications for near-infrared and visible diode laser sensors", Appl. Opt. **34**, 3240 (1995).

9. D. M. Sonnenfroh and M. G. Allen, "Ultrasensitive, visible tunable diode laser detection of NO_2", Appl. Opt. **35**, 4053 (1996).
10. R. M. Mihalcea, D. S. Baer, R. K. Hanson, "Tunable diode-laser absorption measurements of NO_2 near 670 and 395 nm", Appl. Opt. **35**, 4059 (1996).
11. R. T. Ku, E. D. Hinkley, and J. O. Sample, "Long-path monitoring of atmospheric carbon monoxide with a tunable diode laser system", Appl. Opt. **14**, 854 (1975).
12. E. D. Hinkley, "Laser spectroscopic instrumentation and techniques: long-path monitoring by resonance absorption", Opt. and Quantum Electr. **8**, 155 (1976).
13. D. T. Cassidy and J. Reid, "Atmospheric pressure monitoring of trace gases using tunable diode lasers", Appl. Opt. **21**, 1185 (1982).
14. R. T. Menzies, C. R. Webster, E. D. Hinkley, "Balloon-borne diode laser absorption spectrometer for measurements of stratospheric trace species", Appl. Opt. **22**, 2655 (1983).
15. P. Kauranen, H. M. Hertz, and S. Svanberg, "Tomographic imaging of fluid flows by the use of two-tone frequency-modulation spectroscopy", Opt. Lett. **19**, 1489 (1994).
16. P. Kauranen, I. Harwigsson, and B. Jönsson, "Relative vapor pressure measurements using a frequency-modulated tunable diode laser, a tool for water activity determination in solutions", J. Phys. Chem. **98**, 1411 (1994).
17. H. Riris, C. L. Carslie, L. W. Carr, D. E. Cooper, R. U. Martinelli, and R. J. Menna, "Design of an open path near-infrared diode laser sensor: application to oxygen, water, and carbon dioxide vapor detection", Appl. Opt. **33**, 7059 (1994).
18. T. J. Johnson, F. G. Wienhold, J. P. Burrows, and G. W. Harris, "Frequency modulation spectroscopy at 1.3 μm using InGaAsP lasers: a prototype field instrument for atmospheric chemistry research", Appl. Opt. **30**, 407 (1991).
19. D. E. Cooper and T. F. Gallagher, "Double frequency modulation spectroscopy: high modulation frequency with low-bandwidth detectors", Appl. Opt. **24**, 1327 (1985).
20. V. G. Avetisov and P. Kauranen, "High-resolution absorption measurements using two-tone frequency modulation spectroscopy with diode lasers", Appl. Opt. **36**, 4043 (1997).
21. V. G. Avetisov and P. Kauranen, "Two-tone frequency-modulation spectroscopy for quantitative measurements of gaseous species: theoretical, numerical and experimental investigation of lineshapes", Appl. Opt. **35**, 4705 (1996).
22. U. Gustafsson, G. Somesfalean, J. Alnis and S. Svanberg, "Frequency modulation spectroscopy with blue diode lasers", submitted to Appl. Opt. (Oct. 1999).

* Permanent address: Institute of Atomic Physics and Spectroscopy, University of Latvia, Rainis Blvd. 19, LV-1586 Riga, Latvia

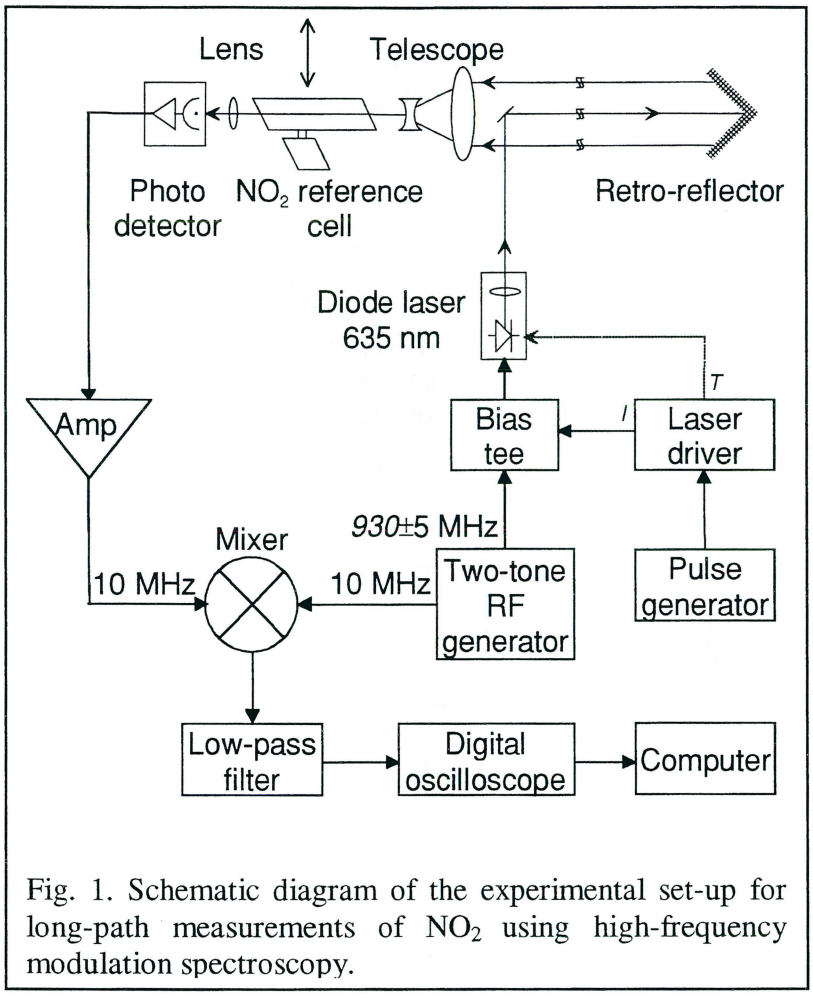

Fig. 1. Schematic diagram of the experimental set-up for long-path measurements of NO_2 using high-frequency modulation spectroscopy.

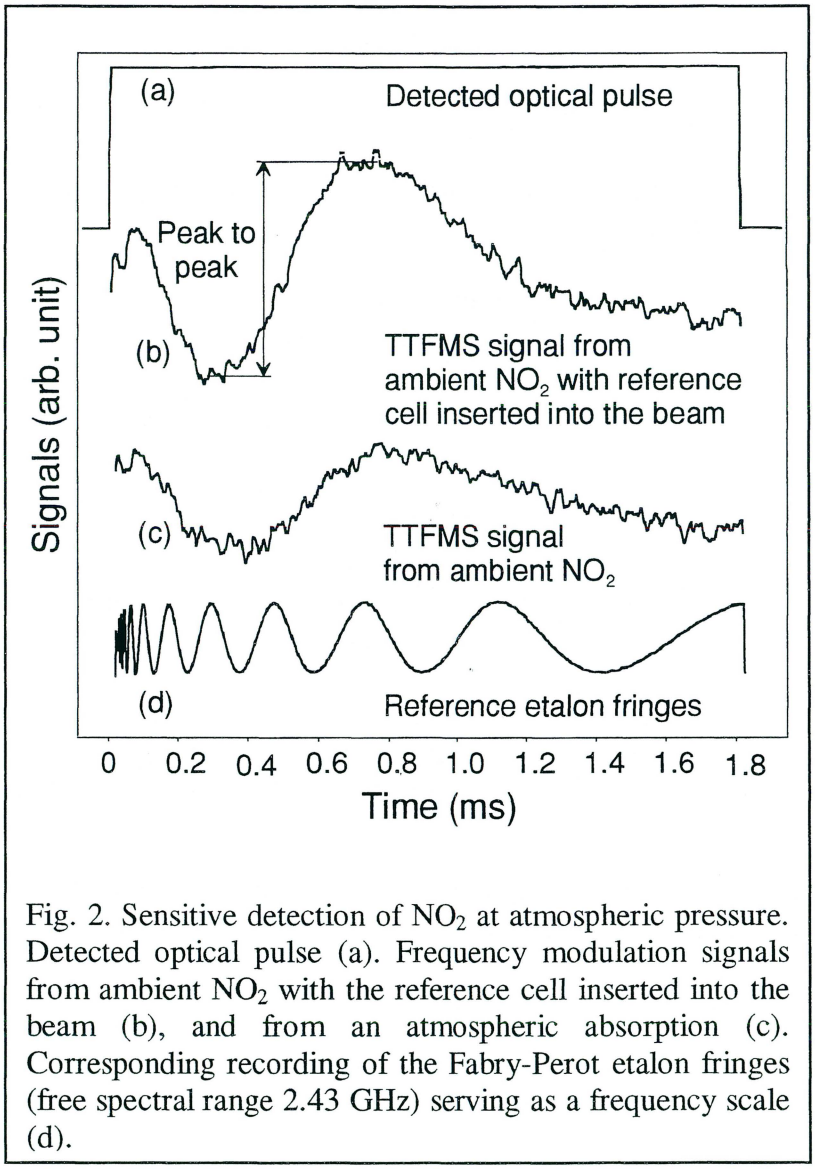

Fig. 2. Sensitive detection of NO_2 at atmospheric pressure. Detected optical pulse (a). Frequency modulation signals from ambient NO_2 with the reference cell inserted into the beam (b), and from an atmospheric absorption (c). Corresponding recording of the Fabry-Perot etalon fringes (free spectral range 2.43 GHz) serving as a frequency scale (d).

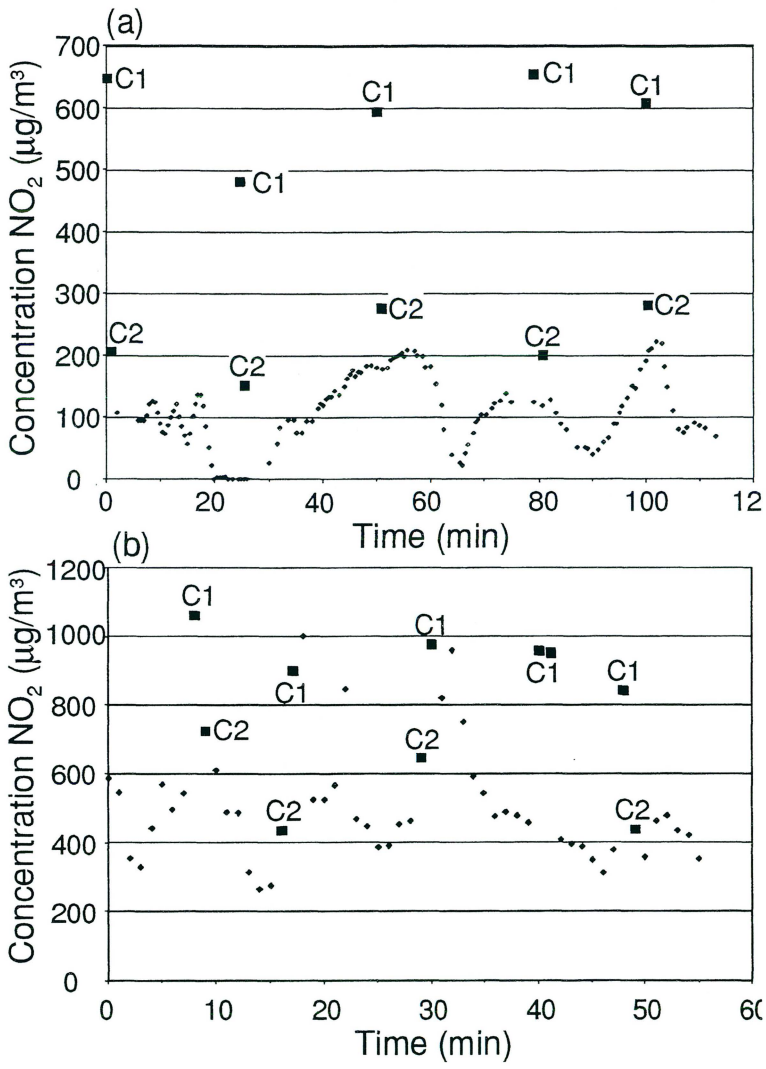

Fig. 3. Two data sets for the measured concentrations of NO_2 along a 160 m long path over a road intersection during winter hours of peak traffic. C1 and C2 mark two reference cells containing an equivalent of 470 µg/m^3 and 87 µg/m^3 of NO_2, respectively, inserted into the beam for calibration purposes.

V

Sum-frequency generation with a blue diode laser for mercury spectroscopy at 254 nm

J. Alnis,[a] U. Gustafsson, G. Somesfalean, and S. Svanberg,[b]
Department of Physics, Lund Institute of Technology, P.O. Box 118, S-221 00 Lund, Sweden

(Received 28 October 1999; accepted for publication 12 January 2000)

Blue diode lasers emitting 5 mW continuous-wave power around 400 nm have recently become available. We report on the use of a blue diode laser together with a 30 mW red diode laser for sum-frequency generation around 254 nm. The ultraviolet power is estimated to be 0.9 nW, and 35 GHz mode-hop-free tuning range is achieved. This is enough to perform high-resolution ultraviolet spectroscopy of mercury isotopes. The possibility to use frequency modulation in the ultraviolet is demonstrated; however, at present the ultraviolet power is too low to give advantages over direct absorption monitoring. Mercury detection at atmospheric pressure is also considered which is of great interest for environmental monitoring. © *2000 American Institute of Physics.* [S0003-6951(00)02810-2]

Absorption spectroscopy using diode lasers is a fast and sensitive method for detection of many gases in atmospheric monitoring.[1] The technique has been widely employed in the mid-infrared spectral region (2–15 μm), where numerous species of interest have fundamental vibrational absorption bands, and in the near-infrared region (0.6–2 μm), where weaker overtone and combination bands occur. Near-infrared spectroscopy makes extensive use of low-cost and room-temperature operated diode lasers which are readily available in this wavelength region. Atomic trace element detection in, e.g., a graphite furnace,[2,3] using diode-laser based absorption is an attractive possibility. Midinfrared absorption measurements apply cryogenically cooled lead-salt diode lasers or utilize difference-frequency generation in a nonlinear crystal pumped by two near-infrared diode lasers.[4] Many species also have strong electronic transitions in the ultraviolet (UV) spectral region (200–400 nm). These transitions are typically one or two orders of magnitude stronger than the mid-infrared transitions. Additionally, interference from water vapor is less significant in the UV spectral region.

Mercury (Hg) is the only pollutant present as a free atom in the lower atmosphere and has a strong transition at 253.7 nm that allows detection at low concentrations. Typical background concentrations of mercury in air are a few ng/m^3,[5] but much higher mercury concentrations exist around mercury mining areas and chloralcali plants.[6] Zeeman absorption,[7] differential optical absorption spectroscopy (DOAS)[8] or light detection and ranging (Lidar)[6] techniques are used for mercury measurements in air. A diode-laser-based spectrometer in the UV region could be especially interesting for low absorption measurements, since modulation techniques,[9,10] which give several orders higher sensitivity compared to direct absorption, can be easily employed.

The access to the UV spectral region employing diode lasers is usually provided by quadrupling[11–13] or sum-frequency generation.[14] The sum-frequency generation is generally conducted in two successive stages. The first stage is frequency doubling of a near-infrared diode laser output, and the second stage is mixing the second harmonic with another or the same near-infrared diode laser. The nonlinear conversion efficiency can be increased by mode locking an external-cavity laser based on a high-power tapered semiconductor amplifier.[11,12,14] A spectral linewidth of about 100 GHz is usually obtained, and that is typically 100 times larger than the required resolution for spectroscopic measurements. Another method to increase the conversion efficiency is to place the nonlinear crystal in an external buildup resonator.[13] This generates relatively high UV powers (~2 mW), but suffers from limited continuous tuning range and increased system complexity.

Very recently Nichia Corporation introduced blue diode lasers[15] and we have studied the possibility to use them for potassium and lead spectroscopy.[16,17] At present we report on the generation of UV radiation around 254 nm for mercury spectroscopy based on frequency mixing of a blue diode laser and a red diode laser.

The setup for sum-frequency generation is shown in Fig. 1. The blue diode laser (Nichia NLHV500 with a nominal wavelength of 404 nm at 25 °C and a free-running output power 5 mW) was operated in a Littrow-type cavity that ensured single-mode operation and less sensitivity to back reflections. We used a Thorlabs system based on a diode laser mount (TCLDM9), a piezoelectric mirror mound (KC1-PZ) and a 2400 1/mm grating (Edmund Scientific 43224).

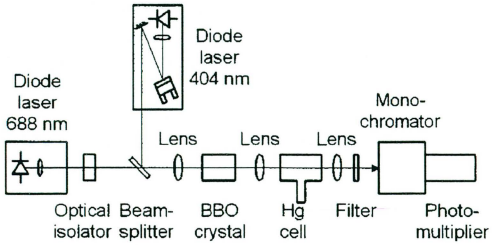

FIG. 1. Experimental setup for sum-frequency generation at 254 nm.

[a]Also with the Institute of Atomic Physics and Spectroscopy, University of Latvia, Rainis Blvd. 19, LV-1586 Riga, Latvia.
[b]Electronic mail: sune.svanberg@fysik.lth.se

The output power with the laser operated in the external cavity was 1 mW. The single-mode red diode laser (Toshiba TOLD 9150, 688 nm, 30 mW) was free-running and could be scanned continuously over 35 GHz by a current ramp. Moulded glass aspheric lenses with $f=4.5$ mm were used for collimation (Geltech C230TM). The diode lasers were temperature and current controlled using low-noise diode laser drivers (Melles Griot 06DLD 103). Both lasers were polarized vertically. An optical diode (OFR IO-5-NIR-I) was placed in the red diode laser beam to reduce backscattering from the nonlinear crystal. The blue and red beams were spatially overlapped via a dichroic beamsplitter and focused by a Nikon camera objective with a 50 mm focal length onto a 8-mm-long BBO crystal cut at $\theta=49°$ and $\varphi=90°$. Type I phase matching was achieved by tilting the crystal horizontally. A quartz lens of 50 mm focal length was used to collimate the UV light exiting the crystal. The detection side consisted of an $f=50$ mm quartz lens, a 254 ± 10 nm interference filter, a monochromator (Oriel 77250) tuned to 254 nm, and a photomultiplier (EMI 9558 QA). Without the monochromator a strong background existed from the not converted red and blue laser light. The signal from the photomultiplier was sent to a transimpedance amplifier (Itacho 1212) and a preamplifier (Stanford Research 560) and further to a signal averaging oscilloscope (Tektronix TDS520B).

It was not possible to measure the UV light power directly and we estimated it by photon counting. At optimized setup $n=5\times10^6$ pulses per second were counted. The quantum efficiency of the photomultiplier at $\lambda=254$ nm is $\eta=0.2$. That gives the UV power at the detector $P=nhc/(\lambda\eta)\approx2\times10^{-11}$ W. The two quartz lenses, the interference filter, and the monochromator had a transmission of 0.84, 0.28, and 0.09, respectively, thus the UV power after the crystal was about 0.9 nW.

From the theory of sum-frequency mixing of focused Gaussian beams and assuming a lossless crystal, the UV power can be expressed as[18,19]

$$P_3=\frac{4\omega_1\omega_2\omega_3 d_{\text{eff}}^3 P_1 P_2 l h}{\pi\epsilon_0 c^4 n_3^2}, \tag{1}$$

where ω_i are the angular frequencies ($\omega_1<\omega_2<\omega_3$), P_i are the powers, n_i are the refractive indices of the crystal, d_{eff} is the effective nonlinear coefficient, l is the crystal length, and h is a dimensionless focusing parameter. The effective nonlinear coefficient was calculated to $d_{\text{eff}}=1.59\times10^{-12}$ m/V according to the expressions in Ref. 20, and from the plots presented in Ref. 18 for the focusing parameter, we estimated $h=0.01$. Using the measured input powers (measured after the camera objective lens to $P_1=0.76$ mW and $P_2=25$ mW) and accounting for the approximately 7% reflection losses at the crystal input and output faces, we calculated a theoretically generated UV power $P_3=1.9$ nW. We believe that the approximately 2 times smaller UV power experimentally observed is due to imperfect overlap of the two input beams.

The spectrum of a natural isotopic mixture of mercury contains 5 peaks, that are formed by 10 Doppler-broadened transitions.[21,22] An absorption signal from a low pressure quartz cell containing a natural mixture of mercury is shown in Fig. 2(a). The spectrum was recorded by sweeping the red laser 35 GHz, and that resulted in an equally long scan in the UV. The mercury cell had a finger that was cooled by liquid nitrogen, because at room temperatures there was a 100% absorption on all the peaks. Absorption signals from two isotopically enriched low pressure cells with ^{204}Hg and ^{202}Hg are shown in Figs. 2(b) and 2(c), respectively. As a reference the designation and relative line strength of the isotope lines are displayed in Fig. 2(e).

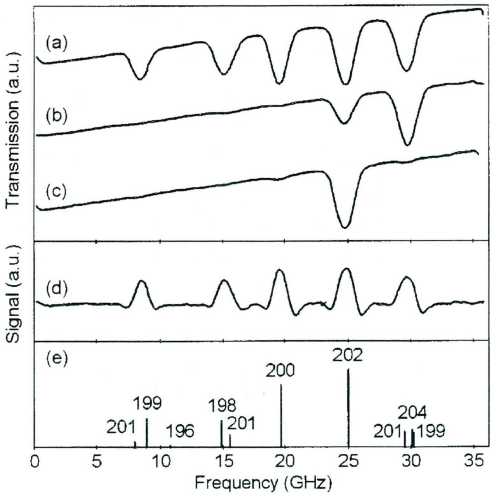

FIG. 2. Recorded UV absorption spectra from low pressure cells at −20 °C containing (a) natural isotope mixture of Hg, (b) enriched with ^{204}Hg, (c) enriched with ^{202}Hg, and (d) wavelength modulation signal from a natural isotope mixture of Hg. (e) Designation and relative strength of the Hg isotope lines according to Ref. 22.

The possibilities to use wavelength modulation in the UV region were also explored. A modulation frequency of 5 MHz was applied to the red diode laser through a bias tee. At the detection side the photomultiplier signal was amplified by a high frequency preamplifier and mixed with a frequency-doubled 5 MHz signal (standard radio-frequency components from Mini Circuits). The output from the mixer was low-pass filtered at 1 kHz, amplified and fed to the oscilloscope. Figure 2(d) shows the recorded second-harmonic ($2f$) signal. We also recorded low-frequency wavelength modulation signals at a few kilohertz frequency by modulating the external cavity grating angle with a piezo. Two-tone frequency-modulation signals with a setup used by our group extensively[17,23–27] were also recorded. Usually frequency modulation techniques have higher sensitivity compared to direct absorption, because the detection bandwidth is moved to higher frequencies, where laser excess ($1/f$) noise is very low, resulting in shot-noise limited measurements. At very low laser power though, as in our case, it is no advantage to use frequency modulation instead of direct detection.

At atmospheric pressures the isotope lines broaden and overlap to form a single absorption feature.[6,7] A scan of about 80 GHz is required to record the absorption at atmospheric pressures. Using our mode-hop-free scanning interval of 35 GHz we have measured the whole mercury absorption feature by recording three separate but overlapping scans. The recorded spectrum is shown in Fig. 3 together with a reference spectrum from a low-pressure cell. It can be

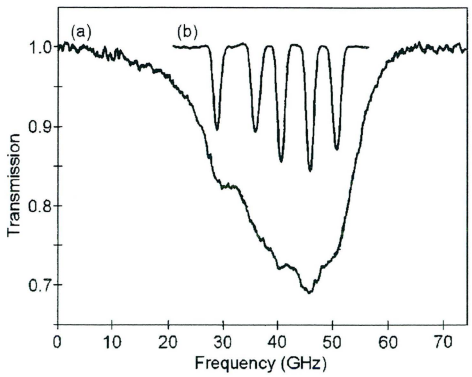

FIG. 3. (a) Hg absorption signal at atmospheric pressure in a 4 mm cell and (b) reference lines from a low pressure cell.

noted that since the isotope shifts are larger than the pressure-broadened linewidth (3.5 GHz obtained in a fit) individual isotope lines are clearly discernable in the recording at atmospheric pressure.

We have demonstrated the applicability of the recently available blue diode lasers for useful sum-frequency generation in the UV spectral region. High resolution absorption spectroscopy signals of mercury at 253.7 nm in a low pressure cell were recorded. Mercury detection at atmospheric pressure was performed, that is of great interest for trace element and environmental monitoring. The possibility to use different modulation techniques in the UV is demonstrated; however, at present the UV power is too low to give advantages over direct absorption monitoring. When higher UV powers become available through the fast development of diode lasers and nonlinear materials, the full power of our scheme combined with modulation techniques can be exploited.

This work was supported by the Swedish Research Council for Engineering Sciences (TFR) and the Knut and Alice Wallenberg Foundation. One of us (J.A.) would like to thank the Swedish Institute for a stipend supporting his stay in Sweden. The authors are grateful to A. Skudra for the loan of mercury isotope cells.

[1] H. I. Schiff, G. I. Mackay, and J. Bechara, in *Air Monitoring by Spectroscopic Techniques*, edited by M. W. Sigrist (Wiley, New York, 1994), pp. 239–333.
[2] P. Ljung and O. Axner, Spectrochim. Acta B **52**, 305 (1997).
[3] A. Zybin, C. Schnürer-Patschan, M. A. Bolshov, and K. Niemax, Trends Anal. Chem. **17**, 513 (1998).
[4] D. Richter, D. Glancaster, R. F. Curl, W. Neu, and F. K. Tittel, Appl. Phys. B: Lasers Opt. **67**, 347 (1998).
[5] S. H. Williston, J. Geophys. Res. **73**, 7051 (1961).
[6] H. Edner, G. W. Faris, A. Sunesson, and S. Svanberg, Appl. Opt. **28**, 921 (1989).
[7] J. Robbins, in *Geochemical Exploration*, edited by M. J. Jones (Institute of Mining and Metallurgy, London, 1973), p. 315.
[8] H. Edner, A. Sunesson, S. Svanberg, L. Unéus, and S. Wallin, Appl. Opt. **25**, 403 (1986).
[9] J. A. Silver, Appl. Opt. **31**, 707 (1992).
[10] D. S. Bomse, A. C. Stanton, and J. A. Silver, Appl. Opt. **31**, 718 (1992).
[11] L. Goldberg and D. A. V. Kliner, Opt. Lett. **20**, 1145 (1995).
[12] D. A. V. Klinter, J. P. Koplow, and L. Goldberg, Opt. Lett. **22**, 1418 (1997).
[13] C. Zimmerman, V. Vuletic, A. Hemmerich, and T. W. Hänsch, Appl. Phys. Lett. **66**, 2318 (1995).
[14] L. Goldberg and D. A. V. Kliner, Opt. Lett. **20**, 1640 (1995).
[15] S. Nakamura and G. Fasol, *The Blue Laser Diodes* (Springer, Heidelberg, 1997).
[16] U. Gustafsson, J. Alnis, and S. Svanberg, Am. J. Phys. (to be published).
[17] U. Gustafsson, G. Somesfalean, J. Alnis, and S. Svanberg (unpublished).
[18] G. D. Boyd and D. A. Kleinman, J. Appl. Phys. **39**, 3597 (1968).
[19] K. Sugiyama, J. Yoda, and T. Sakurai, Opt. Lett. **16**, 449 (1991).
[20] Y. X. Fan, R. C. Eckhardt, R. L. Byer, C. Chen, and A. D. Jiang, IEEE J. Quantum Electron. **QE-25**, 1196 (1989).
[21] W. Schweitzer, J. Opt. Soc. Am. **53**, 1055 (1963).
[22] R. Wallenstein and T. W. Hänsch, Opt. Commun. **14**, 353 (1975).
[23] P. Kauranen, H. M. Hertz, and S. Svanberg, Opt. Lett. **19**, 1489 (1994).
[24] P. Kauranen, I. Harwigsson, and B. Jönsson, J. Phys. Chem. **98**, 1411 (1994).
[25] P. Kauranen and V. G. Avetisov, Opt. Commun. **106**, 213 (1994).
[26] V. G. Avetisov and P. Kauranen, Appl. Opt. **35**, 4705 (1996).
[27] V. G. Avetisov and P. Kauranen, Appl. Opt. **36**, 4043 (1997).

VI

Simultaneous detection of methane, oxygen and water vapour utilising near-infrared diode lasers in conjunction with difference-frequency generation

Ulf Gustafsson, Jonas Sandsten, Sune Svanberg
Department of Physics, Lund Institute of Technology
P.O. Box 118, SE-221 00 Lund, Sweden
(Fax: +46 46 222 4250, e-mail: Sune.Svanberg@fysik.lth.se)

Abstract

An all-diode laser based spectrometer is used for the simultaneous detection of methane, oxygen and water vapour. This is accomplished using a 760 nm diode laser and a 980 nm diode laser in conjunction with difference-frequency generation to 3.4 μm in a periodically poled lithium niobate crystal. Each of the output wavelengths is resonant with one of the molecular species. Simultaneous recordings over a 15 m open path of laboratory air are demonstrated. The recording scheme shows the wide applicability of a diode-laser-based difference-frequency spectrometer for the detection of molecular species in different wavelength ranges. By increasing the frequency of the 980 nm diode laser and decreasing the frequency of the 760 nm diode laser, a maximum continuos tuning range in the mid-infrared of 3.6 cm^{-1} is achieved. This enables the recording of several methane lines at atmospheric pressure. Pressure dependence studies of methane lineshapes are also performed in an absorption cell. An indoor air methane background level of 3 ppm is measured. The signal-to-noise ratio in the recorded methane spectra indicate that sub-ppm detection of methane at atmospheric pressure is feasible.

PACS: 42.55.Px; 42.62.Fi; 42.65.Ky

Introduction

Laser absorption spectroscopy is a powerful technique for fast and sensitive detection of many gases in e.g. atmospheric monitoring, process control, and combustion diagnostics. The technique has been widely employed in the mid-infrared spectral region (2-15 μm), where numerous species of interest have strong fundamental vibrational absorption bands, and in the near-infrared region (0.6-2 μm), where weaker overtone and combination bands occur. Available laser sources in the mid-infrared region, e.g. lead-salt diode lasers, colour centre lasers, and CO or CO_2 lasers, each suffer from various practical drawbacks such as the need for cryogenic cooling, limited

tuning range, poor amplitude and frequency stability, large size, high cost or high power consumption. The promising and newly developed but not yet commercially available quantum-cascade lasers have been used in spectroscopic investigations in the infrared [1-3] but continuous-wave operation requires cryogenic cooling and rather high supply voltages. In the near-infrared region, on the other hand, diode laser technology offers several hundred milliwatts of narrow-band tuneable radiation at room temperature from small and low-cost devices. Using these near-infrared diode lasers and/or compact high-power diode-pumped solid-state lasers, great efforts have been made during the last years in developing difference-frequency generation (DFG) in non-linear materials for trace gas detection using the mid-infrared absorption bands [4-13].

All DFG implementations have so far only focused on the spectroscopic use of the generated mid-infrared radiation, disregarding the possibility of also using the generating laser wavelengths for probing the absorption bands in the near-infrared region. In the present study we explore simultaneous detection of atmospheric oxygen at 760 nm, water vapour at 980 nm and methane at 3.4 μm using near-infrared lasers in conjunction with difference-frequency mixing in a periodically poled lithium niobate (PPLN) crystal. Such simultaneous detection of interacting species is frequently of great interest, e.g. in connection with combustion. Certain important molecules, such as oxygen can be detected in the near-infrared region but do not have strong mid-infrared absorption.

Actually, a similar use of coincidences of excitation spectra occurring in sum-frequency mixing of pulsed dye laser radiation has been used to simultaneously induce fluorescence in the important flame species OH, NO and O (two-photon excitation) [14] and in HN_3, OH, and NO [15]. More cumbersome, simultaneous O_2, H_2O and temperature measurements have been performed by individually scanning three different near-infrared diode lasers [16], just as simultaneous flame fluorescence imaging of C_2 and OH could be achieved with independent laser systems [17]. Alternatively, simultaneous fluorescence detection of flame species can be achieved when absorption lines are inter-mingled in a certain spectral region, such as for OH, NH, CH and CN around 312.2 nm [18]. Similarly, in the mid-infrared region, where difference-frequency mixing has been used for absorption measurements, CH_4 and H_2O could be detected around 3.4 μm [8,11], CH_4 and H_2CO around 3.5 μm [10], CO_2 and N_2O around 4.4 μm [9], or CO and H_2O around 4.8 μm [12].

1 Experimental set-up

Our experimental set-up is schematically illustrated in Fig. 1. The two Fabry-Perot type diode lasers (Laser Components Specdilas F760 and Power Technology

LD1313), operating around 760 nm and 980 nm and having a maximum output power of 55 mW and 200 mW, respectively, are placed in thermoelectrically cooled mounts. Temperature and current are controlled by low-noise diode laser drivers (Melles Griot 06DLD103). Coarse wavelength tuning of the diode lasers is accomplished by changing the temperature around the diode laser capsules between 10°C and 40°C, resulting in a tuning range of about 5 nm for the 760 nm diode laser and of 8 nm for the 980 nm diode laser. Fine tuning is accomplished by changing the diode laser currents. Wavelength scanning is made by adding a 110-Hz current ramp (Hewlett-Packard 33120A) to the operating current of one or both of the two diode lasers.

The vertically polarised diode laser outputs are first collimated by anti-reflection coated moulded glass aspherical lenses (Geltech C230TM-B), and the elliptical beam profiles are then made circular by two anamorphic prism pairs (Melles Griot 06GPA004). The two collimated and circular beams are spatially overlapped in a dichroic beamsplitter (Melles Griot 88NPDC875) and focused by an 8.5-cm focal length achromatic lens into the PPLN crystal (Crystal Technologies 97-02355-01). The focusing into the crystal was simulated with a ray-tracing program (Sinclair Optics OSLO) to choose an optimal lens. The 19-mm long and 0.5-mm thick PPLN crystal without antireflection coating has 10 grating periods, each 1-mm wide, between 18.6 μm and 20.4 μm in 0.2 μm increments. A crystal oven (Super Optronics OTC-PPLN-20) ensures stable temperature of the PPLN crystal and fine tuning of the grating period for proper phasematching.

After the PPLN crystal, the two near-infrared beams and the generated mid-infrared beam are collimated by a 10-cm focal length CaF_2 lens, and then transmitted through approximately 15 m of laboratory air in a common open path. An anti-reflection coated germanium filter is used as a beamsplitter, to reflect the near-infrared radiation and transmit the mid-infrared radiation. A CaF_2 lens with a focal length of 10 cm focuses the mid-infrared beam onto a thermoelectrically cooled HgCdZnTe detector (Boston Electronics PDI-2TE-5) with an active area of 1 mm^2 and an immersed focusing lens. Combining an external focusing lens and a detector with an immersed lens simplifies the positioning of the small-area detector. A glass prism separates the two near-infrared wavelengths, and the intensities are detected by two pin photodiodes (Hamamatsu S-5821). The mid-infrared beam is in some of the experiments directed through a 10-cm long absorption cell with wedged CaF_2 windows for high-resolution measurements at low pressures and studies of pressure broadening.

The detected signals are amplified and low-pass filtered at 30 kHz in low-noise preamplifiers (Stanford SRS560) and viewed in real-time on two-channel digitising oscilloscopes (Tektronix TDS520B). The data are then transferred to a computer for processing and evaluation. A germanium etalon with a free spectral range of 0.05 cm^{-1} can be inserted in the mid-infrared beam for relative frequency calibration, and a glass

etalon with a free spectral range of 0.08 cm^{-1} can likewise be used for the near-infrared beams. A flip-in mirror is used to redirect the two diode laser beams to a wavemeter (Burleigh WA-4500) for precise measurements of the diode laser wavelengths at different temperature and current settings.

No optical diodes are used in the experiments. Instead, all optics are placed with a small angle to the laser beams to avoid optical feedback. Especially important is to angle (1 to 2 degrees is sufficient) the PPLN crystal, since placing it exactly perpendicular to the input beams resulted in severe optical feedback to both diode lasers. Another important factor is the immersed lens on the mid-infrared detector. Tests using a detector without an immersed lens, also showed significant instabilities in the output spectra of the two diode lasers. The tilting scheme probably means that we have a somewhat less than optimum conversion efficiency in the PPLN crystal due to a slight beam walk-off, but it also has the added benefit of reducing etalon effects, often encountered in infrared absorption experiments, to a minimum.

The simplest and most often used tuning method in the mid-infrared utilising difference-frequency generation is achieved by changing the wavelength of one pump laser, while the wavelength of the other pump laser is fixed. The tuning range in the mid-infrared is then limited by the maximum tuning range of only one laser. Alternatively, both pump lasers can be tuned synchronously, resulting in a very large tuning range in the mid-infrared. By temperature tuning of the two near-infrared diode lasers a theoretical mid-infrared tuning range of about 170 cm^{-1} is possible (from 2895 cm^{-1} to 3065 cm^{-1}). Due to the mode jump behaviour of all Fabry-Perot type diode lasers some regions will not be accessible. We have investigated some regions in this range, and once a region of interest was established by temperature tuning, we applied the finer and much faster current tuning. In the experiments we use both of the near-infrared diode lasers for molecular spectroscopy and therefore they are driven by current ramps. Depending on the relative scan directions a long or a short mid-infrared scan can be achieved. By increasing the frequency of the high-frequency diode laser (760 nm) with a negative current ramp and decreasing the frequency of the low-frequency diode laser (980 nm) with a positive current ramp, a maximum continuos tuning range in mid-infrared of 3.6 cm^{-1} has been achieved. A recording of the germanium-etalon fringes during such a scan is shown in Fig. 2. By changing scan directions, very short frequency scans are possible, and in principle, it is also possible to fix the mid-infrared frequency.

With near-infrared input powers of P_1 = 45 mW and P_2 = 195 mW at 760 nm and 980 nm, respectively, a maximum mid-infrared power of about 9 μW was generated. From the theory of difference-frequency mixing of focused Gaussian beams, the mid-infrared power can be expressed by [19]

$$P_3 = \frac{4\omega_3^2 d_{eff}^2 l}{\pi\varepsilon_0 c^3 n_1 n_2 n_3 (k_1^{-1} + k_2^{-1})} h(\frac{k_2}{k_1}, \frac{l}{b}) T P_1 P_2 \ , \qquad (1)$$

where

$$h(\mu, \xi) = \frac{1}{2\xi} \int_{-\xi}^{\xi} d\tau \int_{0}^{\xi} d\tau' \frac{1 + \tau\tau'}{(1 + \tau\tau')^2 + \left(\frac{1+\mu^2}{1-\mu^2}\right)^2 (\tau - \tau')^2} \ . \qquad (2)$$

Here n_i are the refractive indices of the PPLN crystal, P_i are the powers, k_i are the wave vectors, ω_i are the angular frequencies, $d_{eff} = (2/\pi)\times 27$ pm/V is the effective non-linear coefficient, l is the crystal length, b = 10 mm is the confocal parameter of the two mode-matched input beams, and T = 65 % accounts for the reflection losses at the crystal input and output facets. Inserting our experimental values, we calculate a theoretical mid-infrared power of P_3 = 11.8 µW. The deviation between measured and calculated mid-infrared powers can most likely be ascribed to our inclination of the PPLN crystal.

2 Spectroscopic studies

Studies of the absorption spectrum of methane were performed with the generated mid-infrared beam passing through the 10 cm absorption cell. Recordings of a methane line from the P-branch of the ν_3 band at 2927.075 cm^{-1} are shown in Fig. 3 for 3.5 mbar of pure methane in a total pressure of 5 mbar and then this methane concentration is successively diluted by air up to 800 mbar. In these recordings only the 760 nm diode laser was scanned. We observe a line broadening from 390 MHz to 2.4 GHz, corresponding to a pressure broadening coefficient of 2.6 MHz/mbar, in good agreement with previous results [20]. The laser system linewidth was estimated to 280 MHz with a CH_4 Doppler linewidth of 270 MHz and the observed lowest linewidth of 390 MHz. We note that a very good signal-to-noise ratio is achievable, allowing sensitive trace-gas detection at low pressures. At atmospheric pressure the lines broaden and overlap, and it is impossible to distinguish the weak transitions. In particular, at low pressures it is possible to observe the minor isotopic species $^{13}CH_4$ in the presence of the most abundant $^{12}CH_4$ isotope (mixing ratio 1:100) as illustrated in Fig. 4. The mixing ratio is not given directly by the observed intensity relation, since the studied lines do not originate from the same energy levels, but in principle, knowing the relative oscillator strength it is possible to deduce the exact mixing ratio.

After this demonstration of DFG spectroscopy we want to focus on the main theme of this work, namely the simultaneous detection of O_2, H_2O and CH_4. Simultaneous recordings of the three species are shown in Fig. 5 for the 15 meter open air pathlength in the laboratory, together with computed spectra from the HITRAN molecular spectroscopic database [20]. The figure shows the single O_2 A-band line, R7Q8, the single H_2O $5_{33} \leftarrow 6_{34}$ line in the $\nu_1+2\nu_2+\nu_3$ water band, and a portion of the CH_4 P-branch of the fundamental ν_3 methane band. By recording the whole oxygen and water profiles, and by scanning the frequency of the two diode lasers in opposite directions, a total frequency scan of 3.6 cm^{-1} is obtained in the mid-infrared. We choose to show 1.8 cm^{-1} of the scanned region where methane has prominent absorption lines. The relative humidity of the air was measured to 40% with a hygrometer, on the day of this recording. During our measurements the relative humidity was fairly constant, ranging from 35 % to 45 %. The normal O_2 concentration of 21% was measured. As expected, this O_2 concentration value does not change at all from one day to another. CH_4 has an outdoor background atmospheric abundance of 1.7 ppm, and a somewhat higher concentration in the indoor air is expected. From fits to experimental data, we have deduced that the typical methane background concentration in our laboratory is 3 ppm. This is almost twice as high as the typical outdoor concentration. With an observed signal-to-noise ratio of 20 in our recorded spectra at atmospheric pressure, we conclude that sensitivity in the 150 ppb range is achievable. We note that the atmospheric pressure methane experimental and theoretical curve show some deviations not present in the low-pressure short-pathlength data. We conclude that the deviations can then not be due to some spurious laser mode running. The residual non-methane spectrum is most likely due to a low concentration of some non-identified indoor environment hydrocarbon. We do not believe that the deviations are due to etalon fringes, since the structure is insensitive to small adjustments of the optical components, and fringes were ascertained to be absent in independent measurements.

As an example of recordings, relevant to e.g. the working environment, a 15 minute sequence of concentration determinations is shown in Fig. 6, exhibiting the response to the release of methane from a gas tank. The close-lying CH_4 transitions at 2928 cm^{-1} shown to the right in the spectral recordings of Fig. 5 were used. Raw data from recordings of the pressure-broadened single-peak feature are shown as inserts in the figure (0.9 sec. integration time). We note that the methane concentration is reduced to its background level after approximately 15 minutes. The structure occurring at 2 minutes was due to one of the authors walking around in the room inducing turbulent mixing.

3 Conclusions

We have used two near-infrared diode lasers and difference-frequency generation in a periodically pooled lithium niobate crystal for simultaneous detection of oxygen at 760 nm, water vapour at 980 nm, and methane at 3.4 μm. This is accomplished by probing each molecular species by the two near-infrared wavelengths and the generated mid-infrared wavelength, respectively. Recordings of atmospheric pressure broadened lines over a 15 m open path of laboratory air are demonstrated, and show the potential of the new measurement scheme for multispecies detection. Especially interesting is the possibility to simultaneous probe mid-infrared-absorbing molecular species and near-infrared-absorbing molecules without strong mid-infrared absorption. A continuos tuning range in the mid-infrared of 3.6 cm^{-1} is achieved by synchronously scanning the frequency of both near-infrared lasers. Isotopic species detection and pressure dependence studies of methane lineshapes were performed in an absorption cell. A typical indoor air methane background level of 3 ppm was reported, which as expected is higher than the typical outdoor level of 1.7 ppm. The signal-to-noise ratio in the recorded methane spectra indicates that sub-ppm detection of methane at atmospheric pressure is feasible over a measurement path of 10 meters and that practical multispecies detection can be performed over longer outdoor absorption paths.

Acknowledgements

The absorption wavelength relations for multispecies monitoring were pointed out by Dr. V.S. Avetisov. This work was supported by the Swedish Research Council for Engineering Sciences (TFR) and the Knut and Alice Wallenberg Foundation.

References

1. A.A. Kosterov, R.F. Curl, F.K. Tittel, G. Gmachl, F. Capasso, D.L. Sivco, J.N. Baillargeon, A.L. Hutchinson, A.Y. Cho: Opt. Lett. **24**, 1762 (1999)
2. S.W. Sharpe, J.F. Kelly, J.S. Hartman, C. Gmachl, F. Capasso, D.L. Sivco, J.N. Baillargeon, A. Y. Cho: Opt. Lett. **23**, 1396 (1998)
3. K. Namjou, S. Cai, E.A. Whittaker, J. Faist, C. Gmachl, F. Capasso, D.L. Sivco, A.Y. Cho: Opt. Lett. **23**, 219 (1998)
4. U. Simon, C.E. Miller, C.C. Bradley, R.G. Hulet, R.F. Curl, F.K. Tittel: Opt. Lett. **18**, 1062 (1993)
5. K.P. Petrov, L. Goldberg, W.K. Burns, R.F. Curl, F.K. Tittel: Opt. Lett. **21**, 86 (1996)
6. W. Schade, T. Blanke, U. Willer, C. Rempel: Appl. Phys. B **63**, 99 (1996)
7. B. Sumpf, T. Kelz, M. Nägele, and H.-D. Kronfeldt: Appl. Phys. B **64**, 521 (1997)
8. K.P. Petrov, S. Waltman, E.J. Dlugokencky, M. Arbore, M.M. Fejer, F.K. Tittel, L.W. Hollberg: Appl. Phys. B **64**, 567 (1997)
9. K.P. Petrov, R.F. Curl, F.K. Tittel: Appl. Phys. B **66**, 531 (1998)
10. D.G. Lancaster, D. Richter, R.F. Curl, F.K. Tittel: Appl. Phys. B **67** 339 (1998)
11. M. Seiter, D. Keller, M.W. Sigrist: Appl. Phys. B **67**, 351 (1998)
12. T. Kelz, A. Schumacher, M. Nägele, B. Sumpf, H.-D. Kronfeldt: J. Quant. Spectrosc. Radiat. Transfer **61**, 591 (1999)
13. D.G. Lancaster, D. Richter, R.F. Curl, F.K. Tittel, L. Goldberg, J. Koplow: Opt. Lett. **24**, 1744 (1999)
14. U. Westblom, M. Aldén: Appl. Opt. **28**, 2592 (1989)
15. U. Westblom, M. Aldén: Appl Spectr. **44**, 881 (1990)
16. D.S. Baer, R.K. Hanson, M.E. Newfield, N.K.J.M. Gopal: Opt. Lett. **19**, 1900 (1994)
17. M. Aldén, H. Edner, S. Svanberg: Appl. Phys. B **29**, 93 (1982)
18. B.J. Jefferies, R.A. Copeland, G.P. Smith, D.R. Crosley: *Twentyfirst International Symposium on Combustion* (The Combustion Institute, Pittsburg 1986) p.1709
19. T.-B. Chu and M. Broyer: J. Physique **46**, 523 (1985)
20. L. S. Rothman, C. P. Rinsland, A. Goldman, S. T. Massie, D. P. Edwards, J.-M. Flaud, A. Perrin, C. Camy-Peyret, V. Dana, J.-Y. Mandin, J. Schroeder, A. McCann, R. R. Gamache, R. B. Eattson, K. Yoshino, K. V. Chance, K. W. Jucks, L. R. Brown, V. Nemtchinov, P. Varanasi: "The HITRAN molecular spectroscopic database and HAWKS (HITRAN Atmospheric Workstation): 1996 edition, J. Quant. Spectrosc. Radiat. Transfer **60**, 665-710 (1998).

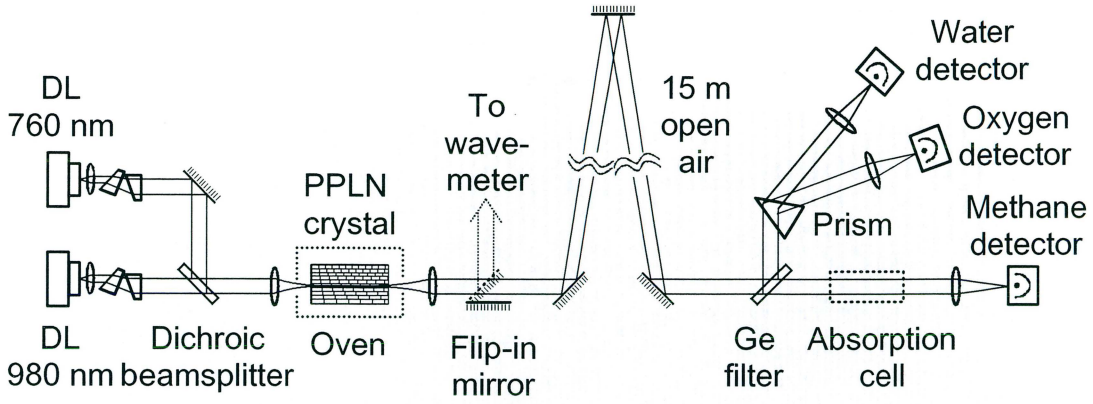

Figure 1. Experimental set-up for simultaneous ambient air monitoring of O_2, H_2O and CH_4.

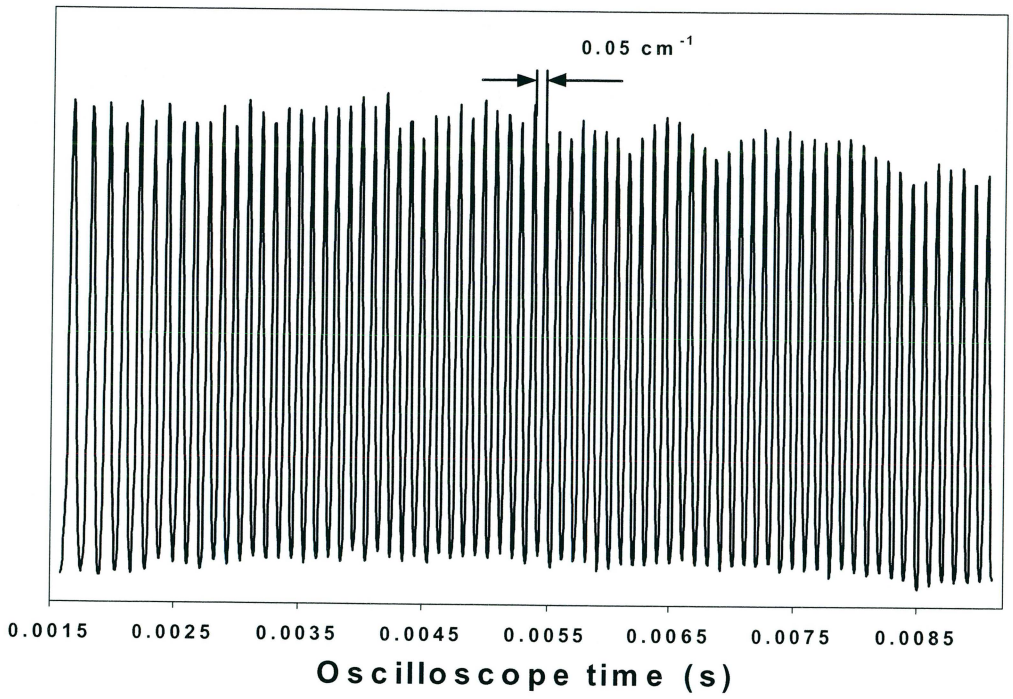

Figure 2. Ge etalon fringes around 3.4 μm corresponding to a continuos tuning range of 3.6 cm^{-1} (72 fringes).

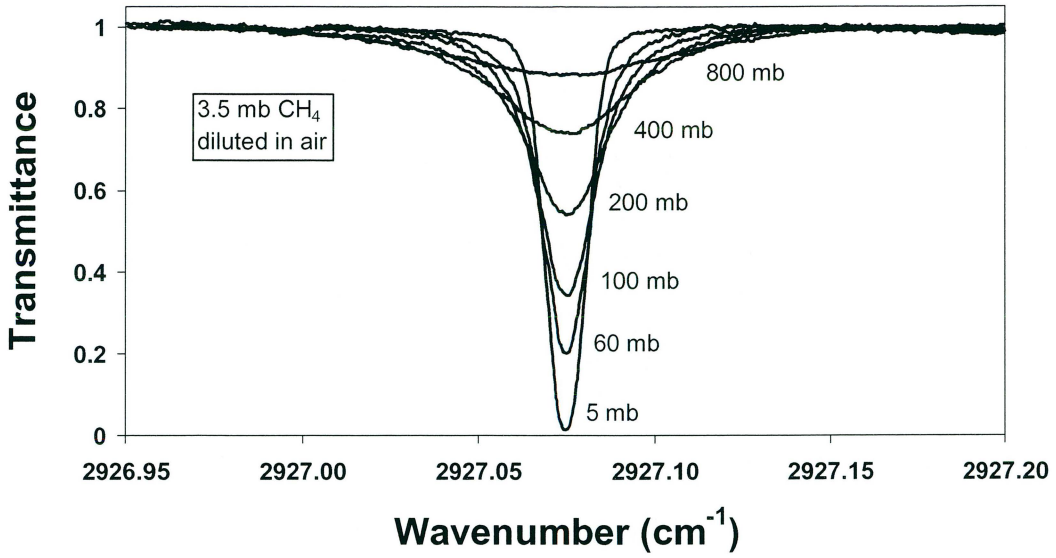

Figure 3. Methane spectrum as a function of pressure at 3.42 μm. The recordings are 500 scan averages, corresponding to a total sampling time of 4.5 sec for each curve.

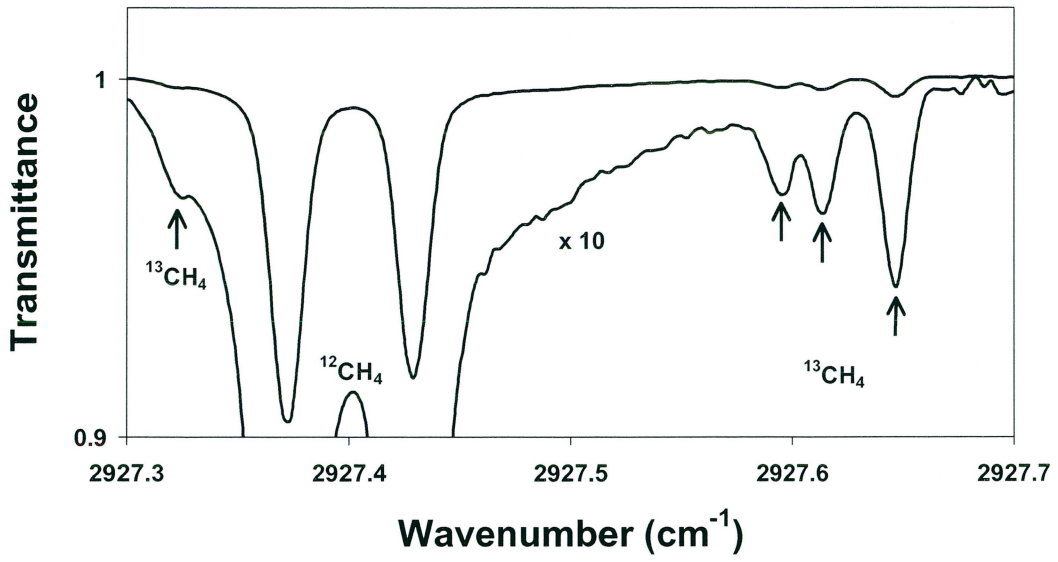

Figure 4. Low-pressure recording of methane gas exhibiting the low abundance species $^{13}CH_4$ in the presence of the normal $^{12}CH_4$ isotope.

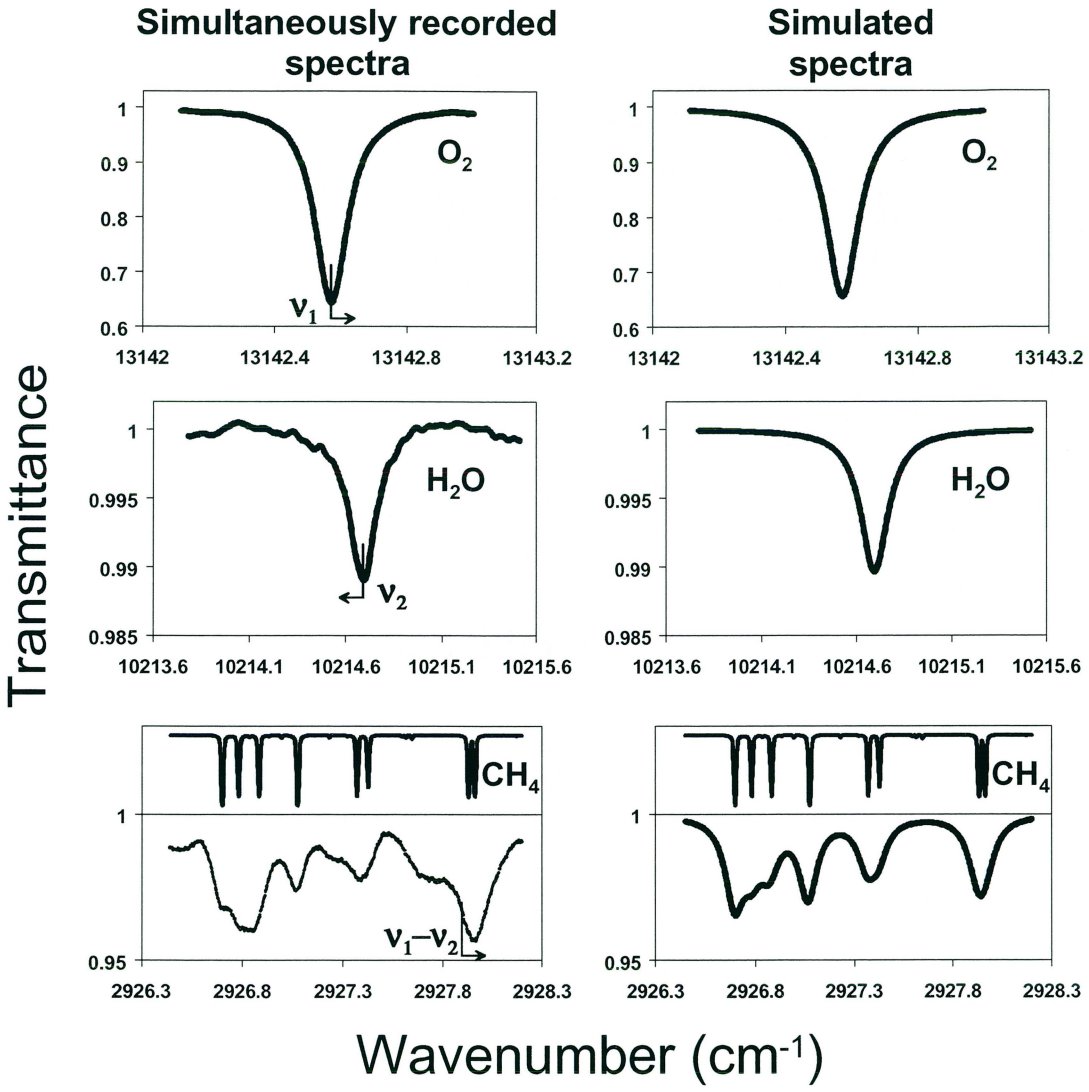

Figure 5. Simultaneous recordings of oxygen, water vapour and methane in a 15 m atmospheric path and corresponding spectral simulations based on HITRAN. Recording time is 4.5 sec. Scan directions in the individual laser sweeps and for the difference-frequency recording are indicated. Low-pressure, high-resolution spectra are included in the methane data.

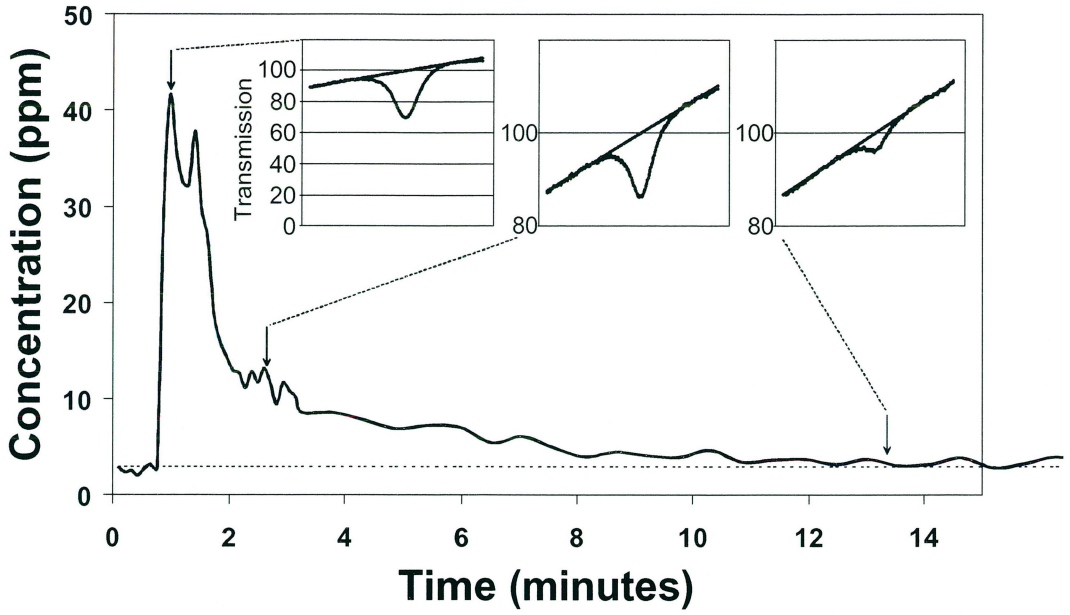

Figure 6. Monitoring of indoor methane concentration following the release of a small amount of gas from a tank. The measurement was performed over a 15 m pathlength. Raw data spectral recordings are shown as inserts in the figure.

VII

Compact fiber-optic fluorosensor using a continuos-wave violet diode laser and an integrated spectrometer

Ulf Gustafsson, Sara Pålsson, and Sune Svanberg
Department of Physics, Lund Institute of Technology
P.O. Box 118, S-221 00 Lund, Sweden

A compact fluorosensor with a fiber-optic measurement probe was developed, employing a continuos-wave violet diode laser as an exciting source and an integrated digital spectrometer for the monitoring of fluorescence signatures. Results from measurements on vegetation and human premalignant skin lesions are reported, illustrating the potential of the instrument.

I. INTRODUCTION

Laser-induced fluorescence is a powerful technique for non-intrusive, real-time diagnostics in a multitude of contexts. All solids and liquids, and complex compounds exhibit a broad-band fluorescence distribution devoid of sharp spectral features due to rotational quenching[1]. Fluorescence monitoring can be performed on samples *in situ*, e.g. in a laboratory or an operating room, through a microscope[2] or remotely using a fluorescence lidar system[3,4]. It can be applied in point monitoring[5] or in imaging applications[6,7]. Field of applications include diagnostics of human malignant tumors[8,9] and atherosclerotic disease[10], vegetation and water monitoring[11,12], analytical chemistry techniques such as HPLC and capillary electrophoresis[13], and forensic sciences[14].

Fluorescence diagnostics has been largely simplified through the availability of CCD detectors for direct read out of the spectrum obtained in the image plane of a spectrometer. With a short-pulse ultra-violet excitation laser, a gated and intensified CCD detector can be employed for efficient suppression of ambient light. Our group has developed several systems of this kind, which have been employed in medical and environmental monitoring. Original systems[15] were quite bulky, whereas later developments resulted in more portable equipment[16]. In the present paper we report on the construction and utilization of a very compact fiber-optic fluorosensor of the size 22 x 13 x 8 cm^3. This achievement became possible basically through two interesting recent developments. Firstly, violet and blue continuos-wave lasers have become commercially available at a power level of 5 mW[17]. Secondly, very compact integrated spectrometer units with CCD read out are now available providing unprecedented convenience for spectral assessment.

This paper is organized as follows: In Section II the construction of the fluorosensor is described. Section III gives examples from vegetation and human tumour diagnostics, and in a final discussion section suggestions for further developments are put forward.

II. FLUOROSENSOR SET-UP

The general lay-out of the new instrument is demonstrated in Fig. 1(a) and photographs of the system are presented in Figs 1(b) and 1(c). As a light source for inducing fluorescence we use a violet diode laser with a nominal operating wavelength of 396 nm (Nichia NLHV500). We note, that below 400 nm the eye safety regulations are relaxed by a factor of about 1000 since the cornea no longer transmits the radiation. Thus it is particularly convenient to be able to operate at these sufficiently short excitation wavelengths. The diode laser is driven by a power-supply (Wavelength Electronics LDD200-3M) with a 9 volt battery as input for decoupling from possible net transients, which can be detrimental to diode lasers. The diode laser is placed in a tube together with a collimating lens (Geltech C230TM-A). The output light is cleaned up for broadband spontaneous emission using a narrow-band interference filter (CVI F25-400-4-0.5).The violet radiation is focused by a fiber-port lens assembly (Optics for Research PAF-SMA-6-NUV-Z) into a 600 μm diameter optical fiber. Before entering the fiber the light beam is reflected off an appropriate dichroic beamsplitter (CVI). Fluorescence is induced in an object placed in contact with the distal tip of the fiber, where about 1.2 mW of laser power is available, and Stokes-shifted fluorescence light is conducted back through the fiber. Since the spectrometer is fiber-coupled, the fluorescence light is focused by a fiber port into a short fiber which is connected to the spectrometer. The spectrometer (Ocean Optics S2000) is equipped with a 100 μm slit. Elastically backscattered diode laser light is effectively blocked by a Schott GG420 colored glass cut-off filter placed behind the dichroic. The grating (600 lines/mm) disperses the light and a spectral region of about 330 - 1000 nm is captured on the 2048 element CCD detector. A spectral resolution of about 5 nm is obtained, which is fully adequate for environmental and medical monitoring.

The wavelength scale of the spectrometer is calibrated using a mercury/argon lamp (Ocean Optics HG-1). A spectrum from the calibration lamp is shown in Fig. 2(a) illustrating the resolution of the system. Since the exciting light is transmitted through the same fiber as the one used for the detection, fluorescence from the fiber itself constitutes a background, which can be stored for the case when the fiber is pointing in the free air and later be subtracted from actual recordings. The level of this fiber fluorescence is shown in Fig. 2(b). A spectrum for a solution of Rhodamine 6G (10 mg/60 ml ethylene glycol), observed through a 1 mm thick quartz window is shown in Fig. 2(c). In order to obtain a flat intensity response over the full spectrum a calibration is performed using a 200 W calibrated quartz tungsten/halogen lamp (Oriel 63355) with a know spectral distribution. The

reference spectrum is recorded through the optical fiber. By dividing the true spectral intensity by the recorded intensity a multiplicative correction curve is obtained which when multiplied by a recorded spectrum yields a standardized spectrum for the case of a "white" spectral response. The experimental spectral correction curve is given as Fig. 2(d). All spectra presented in the present paper were handled with the Microsoft Excel software after transfer from the spectrometer. All spectra shown below are standardized corrected spectral.

Since the laser source is not pulsed and the detection is not gated in contrast to the situation in more complex systems[15,16], there is clearly a risk that ambient light would add an undesired spectrum on top of the fluorescence spectrum. However, since the fiber is put in contact with the specimen under study, the ambient light is effectively shadowed away by the fiber itself in most cases. Under special circumstances (observing weak fluorescence) a reduction of the ambient light or a shadowing by the measuring site could be required. In indoor work with luminescent lamp illumination the presence of sharp mercury line peaks in a recorded spectrum would alert on problems due to ambient light.

III. MEASUREMENTS

We have used the new compact instrument in test measurements in two fields extensively studied at our department: vegetation monitoring and human malignant tumor diagnostics.

A. Plant fluorescence

Green vegetation exhibits characteristic fluorescence peaks in the near infrared spectral region. Chlorophyll *a* is effectively excited in the blue and red spectral regions yielding a dual-humped spectral distribution with peaks at about 685 and 740 nm[18]. The first peak is situated at a wavelength where the chlorophyll pigment still absorbs light. This means, that when the chlorophyll contents in a leaf increases the first peak cannot rise at the same rate as the second one. Thus, the intensity ratio I(740 nm)/I(685 nm) is related to the chlorophyll contents, and after calibration this ratio can be used for chlorophyll concentration assessment. Fluorescence recordings from a beech leaf exhibiting fully green as well as yellow and brown sections, due to senescence, are shown in Fig. 3. The recording time was 1 sec. Experimentally we find the intensity ratios 0.59, 0.28, and 0.17 for the green, yellow and brown regions of the leaf front side, respectively. The corresponding values for the back side are 0.54, 0.19, and 0.17, respectively.

B. Tumor fluorescence

Human tissue exhibits a bluish fluorescence when excited with a violet source. Among molecules contributing to the fluorescence, elastin, collagen, NADH and carotene can be mentioned[10]. Chemical compounds, called sentitizers, are selectively retained in malignant tumours following systemic, oral or topical

administration. Sensitizers, including porphyrins, phtalocyanines and chlorines, exhibit characteristic fluorescence signatures in the near infrared spectrum which can serve for clinical tumour diagnostics[8,15]. By irradiation of red light the same compounds can also mediate tumor cell necrosis through selective singlet oxygen release (photodynamic therapy[19]). A particularly interesting sensitizer is protoporphyrin IX, which is synthesized at a higher rate in malignant tumours after administration of δ-amino levulinic acid[20,21]. The synthesis of protoporphyrin IX can be readily seen through its characteristic fluorescence peaks at 635 and 690 nm, which can be used for tumour identification and demarcation[21].

Fluorescence diagnostics is routinely used as a diagnostic method in connection with photodynamic tumor therapy at the Lund Laser Centre, and the new equipment was used in connection with the treatment of a 74 year old male patient presenting with actinic keratosis, a premalignant skin disease. The tumors were prepared with a 20 % ALA cream which was left covered by occlusion pads during a 6 hour protophorpyrin IX build-up period. The pads and the cream were then removed. Fluorescence spectra were recorded in scans across the tumors before and after PDT. Recordings are shown in Figs. 4 and 5 with an accumulation time of 400 ms for each spectrum. In Fig. 4 the characteristic build-up of protoporphyrin IX in the tumor is clearly illustrated. The decrease of the blue fluorescence in the tumor is also a well-known phenomenon[7,8]. Fig. 5 illustrates the strong photobleaching of the protoporphyrin IX induced by the photodynamic treatment, a phenomenon that can be used for dosimetry.

IV. DISCUSSION

A compact fiber-optic fluorosensor was constructed and employed in vegetation and human skin monitoring. The system performance is similar to what is obtained from much larger and more complex fluorosensors. Back-ground light influence is the major draw-back in the present version of the system, favouring measurements in a somewhat shadowed region. However, by pulsing the diode laser with preserved average power the background can be effectively eliminated using repeated short accumulation periods. Presently, an ordinary personal computer was used for the data processing. Clearly, a lap-top computer, all-battery power and efficient soft-ware routines for on-line evaluation of diagnostic information will further enhance the attractiveness of fluorosensors of this kind.

ACKNOWLEDGMENTS

The authors gratefully acknowledge the collaboration with Dr. K. Svanberg in performing the clinical measurements. This work was supported by the Swedish Engineering Science Research Council and the Knut and Alice Wallenberg Foundation.

REFERENCES

[1]D. H. Hercules (ed.), *Fluorescence and Phosphorescence Analysis* (Interscience, New York 1966).

[2]B. Herman and J. J. Lemasters (eds), *Optical Microscopy* (Academic Press, San Diego 1993).

[3]P. S. Andersson, S. Montán, and S. Svanberg, Appl. Phys. **B44**, 19 (1987).

[4]S. Svanberg, Phys. Scripta **T58**, 79 (1995).

[5]S. Montán and S. Svanberg, Appl. Phys. **B38**, 241 (1985).

[6]P. S. Andersson, S. Montán, and S. Svanberg, IEEE J. Quant. Electr. **QE-23**, 1798 (1987).

[7]S. Andersson-Engels, J. Johansson, and S. Svanberg, Appl. Opt. **33**, 8022 (1994).

[8]S. Andersson-Engels, C. af Klinteberg, K. Svanberg, and S. Svanberg, Phys. Med. Biol. **42**, 815 (1997).

[9]K. Svanberg, I. Wang, S. Colleen, I. Idvall, C. Ingvar, R. Rydell, D. Jocham, H. Diddens, S. Bown, G. Gregory, S. Montán, S. Andersson-Engels, and S. Svanberg, Acta Radiologica **39**, 2 (1998).

[10]S. Andersson-Engels, A. Gustafson, J. Johansson, U. Stenram, K. Svanberg, and S. Svanberg, Lasers Life Sci. **5**, 1 (1992).

[11]L. Alberotanza, P. L. Cova, C. Ramasco, S. Vianello, M. Bazzani, G. Cecchi, L. Pantani, V. Raimondi, P. Ragnarsson, S. Svanberg, and E. Wallinder, EARSeL Adv. Rem. Sensing **3**, 102 (1995).

[12]H. Edner, J. Johansson, S. Svanberg, and E. Wallinder, Appl. Optics **33**, 2471 (1994).

[13]S. Nilsson, J. Johansson, M. Mecklenburg, S. Birnbaum, S. Svanberg, K.-G. Wahlund, K. Mosbach, A. Miyabayashi, and P.O. Larsson, J. Cap. Elec. **22**, 46 (1995).

[14]E. R. Menzel, Anal. Chem. **61**, 557A (1989).

[15]S. Andersson-Engels, Å. Elner, J. Johansson, S.-E. Karlsson, L. G. Salford, L.-G. Strömblad, K. Svanberg, and S. Svanberg, Lasers Med. Sci. **6**, 415 (1991).

[16]C. af Klinteberg, M. Andreasson, O. Sandström, S. Andersson-Engels, and S. Svanberg, Compact medical fluorosensor for minimally invasive tissue characterisation, to appear.

[17]S. Nakamura and G. Fasol, *The Blue Laser Diodes* (Springer Verlag, Heidelberg 1997)

[18]H. K. Lichtenthaler and U. Rinderle, CRC Crit. Rev. Anal. Chem. **19**, S29 (1988).

[19]S. L. Marcus, Proc. IEEE **80**, 869 (1992).

[20]J. C. Kennedy and R. H. Pottier, J. Photochem. Photobiol. B **14**, 275 (1992)

[21]K. Svanberg, T. Andersson, D. Killander, I. Wang, U. Stenram, S. Andersson-

Engels, R. Berg, J. Johansson, and S. Svanberg, British J. Dermatol. **130**, 743 (1994).

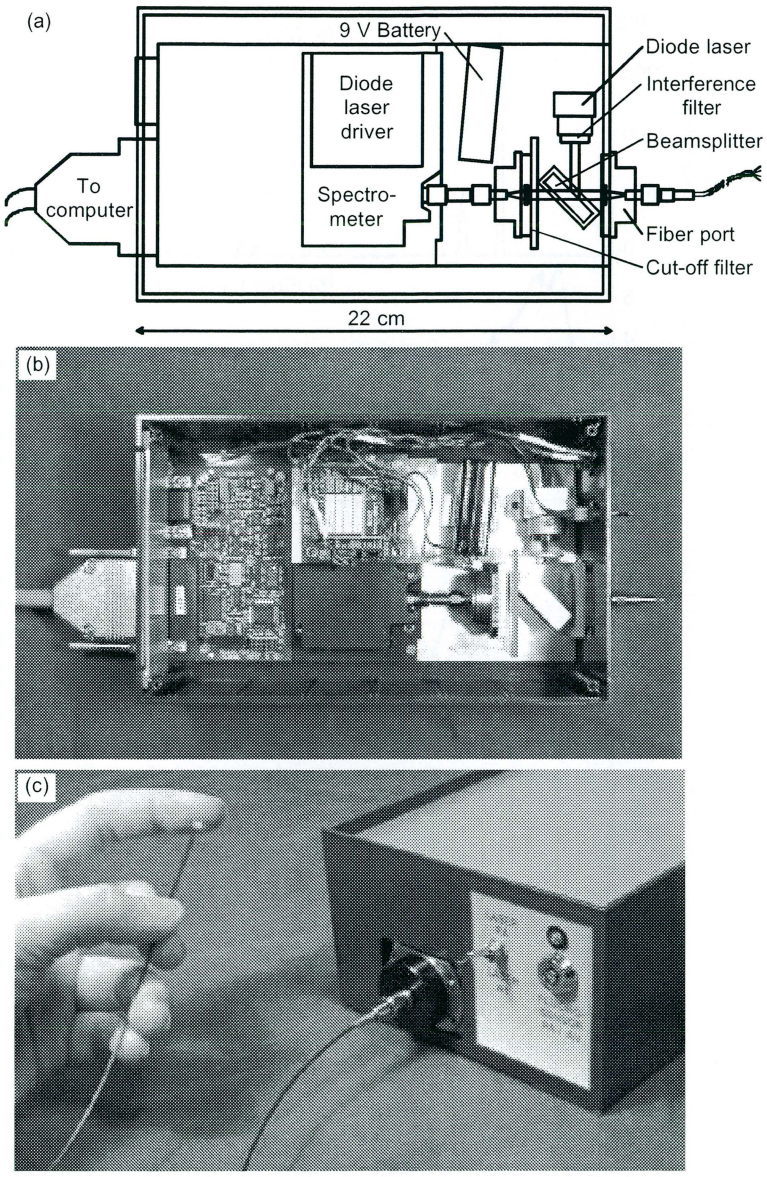

FIG. 1. (a) Schematic lay-out of the compact fluorosensor. (b) Photograph of the system interior. (c) Photograph of the system inducing skin fluorescence.

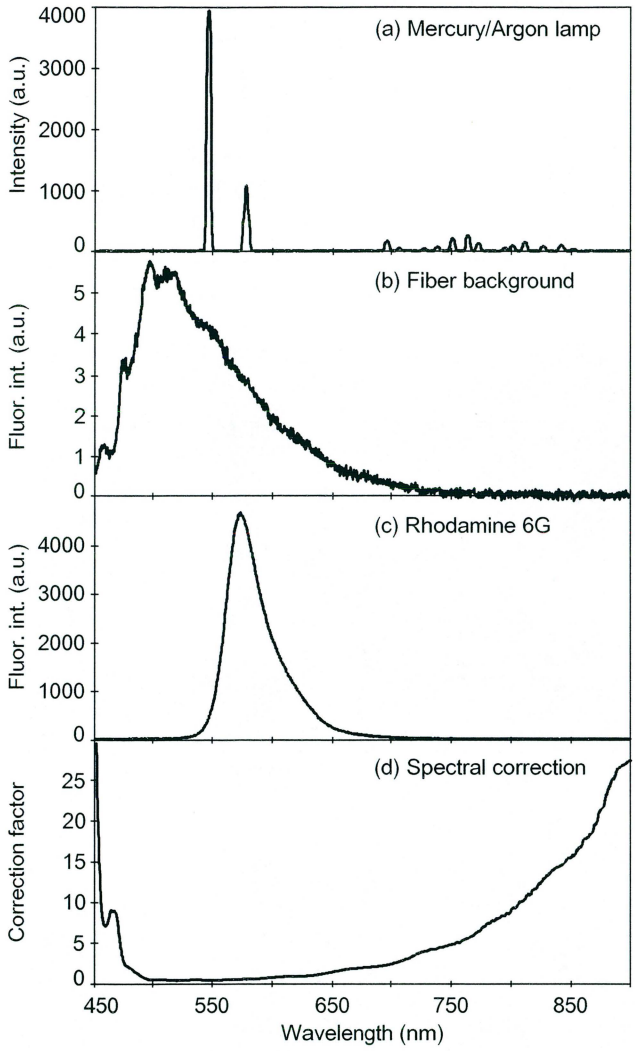

FIG. 2. (a) Recording of the emission spectrum of a mercury/argon lamp (integration time 10 ms). (b) Laser-induced intrinsic fiber fluorescence level to be subtracted from recorded spectra (intensity scaled for 10 ms integration time). (c) Fluorescence spectrum from a Rhodamine 6G solution (integration time 10 ms). (d) Spectral correction curve.

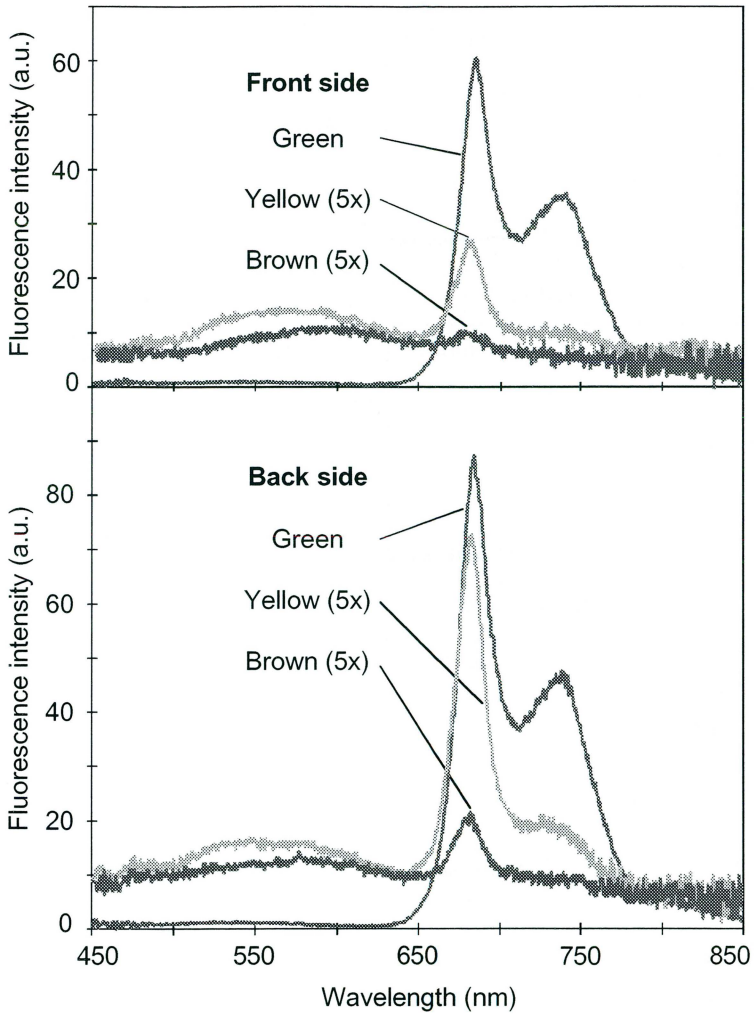

FIG. 3. Spectra from different parts of a beech leaf.

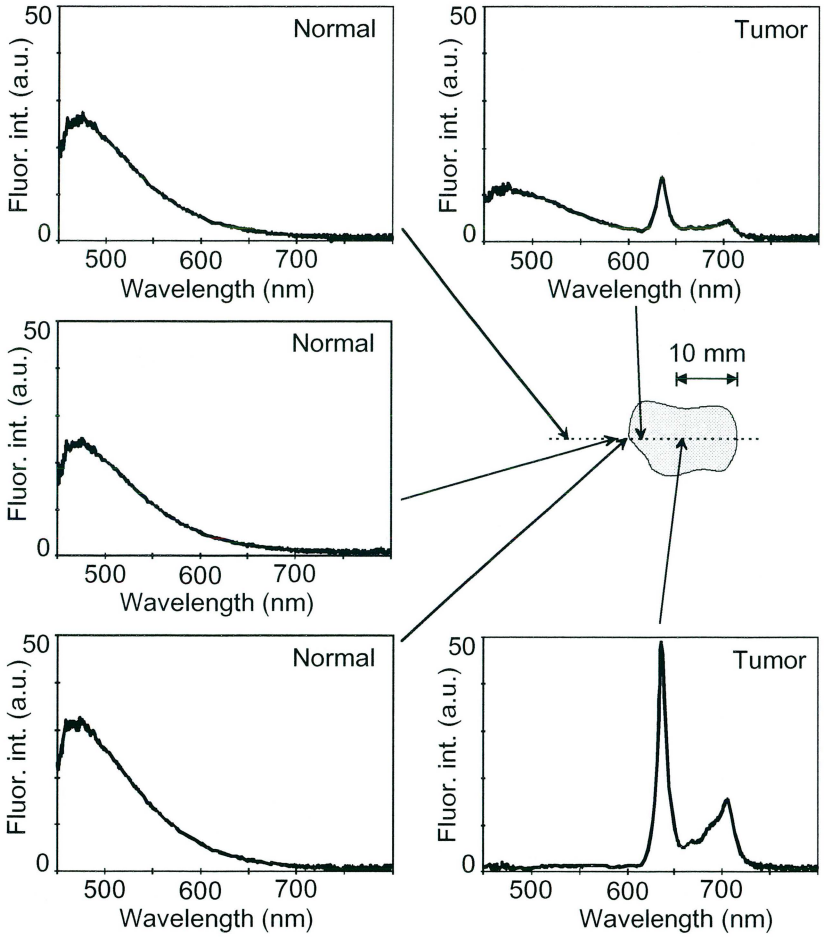

FIG. 4. Fluorescence spectra recorded in a scan across an actinic keratosis, sensitized by a cream containing δ-amino levulinic acid. Recordings before photodynamic therapy are shown.

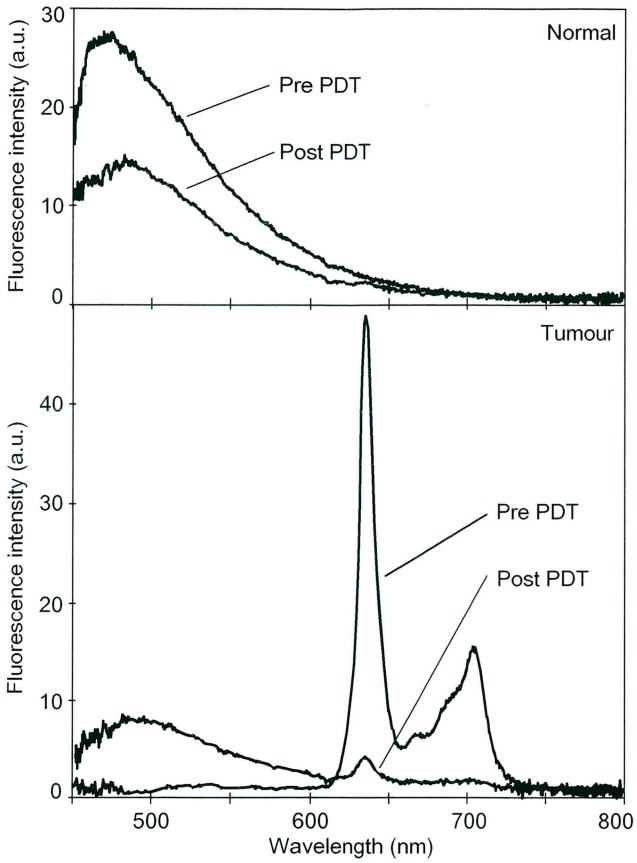

FIG. 5. Fluorescence recordings for actinic keratosis and normal surrounding skin before and after photodynamic therapy.

VIII

Coherent transient data rate conversion and data transformation

Xiangjun Wang, Mikael Afzelius, Nicklas Ohlsson, Ulf Gustafsson and Stefan Kröll
Dept. of Physics, Lund Institute of Technology (LTH)
Box 118, S-221 00 Lund, Sweden

Abstract

Temporal compression of optical pulses and pulse trains has been performed using the photon echo process in Tm doped YAG at 793 nm. Single pulse temporal compression by almost a factor of 500 from 10 μs to 22 ns and pulse train compression by almost a factor of 100 from 20 μs to 212 ns is demonstrated using a high-speed-frequency-tunable external cavity diode laser. It is expected that significantly higher compression could be obtained by improved control of the laser frequency and laser frequency chirps. Theoretically, Tm doped YAG would be capable of compressing single pulses by almost a factor 10^7.

At present there is a strong activity to investigate and develop the potential of photon echoes for all optical data storage and all-optical data processing applications. Potentially the photon echo approach can give exceptionally high storage densities [1]. Further, because it is the frequency Fourier transform of the temporal data that is stored in the photon echo technique it offers unique possibilities for all-optical processing of temporal data, see *e.g.* [2]. Such operations include *e.g.* all-optical address recognition of temporal sequences, pulse and data compression and stretching and all-optical logical operations.

All-optical operations on temporal signals can also be performed using combinations of gratings and prefabricated masks [3]. With respect to these techniques, time-domain operations using photon echo materials differ in the sense that they can be reprogrammed during the experiment instead of being limited to only one fixed type of operation. With photon echo techniques it is also possible to modify and tailor temporal signals in the microsecond to nanosecond region *i.e.* sub-MHz or kHz frequency resolution. Gratings and fabricated masks such as those in Ref. 3 are restricted to picosecond or sub-picosecond waveforms. Generally microsecond or nanosecond waveforms can readily be tailored using electronic equipment. However, photon echo materials and photon echo techniques do cover a time range from milliseconds down to femtoseconds and the microsecond to nanosecond domain is then a good range to initially investigate the limitations and possibilities for time-domain operations using photon echoes.

We propose that a potential application for the type of time-domain processing using photon echoes would be to work at the upper rate limit for electronic devices and then to

compress data in time and thereby increase the data rate using a photon echo process. The compressed data could propagate through a high speed transmission link and after this be stretched in time in a second photon echo process such that it again can be read by electronic devices. The energy efficiency in the photon echo process is in most cases (but not all [4]) low. Such a scheme would therefore probably also require amplification of the output from the initial photon echo data compression step [5], before the photon echo data stretching operation takes place.

Spurred by exciting prospects like those discussed above, we have, building on previous work by other groups [6,7,8], pushed to achieve improved performance in photon echo single pulse and multi-bit data compression. In the present paper single pulse compression by a factor of 450 from 10 μs to 22 ns and compression of a sequence of 10 bits by a factor of 92 is presented. It is interesting to note that when the chirp interval is much larger than the band-width of a single unchirped bit, the mathematical description of temporal multi-bit compression is equivalent to the mathematical description of transverse diffraction in space by a multiple slit pattern in the Fraunhofer approximation. Even if this particular effect not has been pointed out explicitly before, the issue of space-time duality in photon echo processes is well known, *e.g.* [9,10].

An external cavity diode laser equipped with an intra-cavity electro-optic (EO) crystal [11] was used in this experiment. The laser frequency of this external cavity diode laser could be linearly chirped over large intervals by supplying voltage ramps to the EO crystal. This construction is based on the design by Mossberg and co-workers [12]. The voltage ramps were generated by a Stanford Research, model DS345 30MHz synthesized function generator and amplified by a New Focus 3211 high voltage amplifier. The laser was operated in single-mode and tuned to the $^3H_4$ - $^3H_6$ transition line of the trivalent rare earth ion Tm^{3+} doped in YAG at 793.1 nm. A home built wavelength meter and a Coherent Model 240 Spectrum Analyzer monitored the wavelength and mode, respectively. The laser output power was about 30 mW with a short time line width of about 350 kHz over a time scale of 200 μs. This line width was measured by first irradiating the sample at fixed frequency and then observing the width of the hole burned in the absorption profile by applying a voltage ramp to one of the acousto-optic modulators and scanning the laser frequency across the hole. The pulses in the compression sequence are created by the acousto-optic modulators AOM1 and AOM2 (Isomet Corporation, model 1205C). The 0.1 at. % thulium-doped YAG crystal was 5 mm thick along the direction of light propagation and it was submerged in liquid helium. The laser spot (about 2 mm diameter) is focused onto the crystal by a 10-cm focal-length lens. The echo signal was detected with a Hamamatsu R943-02 photo-multiplier tube (PMT). An additional acousto-optic modulator (AOM3) was inserted at the detection side between the crystal and the PMT to reject the excitation pulses transmitted through the crystal.

The recorded data has been compared with analytical and numerical calculations of the photon echo time-compression process. A schematic picture of the input pulse

frequencies and intensities for the single bit and multi-bit compression experiments are shown in Figs 1a-d. The electro-magnetic field of the first pulse (or alternatively pulse sequence) and second pulse is denoted E_1 and E_2, respectively. The echo output field as a function of time, $E_e(t)$ equals the first input field $E_1(t)$ correlated with the second field $E_2(t)$ convoluted with itself (see *e.g.* [2]), *i.e.*

$$E_e(t) \propto \int_{-\infty}^{\infty} E_1^*(\omega) \cdot E_2^2(\omega) \cdot e^{i\omega t} d\omega , \qquad (1)$$

where $E_i(\omega)$ is the frequency Fourier transform of $E_i(t)$. We consider two chirped excitation pulses of length $T_1=T$ and $T_2=T/2$ respectively as in Fig. 1a. Assume that both excitation pulses are chirped over the bandwidth ω_{ch} and that $\omega_{ch} \cdot T >> 1$. Within the time interval $t \in [t_i - T_i/2,\ t_i + T_i/2]$ we write the electrical field of pulse i as $E_i(t) = e^{-i(\omega_0 + K\cdot(t-t_i))\cdot(t-t_i)} e^{-i\bar{k}_i \bullet \bar{r}}$, where $K = \omega_{ch}/(2T_i)$ The echo will now appear in the direction $\bar{k}_e = 2\bar{k}_2 - \bar{k}_1$ around time $t_e = 2t_2 - t_1$. Graf *et al.* [8] suggested that, in the regime $\omega_{ch} \cdot T >> 1$, the excitation pulses can be regarded as constant in the frequency interval $[\omega_0 - \omega_{ch}/2, \omega_0 + \omega_{ch}/2]$ and zero otherwise. Eq. (1) can then be simplified as

$$E_e(t) \propto \int_{\omega_0 - \omega_{ch}/2}^{\omega_0 + \omega_{ch}/2} e^{i\omega t} d\omega = e^{i\omega_0 t} \cdot \omega_{ch} \cdot \mathrm{sinc}\left(\frac{\omega_{ch}}{2} \cdot t\right), \qquad (2)$$

where we now have chosen zero for the time axis such that the echo occurs at time $t_e = 0$. The full width of half-maximum for the intensity of this echo pulse is approximately $T_e = 5.5/\omega_{ch}$. If the duration of the first pulse would be T_b, where $T_b \le T$ and the chirp rate is kept unchanged we can still use the result above if we replace ω_{ch} with ω_{ch}^b (where $\omega_{ch}^b = \omega_{ch}\ (T_b/T)$). Numerical and analytical calculations show that this result holds as long as $\omega_{ch} \cdot T_b >> 1$. The results above can now be used to analyze the compression of a sequence of data bits. We thereby consider the first pulse with time duration T, to consist of several bits of duration T_b that have their center points separated by a time T_s (Fig. 1c). If only $\omega_{ch} \cdot T_b >> 1$ the echoes of the separate bits all appear at the same time. To get the resulting echo field it is then sufficient to sum up the echo field from each individual bit. (If $\omega_{ch} \cdot T_b << 1$ and $\omega_{ch} \cdot T >> 1$ the first pulse will work as a brief pulse and the echo will have duration T.) Summing the echo output field for several individual bits j in Eq. (2) we obtain

$$E_{tot}(t) = \sum_j E_j(t) \propto \omega_{ch}^b \cdot \mathrm{sinc}\left(\frac{\omega_{ch}^b}{2} \cdot t\right) \sum_j e^{i\omega_0^j t} . \qquad (3)$$

In our case all bits have the same duration and $\omega_{ch}{}^{b}$ is independent of j. $\omega_0{}^{j}$ is the center frequency of bit j and can be expressed as: $\omega_0^j = \omega_0 + \frac{\omega_{ch}}{T} \cdot T_s \cdot (j-1)$, where ω_0 is the central frequency of the first bit ($\omega_0 = \omega_0{}^{1}$). Eq. (3) becomes particularly simple if the data stream contains the maximum number of bits, *i.e.* j runs from *1* to N_b, where N_b is the number of bits in the sequence. The resulting intensity then becomes

$$I(t) \propto \omega_{ch}^{b\,2} \cdot \mathrm{sinc}^2\left(\frac{\omega_{ch}^b}{2} \cdot t\right) \cdot \frac{\sin^2\left(N_b \cdot \frac{\omega_{ch}^b}{2T_b} \cdot T_s \cdot t\right)}{\sin^2\left(\frac{\omega_{ch}^b}{2T_b} \cdot T_s \cdot t\right)}. \qquad (4)$$

Eq. (4) (and in fact essentially the whole treatment starting from Eq. (2)) is analogous to a much more often discussed experimental case, namely the far field intensity pattern due to Fraunhofer diffraction by a multi-slit pattern. Exactly the same equations would result for N_b slits, each with a width $\omega_{ch}{}^{b}$ and a slit separation $(\omega_{ch}{}^{b}\ T_s)/T_b$. Time is then replaced by the wave vector perpendicular to the slits, $t \rightarrow k\sin\theta$, where k is the wave vector and θ is the diffraction angle.

Figure 2a shows a 10 μs long pulse chirped over 230 MHz compressed to 22 ns and the inset shows the echo output on an expanded time scale. The noise in the input pulses arise from PMT shot noise because AOM3 does not open until after the second input pulse. Optimum compression with a 230 MHz chirp would give an echo duration of about 3.8 ns. The current echo signal is a factor of 6 longer. In our experiments the echo duration for large compression factors often had a longer duration than predicted by theory. We believe this occurred because the chirp rates for the first and second pulses deviated slightly from the optimum 1:2 ratio. This may for example be due to noise and non-linearity in the voltage ramps sent to the high voltage amplifier and EOM crystal from the arbitrary function generator. The influence of the 350 kHz laser line width was modeled using a random walk phase diffusion process. This could, however, not explain the increased echo duration at higher chirp rates.

Figure 2b shows a 10-bit sequence transformed in time from 20 μs to 212 ns. The signal-to-noise in this trace is not sufficient to show the side-band structure due to the presence of multiple bits in the input sequence. Although the duration of the compressed signal is two orders of magnitude shorter than the input sequence the fidelity is not sufficient for extracting the input by Fourier transforming the output data. Such a side-band structure, which is where the information about the bit sequence actually is contained, is on the other hand shown in the solid curve in Fig. 2c. This is the echo output from a 3 bit input sequence similar to the 4 bit sequence displayed in Figs 2c and 2d. Each bit has a duration $T_b = 1\mu s$ and these bits are separated by $T_s = 2\mu s$. The data is thereby compressed a factor of 20 from 7μs to 350 ns. The chirp, ω_{ch}, roughly covers

60 MHz during 20 μs. The dashed curve in Fig. 2c is the theoretically calculated photon echo output using Eq. (4) for the input signal in Fig. 2c. As discussed by Graf *et al.* [8] the shortest duration for a compressed pulse train at a given chirp rate is the same as the duration of a compressed single bit at this given chirp rate.

Although the data in Figs 2a and 2b demonstrate an order of magnitude improvement in single-bit and multi-bit pulse compression compared to previous investigations [6, 7] a still more interesting experimental domain would be to compress ns duration pulses to ps duration to reach into the domain which cannot be handled by conventional electro-optic equipment. The present investigation did not include any detailed investigation of the signal levels but the excitation power has been about 3-5 mW and the overall pulse duration typically has been about 10 μs, *i.e.* we have used an excitation energy of about 30-50 nJ. The number of echo output photons will be proportional to the product $sin^2\theta_1$ $sin^4\theta_2$ (see *e.g.* Ref. 13). Where θ_i, the pulse area for pulse i, is given by $\theta_i = 2\mu E_i T/\hbar$, where μ is the transition dipole moment. For small pulse areas the number of output photons will essentially be proportional to the quantity [(Electro-magnetic field) × (pulse duration) × (transition dipole moment)]^6, which also is proportional to [(Pulse energy) × (pulse duration) × (transition oscillator strength)]^3. For a given input pulse *energy* the number of output photons will consequently be the same for μs and ns input pulses if the oscillator strength, f, is increased by three orders of magnitude in the latter case. This would correspond to an oscillator strength increase from 10^{-7}-10^{-6} to 10^{-4}-10^{-3}, which is by no means unrealistic. For ns excitation on highly allowed transitions, $f \approx$ 0.1-1, the input *power* could be kept in the few mW region and the number of output photons would still be the same as for our microsecond excitation pulses in Tm doped YAG.

In summary we have demonstrated photon-echo-based single bit temporal compression by a factor of 450 and multi-bit compression by a factor of 20. The single-bit compression represent an order of magnitude and the multi-bit compression a factor of two improvement compared to what has been obtained previously in photon-echo pulse compression. Our current values are limited by the stability of the diode laser and diode laser control system used in these measurements and by the laser power. There is no reason not to believe that significantly better compression could be obtained by using higher power and a more stable system. Such a system is presently developed. We argue that suitable photon echo materials can be used to compress GHz data to THz rate and to decompress THz data to GHz rates which, *e.g.*, could be an approach to time multiplexing in optical communication.

This work was supported by the Swedish Research Council for Engineering Sciences (TFR) and the Swedish Natural Science Research Council (NFR).

Figure captions

Fig. 1
Input intensity (a) and frequency (b) as a function of time for single pulse compression. The excitation pulses are centered around times t_1 and t_2. ω_0 is the center frequency of the frequency chirp. The echo occurs at the time indicated by the vertical line. Traces (c) and (d) show the same input parameters for multi-bit compression. ω_0^j is the center frequency for input bit j.

Fig. 2
(a) Single pulse compression of a 10 μs input pulse by a factor of 450 to a full width of half maximum of 22 ns. The inset shows the echo output on an expanded time scale.
(b) A 20 μs long 10-bit pulse train is transformed in time to approximately 200 ns duration. For the compressed signals the bit information is contained in the side-band structure. Such a side band structure is shown in trace (c).
(c) Solid line: Compressed echo output for a three bit input sequence (details given in text). Dashed line: Theoretical simulation based on Eq. (4). Experimental and simulated peak intensities are normalized to unity. ω_{ch}^b has been used as fitting parameter.

References

1 W. R. Babbitt and T. W. Mossberg, J. Opt. Soc. Am. B**11**, 1948 (1994).

2 M. Mitsunaga, Opt. & Quant. Electron. **24**, 1137 (1992).

3 A. M. Weiner, S. Oudin, D. E. Leaird and D. H. Reitze, J. Opt. Soc. Am. A**10**, 1112 (1993).

4 M. Azadeh, C. S. Cornish, W. R. Babbitt and L. Tsang, Phys. Rev. A**57**, 4662 (1998).

5 R. Krishna Mohan, U. Elman, M Tian and S. Kröll, Opt. Lett. **24**, 37 (1999).

6 Y. S. Bai and T. W. Mossberg, Opt. Lett. **11**, 30 (1986).

7 T. Wang, H. Lin and T. W. Mossberg, Opt. Lett. **20**, 2033 (1995).

8 F. R. Graf, B. H. Plagemann, E. S. Maniloff, S. B. Altner, A. Renn and U.P. Wild, Opt. Lett. **21**, 284 (1996).

9 B. H. Kolner, IEEE J. Quantum Electron. **30**, 1951 (1994).

10 L. Ménager, I. Lorgeré, J.-L. Le Gouët, R. Krishna Mohan and S. Kröll, Opt. Lett. **24**, 927 (1999).

11 R. Nilsson, Lund Reports on Atomic Physics, **LRAP-241**, LTH, Lund (1998).

12 C. Greiner, B. Boggs, T. Wang and T. W. Mossberg, Opt. Lett. **23**, 1280 (1998).

13 S Kröll and P Tidlund, Appl. Opt. **32**, 7233 (1993).

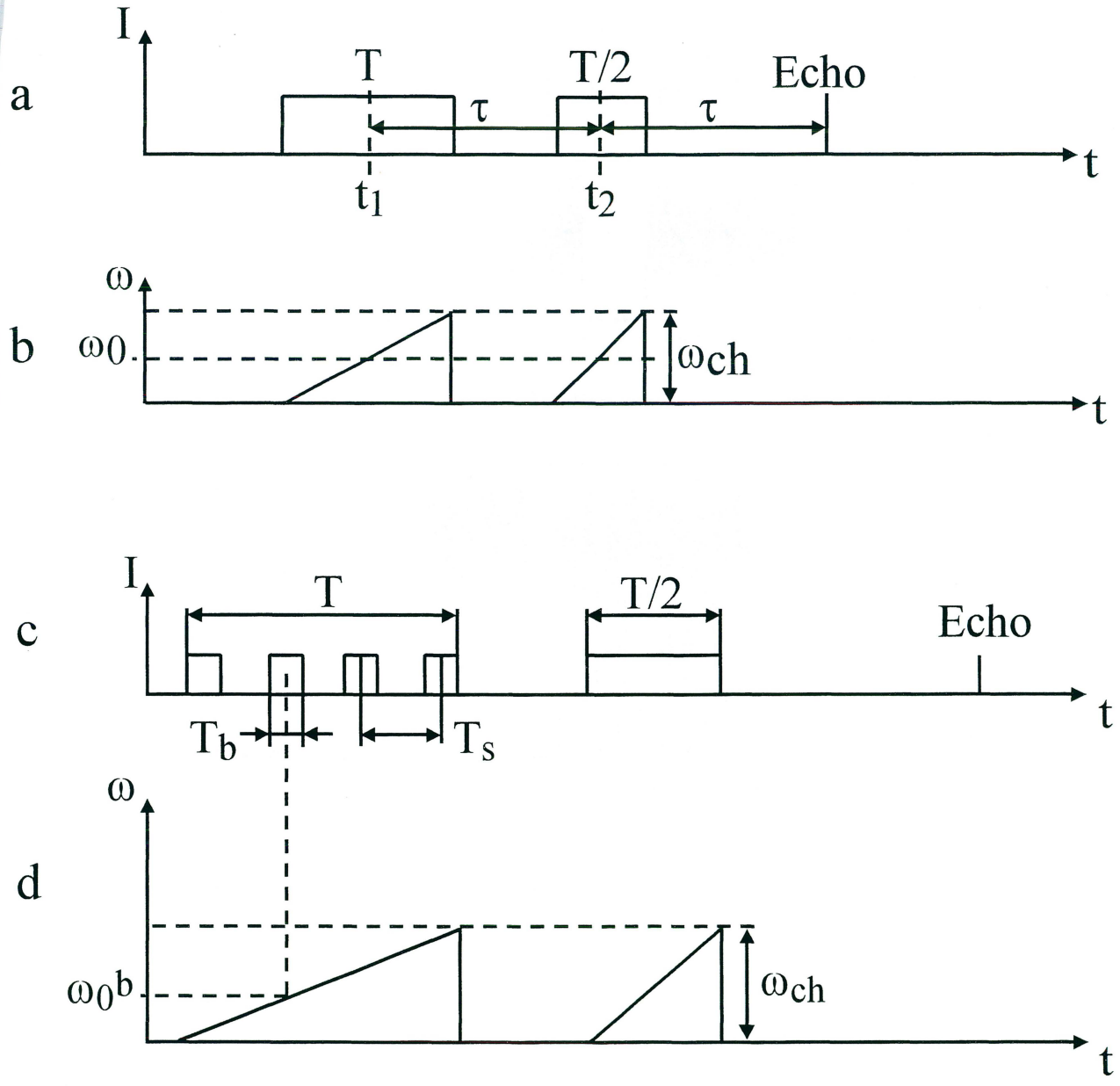

Figure 1

a

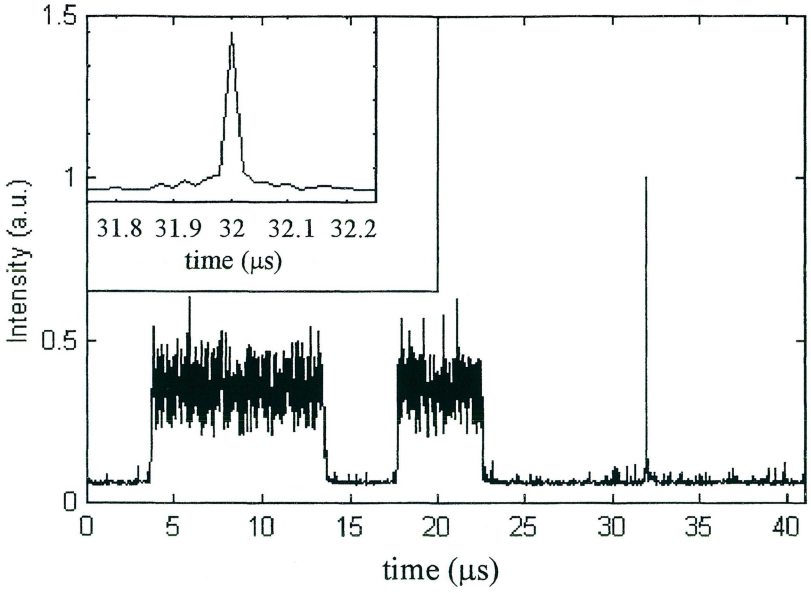
1.5
1
0.5
0
Intensity (a.u.)
31.8 31.9 32 32.1 32.2
time (μs)
0 5 10 15 20 25 30 35 40
time (μs)

b

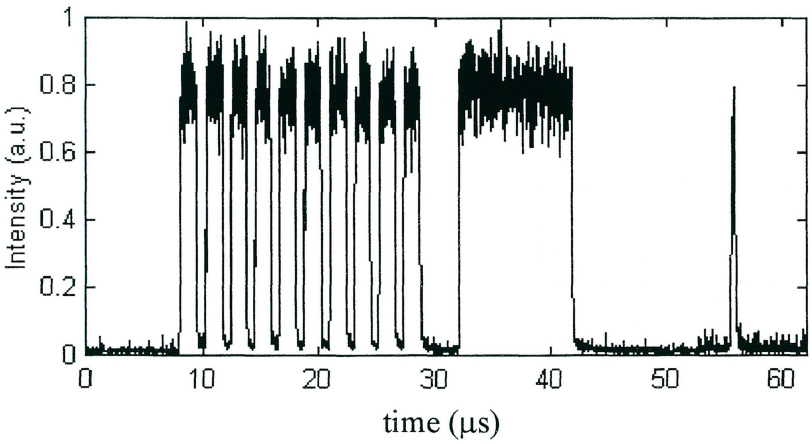
1
0.8
0.6
0.4
0.2
0
Intensity (a.u.)
0 10 20 30 40 50 60
time (μs)

c

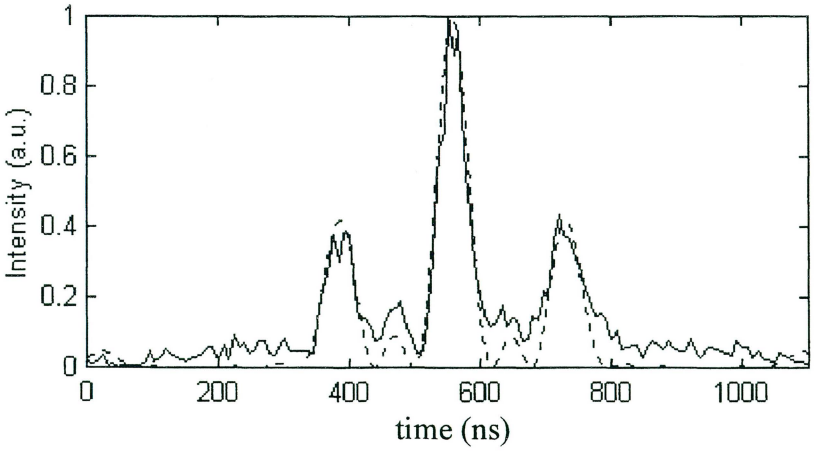
1
0.8
0.6
0.4
0.2
0
Intensity (a.u.)
0 200 400 600 800 1000
time (ns)

Figure 2